Computational Methods for Understanding Dynamics in Mass Transport and Tissue Development

by

Kejie Chen

A dissertation submitted in partial fulfillment
of the requirements for the degree of
Doctor of Philosophy
(Mechanical Engineering)
in The University of Michigan
2020

Doctoral Committee:

Professor Jianping Fu, Chair
Professor Charles Doering
Professor Bogdan Epureanu
Professor Donald Siegel

Kejie Chen

chenkjie@umich.edu

ORCID ID: 0000-0001-6591-5875

ACKNOWLEDGEMENTS

PhD is a joyful and memorable journey for me. I learned lots of professional and life knowledge during this period. This dissertation marks an important milestone in my career. Here, I wish to thank all who helped me make this work possible.

I wish to sincerely thank my advisors Professor Jianping Fu and Professor Bogdan Epureanu for their guidance and support throughout my PhD studies. Their wisdom and knowledge have significantly influenced my research philosophy and style, and helped me become better in research and life. Prof. Epureanu has helped me develop passion in research and become confident. He helped me realize the importance and taught me skills about how to clearly explain concepts and works to people. Prof. Fu guided me into a cutting-edge field and pointed out important and interesting research questions. In their labs, I am lucky to get research experience in both theoretical and experimental fields. I also want to thank my committee member Professor Charles Doering. I always learned something when I had a short or long conversation with Prof. Doering. He can always precisely pointed out my problems or concerns and gave me timely suggestions. I also want to thank my committee member Professor Donald Siegel. Prof. Siegel has helped me overcome many challenges and difficulties during my PhD and gave me helpful advices and support. Without their guidance and help, I would not be able to complete this PhD journey.

I want to express my appreciation to my family, for their unconditional love and support. Their accompany gave me courage and strength to face challenges and keep moving forward. I made lots of friends at University of Michigan. They brought me

immense joy and made my life more colorful and meaningful. I am really grateful to have all my amazing friends.

TABLE OF CONTENTS

CHAPTER

LIST OF FIGURES

Figure

LIST OF TABLES

Table

ABSTRACT

Elucidating the process by which a biological system evolves and properly identifying hidden states and influential underlying factors are important for studying biological functions and origins of diseases. However, due to the small length and time scale of many biological systems, these evolution processes are “invisible” under current microscopy techniques. The goal of this dissertation is to provide mathematical and computational models to help re-construct the dynamics inside biological systems from limited experimental observations and aid the understanding of system properties. Three different types of models were developed using first principles, mathematical abstraction and data-based statistical inference.

To describe the dynamical transport of intracellular cargoes and reveal underlying factors that impair transport efficiency, a multi-physics stochastic model is developed based on first principles and solved by Monte Carlo simulation. In the model, the transport of a cargo by multiple kinesin motors along tracks (microtubules) is simplified as a spherical cargo being moved forward by several non-linear springs along cylindrical and intersecting tracks. The thermal diffusion of cargo, walking motion of motors, and interactions between cargo, motors and tracks are considered based on fundamental physics laws. Using the model, comprehensive collective behaviors of motor kinesins influenced by the topology of tracks were uncovered and studied based on macroscopic experimental observations such as the transport directions and pausing time at track intersections.

To connect the macroscopic particle distribution with its microscopic properties, such as particle moving direction and speed, a generalized random walk model is introduced. Particularly, the influence of directional heterogeneity (i.e. probability of moving along θ direction is non-uniformly distributed between 0 and 2π) on particle diffusion coefficient and mean square displacement is studied. We observed that when directional heterogeneity only depends on space, particle performs normal diffusion with directed drifting. Including the correlation between directional persistence (i.e. probability of maintaining current moving direction) and particle speed leads to Fickian but non-Gaussian particle diffusion. Furthermore, the self-reinforced directional persistence leads to superdiffusive motion of particles. The generalized random walk model can be used as a mathematical abstraction of the movements of many biological particles, such as cell migration and intracellular protein diffusion. Given the macroscopic distribution of biological particles, the proposed model provides insights about their moving speed and directional persistence.

In the end, an image-based tissue profiling and trajectory inference algorithm is developed. This algorithm extracts morphological and intensity features from tissue images fixed at discrete time points. By projecting high-dimensional feature data set to new coordinates based on tissue similarities, the algorithm helps reduce systematic noise coming from the tissue heterogeneity and inference a continuous developmental trajectory. Following the trajectory, the bifurcating expressions of proteins were predicted and applied to understand tissue development dynamics. In particular, the developmental progression of embryonic-like tissues, including the morphological changes and appearance of new cell types, are studied based on the algorithm.

CHAPTER I

Introduction

1.1 Overview

One important goal in biomedical science is to achieve predictable understanding of functions and mechanisms involved in living cells, tissues and even whole organisms. To date, much effort has been directed toward understanding static "snapshots" of biological systems from microscopy. For example, fluorescent images of cells and tissues are widely used to characterize cell types and their spatial organizations [9]. The conformation of nano-size molecules and proteins is visualized based on X-ray crystallography [10]. In reality, however, living systems dynamically alternate between transient sub-states. Many biological functions and biochemical mechanisms largely depend on the temporal regulation and spatial compartmentalization of the dynamical system. For example, static microtubules (MTs) are aligned along the neuronal axon to support transport of proteins, while dynamic MTs, which undergo continuous polymerization and depolymerization, accumulate at neuronal growth cone to produce forces for axonal elongation [11, 12]. Therefore, besides the information acquired from discrete image snapshots, mathematical and computational tools are developed to elucidate the continuous evolution of the structure and morphology and predict long-time associated functions and rare events. In this dissertation, three types of mathematical and computational tools are developed to understand the multi-scale dynamical biological systems. Specifically, a multi-physics computational algorithm is built based on first principles to understand the intracellular transport dynamics mediated by kinesins. A coarse-grained probabilistic model is proposed for particle diffusion and transport. It can be applied to investigate cell migration dynamics. Furthermore, a statistical data-driven method is applied to inference the morphological and proteinomic bifurcating development of embryonic-like tissues. In the following sections in this chapter, I am going to introduce the background biology knowledge related to intracellular transport, cell migration and development of embryonic-like tissues. At the end of this chapter, the major contribution of this dissertation is summarized.

1.2 Intracellular transport (axonal transport)

Adult-onset neurodegenerative diseases (AOND) contains a group of neurological disorders, such as Alzheimer's disease (AD), amyotrophic lateral sclerosis (ALS) and Huntington's disease (HD). In the past decades, studies based on post-mortem brains, animal models and in vitro cultured neuron cells have revealed that a certain population of neurons, which usually extend axons to distant targets, undergo a gradual loss of functions and connectivity at the early stage of AOND diseases [13, 14, 15]. The AOND pathology begins many years before the emergence of cognitive impairment symptoms. Understanding the pathogenic mechanisms of AOND diseases through molecular and genetic aspects can help develop biomarkers for early diagnosis as well as providing insights to therapeutic interventions.

The causes of neuronal dysfunction and disconnection at the early stage of AOND appear multifactorial. The defective axonal transport, which leads to the accumulation of phosphorylated neuronal proteins in the proximal axons, is a primary hallmark during the disease progression [13, 16, 17, 18]. The axonal transport refers to a group of intracellular trafficking events that happen inside neuronal axon to deliver synthesized organelles and proteins, remove degraded and misfolded materials and help maintain structural and functional heterogeneity and integrity among axonal and dendritic subdomains. The axonal transport is achieved by groups of molecular motor proteins, including kinesin, dynein and myosin, moving along the microtubules (MTs) (Figure 1.1 a). Specifically, MTs are long, hollow cylindrical shape and made up of many α- and β-tubulin heterodimers. α, β-tubulin dimers undergo continuous polymerization and depolymerization at the two ends of the MT. One MT end has α-tubulin exposed. This end points toward cell body and grows slow, which is defined as the minus end. Another end has β-tubulin exposed and points toward the axon tips and grows fast, which is the plus end (Figure 1.1 b). Motor proteins on the MT, including kinesin, dynein and myosin, convert chemical energy from Adenosine triphosphate (ATP) to mechanical motions of intracellular cargoes. Kinesin-1 (conventional kinesin) walks toward the plus end of the MT (anterograde transport) in a step-wise fashion. In this dissertation, kinesin-1 is referred to as kinesin. Kinesin has two heavy chains and two light chains. Each heavy chain contains a globular head domain, a neck linker, a α-helical stalk and a tail. The head domain interacts with MT and ATP. The tail domain connects to the kinesin light chain and modulate the binding to the cargoes, as shown in Figure 1.1 c [19]. Dynein moves in the opposite direction along the MT (retrograde transport). Dynein has two heavy chains interact with the MT and a doughnut-shape head responsible for the force-generating ATPase activity [20]. Myosin walks along the actin filaments enriched in nerve terminals and is involved in retrograde transport and cellular force generation [21].

Most current studies about deficit axonal transport focus on investigating how the binding affinity between motor proteins, cargoes and MTs influence axonal transport efficiency (quantified by transport speed and protein distributions) and what signaling pathways are involved. The binding affinity between kinesin and its cargo is found to be modulated by the phosphorylation of kinesin light chains and mutation of

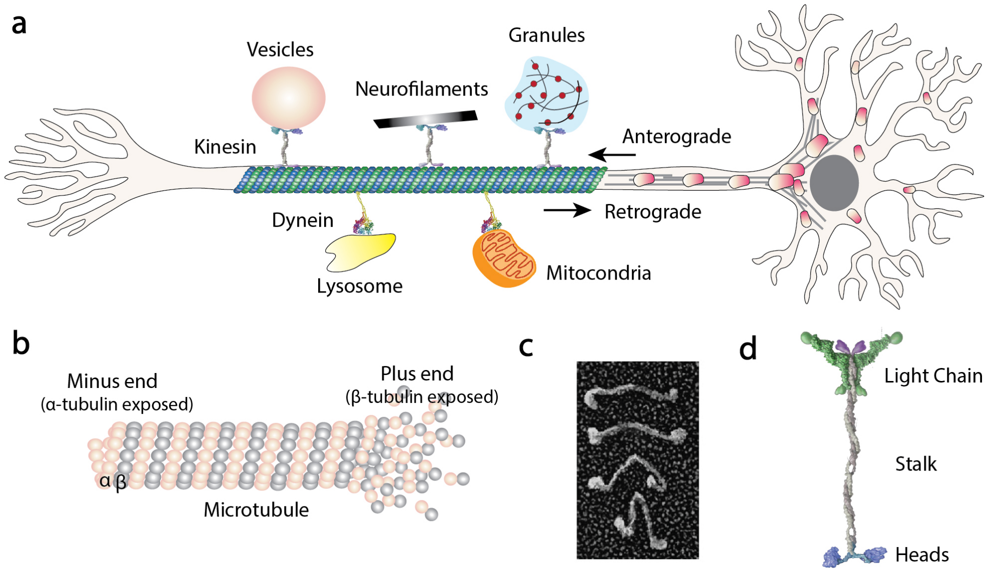

Figure 1.1: **Axonal transport.** **a**, Intracellular organelles and proteins are transported by molecular motor protein kinesin and dynein along the MT. **b**, MT is comprised by many α, β-tubulin dimers. **c**, Electron microscope image of the kinesin [1]. **d**, Schematic illustration of the structure of the kinesin [2]. Kinesin contains two heads, a long stalk and two tails.

proteins which interact with kinesin light chains, such as c-Jun-N-terminal kinase related proteins [22]. For example, in the model of AD, the depletion of kinesin light chains increases the retrograde transport of amyloid precursor protein (APP), enhances the production of toxic amyloid-β peptide and causes the axonal swelling [23]. The binding affinity between kinesin and MT is found to be influenced by MT-associated proteins and tubulin acetylation [16, 24]. For example, MT-associated protein tau promotes the detachment of kinesin from MT. Under a high concentration of tau proteins, the axonal transport is likely to be dominated by dyneins toward the minus end of the MT, while a low concentration of tau facilitates the anterograde transport by kinesins [25].

However, the axonal transport of cargoes is a complicated dynamical process that involves not only the binding between cargo, MT and kinesin, but also generation of mechanical forces and continuous motion of cargo-kinesin complex [26]. Until now, most live cell imaging tools only allow capturing the static distribution of many fluorescent cargoes and the topology of MT networks where each MT is visualized as a two dimensional line [27]. Based on the image information and pharmacological perturbations, for example, Ali et al. found that compared with parallel MT bundles, networks containing lots of intersecting MTs inhibit the growth of axonal tip. But why and how transport gets impeded by disorganized structures is not understood because of the difficulty of visualizing the movements of cargoes and motor proteins. Uncovering high-resolution and dynamical structures of MTs and motor proteins, such as the growth and shrinkage of MTs and walking of motor proteins, requires advanced fluorescent labeling and imaging techniques. For example, Shaul et al. analyzed the dynamical MT organization inside the motor neuron of C. elegans using a self-developed light microscopy, and found that MT length and coverage area limits transport efficiency by influencing the run length and pausing frequency of cargoes [28]. Using total internal reflection fluorescence microscopy (TIRF), Brigette et al. visualized the distribution of tau and MAP7 proteins along a MT inside neuronal axon. They found that MT associated protein MAP7 can displace tau from MT lattices and recruit kinesins to the MT [29].

Due to limited sources of advanced microscopy and extensive analysis required to process specimens at various time points, little knowledge about the dynamical transport process has been provided. Alternative methods, including computational models and statistical inference algorithms, could be applied to assist the understanding of axonal transport. Specifically, at a length scale of sub-nanometer and nanometer, the molecular dynamics based methods are used to study the evolution of structure and inner stress of a motor protein when it walks along a MT during a time interval of several hundred nanoseconds. For example, Wang et al. studied the molecular origin of susceptibility to external force for a kinesin and found that the key effect of external force on kinesin velocity is through controlling ATP releasing rate from the MT [30]. At a length scale of sub-micrometer, the comprehensive structure of a motor protein is simplified as a non-linear spring that can apply mechanical force to the cargo when its heads move forward and the motor gets stretched. For example, Bergman et al. simplified the transport system as multiple springs randomly distributed on a spherical cargo. Motors attaching to and detaching from MTs are regulated by constant rates. When motors attach to a track, it moves forward and pull the cargo. Based on the model, they predicted probabilities of choosing different transport directions or being trapped at MT intersections. The model predictions are further verified based on in vitro cargo transport experiments [31]. At a large length scale of several micrometers and millimeters, distinct axonal transport modes, including fast and slow transport, anterograde and retrograde transport and diffusion, are described based on multi-state transition models [32]. In practice, the hidden Markov algorithm is applied to extract diffusive and transport states of axonal proteins based on experimentally measured protein trajectories [33, 34].

1.3 Cell migration

Cell migration plays a critical role in the development of tissues and organs. The migration of ill-regulated cell motility is often related to the onset of diseases, such as tumor metastasis, wound healing and immunological responses [35, 36, 37, 38, 39]. For example, resistance to parasites, such as *T. gondii* in the central nerve system, relies on T cells migrating within lymphoid tissues and targeting pathogens in sites of inflammation [35]. Generally, studies about cell migration focus on two aspects, single cell migration statistics and collective cell behaviors.

To understand the self-generated movements of single cells, in the experiments, cells are cultured on 2D substrate or embedded in 3D gel matrix, and time series of cell positions are acquired [40, 41]. Several studies further adjust the stiffness and chemical gradient of extracellular environment to study durotaxis and chemotaxis properties [41, 39]. It has also become feasible to track fluorescent protein expressing cells in animal models by multi-photon imaging and measure their migration trajectory [35, 36]. Based on the trajectory, the mean square displacement (MSD) as well as the probability distribution of displacements are calculated over time and used as identifiers of migration statistics. It has been found that for some types of cells, the MSD of cell displacement is superlinear with time and the displacement distribution is non-Gaussian [42, 35, 43, 38]. The anomalous migration statistics usually indicate specific cell properties and functions, and can be used to understand disease related mechanisms. For example, Harris et al. showed that the MSD of antigen-specific T cells grows with time approximately as $t^{1.4}$, and the displacement probability distribution diverges from Gaussian (i.e. the probability of large displacements is much larger than Guassian). The large displacements help improve the efficiency of finding rare pathogens by reducing oversampling [35].

The collective migration within a confluent cell sheet preserves glassy-like dynamics. At short time, each cell is constrained by the crowding of neighboring cells and maintain fixed and solid-like property. At longer times, cell sheets flow like fluid. The transition between fluid-like and solid-like states is reminiscent of the glass transition (thus named as glassy-like dynamics). The glassy transition is determined by properties of cells and environments [44, 45, 46, 47, 48, 49]. For example, Vedula et al. showed that changing environmental constraints surrounding the cell sheet can lead to distinct migration modes. They found that cells migrating inside a narrow strip show contraction-elongation type of motion, while cells in a wide strip form large-scale vortices [47].

1.4 Development of embryonic-like tissues

During the second week of embryonic development, the embryo attaches to the uterine wall of the mother and undergoes consecutive morphological and genetic changes. By the end of second week, the amniotic cavity and yolk sac are formed and the dorsal-ventral and anterior-posterior body axes (Figure 1.1 a) are established. Specifically, at around day 5, the structure growing from a fertilized egg, referred to as blastocyst, contains a fluid-filled cavity surrounded by a layer of trophoblast cells. At one side of the cavity, there is an aggregate of cells, referred to as inner cell mass. The inner cell mass then differentiates into epiblast cells and hypoblast cells, where epiblast cells are located near trophoblast cells and hypoblast cells are near the cavity. Epiblast cells start to secret proteins and ions into cell-cell boundaries. Due to osmotic pressure balance, fluid enters into cell boundaries and drives the formation of a cavity, the amniotic cavity, inside the inner cell mass. At the same time, proteolytic enzymes secreted by trophoblast break down the extracellular matrix in the endometrium. Trophoblast cells begin penetrating into the space between endometrial cells and pulling the embryo into the uterine wall. At around day 12, cells between trophoblast and amniotic cavity differentiate into a thin and squamous membrane. The membrane, named as amniotic epithelium, is one of the four extraembryonic membranes and its appearance represents the development of dorsal-ventral body axis. The dorsal side is close to the amniotic membrane and the ventral side has columnar epiblast cells. Hypoblast cells migrate and form primary yolk sac. At the end of the second week, a longitudinal midline structure, the primitive streak, is formed at the posterior side. The formation of primitive streak represents the onset of gastrulation. During gastrulation, epiblast cells ingress along primitive streak and form definitive endoderm and mesoderm (Figure 1.2).

To understand mechanisms that drive embryogenesis and development of body axes in mammals, animal models such as embryos of mouse and cynomolgus monkey are used. In mouse model, embryos at different stages are collected from timed mating of outbred mouses or genetic mutant mouses. For cynomolgus monkey, a series of reproductive technologies, including oocyte collection, sperm injection, preimplantation embryo culture and transfer embryo into foster mother, are performed.

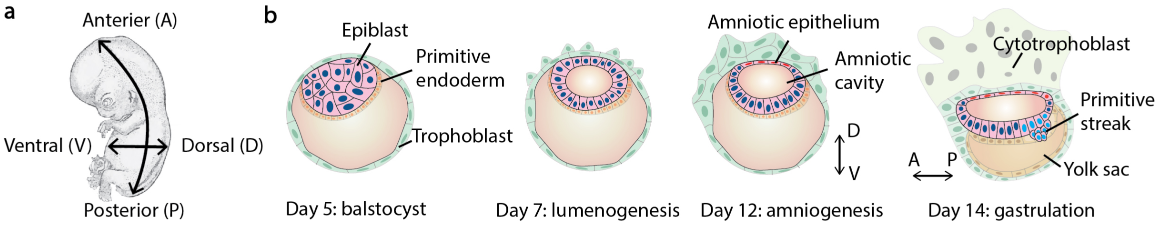

Figure 1.2: **Embryonic development during post-implantation period.** **a**, Schematic illustration of dorsal-ventral and anterior-posterior body axes. **b**, Developmental landmarks of pre-gastrulation embryonic development, including lumenogenesis, amniogenesis and gastrulation.

Afterwards, embryos are recovered from the uterus and analyzed by dissection microscopy and histological examination [4]. Based on the loss- or gain-of-function assays, it has been found that Nodal signaling, BMP/TGFβ signaling and WNT signaling are critical in the development of dorsal-ventral and anterior-posterior axes in mouse. For example, in the posterior side of mouse embryo, the extraembryonic ectoderm secretes BMP, which activates regulatory pathway of WNT and activates T expression, and later form primitive streak. At the anterior side, the anterior visceral endoderm secretes nodal antagonists CER 1 and DKK1 to regulate the epiblast patterning (Figure 1.3 a). The structure of pre-gastrulation monkey embryo is different from the mouse embryo but more similar to human embryo. Some recent immunostaining and sequencing data suggests that BMP and Nodal signaling might also play important and similar roles in regulating anterior and posterior patterning in monkey embryo (Figure 1.3 b). However, until now, no fundamental assays have been successfully conducted to confirm the role of BMP and Nodal signaling nor providing other mechanistic understanding about amniogenesis and gastrulation of monkey embryo.

Due to the limited sources of human embryos and ethical issues, synthetic embryonic models generated based on human pluripotent stem cells have been proposed as an alternative method for studying the early human development in recent years [50, 51, 52, 53, 54]. Human pluripotent stem cells, including embryonic stem cells

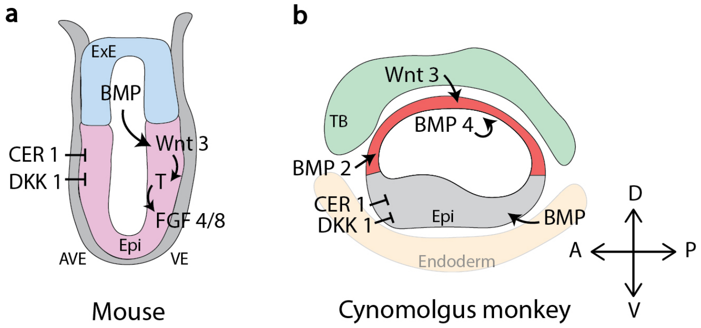

Figure 1.3: Signaling activities which lead to the spatial patterning in the embryos of **a**, mouse [3] and **b**, cytonomolgus monkey [4]. ExE: extraembryonic ectoderm; Epi: epiblast; VE: visceral endoderm; AVE: anterior visceral endoderm; TB: trophoblast.

(ESC) and induced pluripotent stem cells (iPSC) share molecular similarity with post-implantation epiblast cells, and have the ability to self-renew and give rise to all cell types of tissues and organs [55]. Yue et al. showed that human embryonic stem cells are able to self-organize into spherical aggregates and then undergo processes similar to *in vivo* lumenogenesis and amniogenesis [50, 51]. Simunovic et al. studied the spontaneous symmetry breaking and the development of anterior-posterior axis in ESC spheroids uniformly exposed to a small dose of BMP [53]. Furthermore, using microfluidic devices, Zheng et al. presented a reliable model for generating asymmetric amniotic sac by applying BMP to one side of the cell aggregates [52].

1.5 Dissertation contribution

During my PhD, I focus on developing mathematical (statistical) and computational tools to help elucidate hidden dynamics in above-mentioned three biological systems, and reveal underlying biological functions of cellular patterns or intracellular structures. Compared with the traditional biological assays, these approaches view biological observations from a different angle and provide new insights about fundamental mechanisms.

- In chapter II and III, I will discuss a multi-physics dynamical model of kinesin-mediated cargo transport. This model, for the first time, captures the 3D diffusive motions of cargo and kinesins, and their interactions within different topology MTs, with an acceptable computational cost. We demonstrated the feasibility and flexibility of the model for studying mechanisms that reduce cargo transport efficiency and lead to transport defects.

- In chapter IV, I will introduce a generalized persistent random walk model for connecting microscopic particle motion with macroscopic distribution and diffusion properties. This model, for the first time, considered the effects of angular heterogenity on particle diffusion and transport. We further discussed how the spatial dependent angular heterogeneity and the self-reinforced angular heterogeneity (with memory) lead to anomalous diffusion phenomena.
- In chapter V, I will discuss an image-based tissue profiling approach for revealing the dynamics of embryonic-like tissue development. A pipeline is developed to extract topological and intensity features from fluorescent images of embryonic tissues fixed at discrete time points. A continuous bifurcating developmental trajectory is inferred from discrete tissue samples. By mapping protein expressions to the trajectory, proteinomic variations can be acquired and used to understand factors that drive the bifurcation and symmetry breaking during development.

CHAPTER II

Intracellular Cargo Transport Influenced by Microtubule Topology

2.1 Abstract

Kinesins transport a variety of cargo along microtubules (MTs) in the cytoplasm. Although much is known about the walking of a kinesin along a single MT, the effects of the spatial distribution of MTs on kinesin-mediated transport has not been sufficiently understood and quantified. In this study, we present a 3D stochastic multi-physics model to study the dynamics of a kinesin in the presence of multiple MTs. In the model, the Brownian diffusion of the cargo, mechano-chemical dependent kinesin walking, and binding and unbinding of the kinesin are considered. Specifically, a stress-influenced chemical kinetics was used to describe changes in the walking and unbinding of a kinesin due to the intersecting MTs. In addition, the binding of a kinesin to MTs were calculated using a spatial marching method. Our model predict a significant disturbance in the transport of kinesin when the distance between two intersecting MTs is close to the radius of the cargo and the intersection angle between MTs is large. Moreover, we found that a longer kinesin is more likely to maintain the transport at the MT intersections.

2.2 Introduction

Cells rely on cytoplasmic motors to deliver important proteins and organelles to their specific locations. Kinesin-1 is a major cytoplasmic motor that walks along microtubules (MTs) to transport cargoes through crowded cytoskeletal structures. Cytoskeletal tracks such as MTs and actin filaments influence the dynamics of kinesins and the characteristics of intracellular transport [56, 57, 58]. For example, in epithelial cells, MTs form web-like networks to support endocytosis and transcytosis processes [59]. In the initial segment of the neuronal axon, MTs and actin filaments function as active filters, which selectively segregate axonal and somatodendritic components by blocking their diffusion and transport [60]. Disorganized cytoskeletal structures disrupt intracellular transport and can cause or contribute to various diseases such as amyotrophic lateral sclerosis [61, 62]. Until now, it is still not clear what are the underlying mechanisms that allow kinesins to accurately navigate through a maze of MTs. It is also critical to investigate if cells can control the delivery of intracellular proteins and organelles by adjusting the topology of the cytoskeletal network.

Several researchers have studied kinesin walking along a single isolated MT [63, 64, 65]. However, in the presence of neighboring MTs, the motion of kinesins observed in experiments is different. The transport of cargo is slowed down. Occasional switching in the walking directions and pausing are observed [7]. The multidirectional motion of cargo is usually explained as a consequence of tug of war of multiple motors [66, 67, 68], in which motors walking toward the different directions pull a common cargo in an antagonistic fashion. However, some observations in previous experiments cannot be explained by the tug of war perspective. For example, Ross et al. [7] observed that cargo transported by a single kinesin also switched its transport direction at MT intersections. By tracking cargo trajectories in vivo, the position of neighboring MTs was revealed to influence the motion of cargoes significantly [69]. Even for the same topology of MTs, cargoes of different sizes also showed different dynamics [60, 57]. Moreover, David Breuer et al. observed the wiggling behavior of cargo during the transport in cytoskeleton networks [70]. These observations suggest that other regulatory mechanisms exist to generate the diverse transport dynamics. And the dynamics is highly correlated with the interactions of motors and crowded environments.

In chapter II and III, I discuss the Monte Carlo based computational models developed to study the kinesin-mediated transport dynamics in different topology of MTs. Chapter II (single-kinesin model) focuses on the effects of the MT topology on the dynamics of a single kinesin. Chapter III (multi-kinesin model) investigates the collective transport dynamics of many kinesins inside the MT crowded environment.

In the single kinesin model, first, a mechano-chemical cycle with transition rates influenced by the stress inside the kinesin is used to describe the stochastic walking motion of the kinesin. Second, the stochastic unbinding of the kinesin from an MT is predicted by calculating the unbinding probabilities at different chemical reaction states. Third, the Brownian diffusion of the cargo and kinesin heads are considered and the stochastic binding of the kinesin to the MTs is calculated based on the spatial marching method.

The single-kinesin model provides insights into transport dynamics influenced by a neighboring MT. We found that a perpendicularly intersected MT has a considerable influence on the transport dynamics when the distance between two MTs is close to the cargo radius. In addition, MTs pointing toward different directions disrupts the transport by increasing the pausing probability. Moreover, a longer kinesin cargo linker could improve the ability of the kinesin to overcome the intersection of MTs.

2.3 Model and method

The cargo transport has two distinct modes, the active transport mode and the passive diffusion mode. When a kinesin binds to both the cargo and the MT, it walks

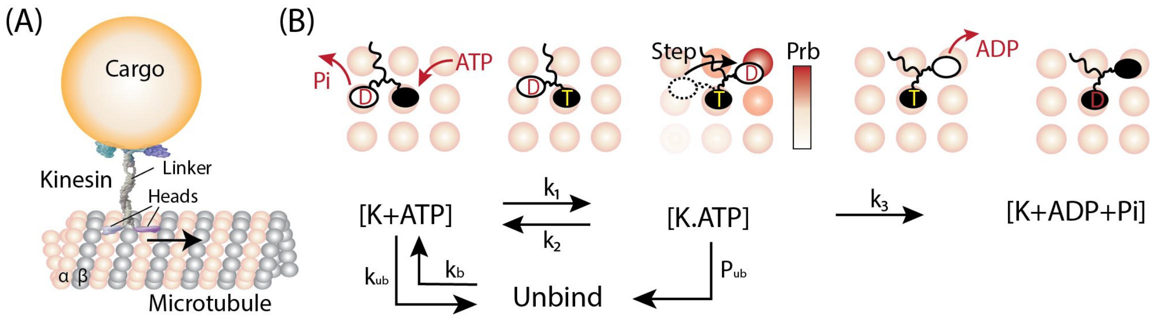

Figure 2.1: **Active transport of the cargo by a kinesin molecule along the MT.** (A) Kinesin contains a long cargo linker and two heads. Kinesin heads attach to two α-tubulin subunits on the microtubule and walks in a step-wise fashion forward. (B) The mechanochemical cycle on kinesins heads. After completing one mechanochemical cycle, kinesin moves on step (8 nm) forward.

along the MT and actively transports its cargo toward the plus end of the MT. This motion is referred to as the active transport mode. The kinesin occasionally unbinds from the MT. After unbinding, the kinesin-cargo complex moves with Brownian motion until the kinesin binds to a new binding site on the MT. This motion is referred to as the passive diffusion mode. The transition between the active transport and passive diffusion modes depends on the kinesin binding and unbinding probabilities to and from MTs.

2.3.1 Active transport

In the active transport mode, kinesin walks on the MT in a step over step fashion. In each step, an ATP is hydrolyzed and the duration of the ATP hydrolysis process is characterized by a mechanochemical cycle (composed of three states, [K+ATP], [K.ATP] and [K+ADP+Pi]), as shown in Figure 2.1. At state [K+ATP], the leading head is in the nucleotide free state and strongly bind to the MT while another head is loosely attached to the MT. Then, an ATP binds to the leading head and causes a conformational change in the kinesin molecule. At state [K.ATP], the trailing head diffuses to the next binding site and the stress caused by the conformational change is released. By dissociating ADP, the free head strongly binds to the next binding site. At state [K+ADP+Pi], the ATP on the leading head is hydrolyzed into ADP and phosphate. The probabilities of staying at states [K+ATP], [K.ATP] and [K+ADP+Pi] are denoted as P_K, P_{ATP} and P_{ADP}, respectively. These probabilities are calculated as

$$\frac{d}{dt}P_K = -k_0\, c_{ATP} P_K + k_2 P_{ATP}, \tag{2.1}$$

$$\frac{d}{dt}P_{ATP} = k_0\, c_{ATP} P_K - k_1 P_{ATP} - k_2 P_{ADP}, \tag{2.2}$$

$$\frac{d}{dt}P_{ADP} = k_2 P_{ATP}, \tag{2.3}$$

$$P_K + P_{ATP} + P_{ADP} = 1. \tag{2.4}$$

where c_{ATP} is the concentration of ATP. Transition rates k_0 and k_2 are assumed to be constants. k_1 is influenced by the magnitude of the force $\boldsymbol{F}$ in kinesin, because the most susceptible state to the external load is when the ATP releases from the MT bound head [30]. k_1 is calculated based on the equation suggested by Hendricks et al. [71] as

$$k_1 = k_{10}\, \exp\left[\frac{k_{11}(\frac{|\boldsymbol{F}|}{k_{11}} - k_{12})^2}{2k_B T}\right], \tag{2.5}$$

k_{10}, k_{11} and k_{12} are constant parameters.

At state [K.ATP], the short neck linkers of the two kinesin heads constrain the reachable binding sites of the trailing head. The force $\boldsymbol{F}$ inside the kinesin influences the probabilities of the trailing head to bind to a specific site. In 3D space, a kinesin can step along both the longitudinal and tangential directions of the MT. Therefore, the processivity of the kinesin, which is defined as the velocity of kinesin moving along the longitudinal direction of the MT, is influenced by two factors, the stepping rate (or the duration of a chemical reaction cycle) and the probability of the trailing head to bind to a forward binding site along the longitudinal direction. In particular, a

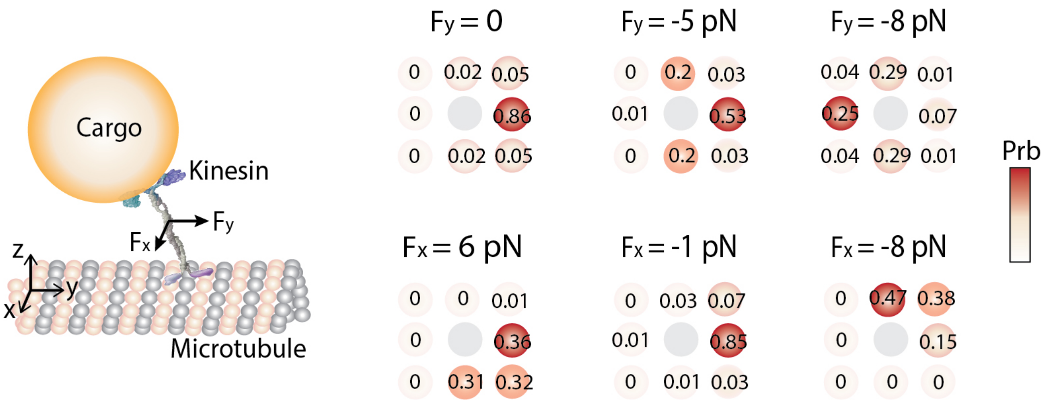

Figure 2.2: **The stepping probability influenced by force $\boldsymbol{F}$ inside the kinesin cargo linker.**

coarse-grained mechanical model proposed in previous study [72] is used to calculate the stepping probability when the stress inside the kinesin is $\boldsymbol{F}$ (Figure 2.2).

2.3.2 Passive diffusion

When kinesin unbinds from the MT, the kinesin-cargo complex moves with Brownian motion. The transnational and rotational diffusion of cargo center ($\boldsymbol{X}_c$ and $\boldsymbol{\theta}_c$) are calculated as

$$\boldsymbol{\theta}_c(t+\Delta t)-\boldsymbol{\theta}_c(t)=\boldsymbol{r}(\sqrt{2D_r\Delta t}), \tag{2.6}$$

$$\boldsymbol{X}_c(t+\Delta t)-\boldsymbol{X}_c(t)=\boldsymbol{r}(\sqrt{2D_t t}). \tag{2.7}$$

where $\boldsymbol{X}_c$ and $\boldsymbol{\theta}_c$ are the translational and rotational position of cargo center. R is the cargo radius; $\delta = 8.9\times 10^{-4} Pa\cdot s$ is the fluid viscosity of water. $D_t = \dfrac{k_B T}{6\pi R\delta}$ and $D_r = \dfrac{k_B T}{8\pi R^3\delta}$ are the transnational and rotational diffusion coefficients, respectively. $\mathbf{r}(\sigma)$ is a vector composed of normally distributed random numbers with standard deviation σ and zero average.

2.3.3 Transitions between diffusion and transport

The transition between active transport mode and passive diffusion mode is determined by the binding and unbinding of kinesin. The force dependent unbinding probability of kineins is calculated based on the Bell formula in several recent studies [73, 74, 75, 31, 76]. Bell [77] first showed that the unbinding rate between a ligand and its receptor is influenced by the force applied to pull the complex apart . The unbinding rate follows the expression $k_{ub} = k_{u0} \exp(\frac{fd}{k_B T})$, where k_{u0} is the unbinding rate without force. f is the magnitude of the force. d is the changes of the distance of the ligand and receptor from the bound state to the transition state. In our model, the unbinding probability is calculated at states [K+ATP] and [K.ATP] separately. At state [K+ADP+Pi], the unbinding probability is negligible because both kinesin heads strongly bind to the MT. The average time the kinesin spends at [K+ATP] state is at millisecond level, while the average time for state [K.ATP] is at microsecond level [78, 26]. Although the duration of state [K.ATP] is short, the unbinding probability at [K.ATP] is not negligible, because at this state the affinity between kinesin and MT is the weakest among the whole mechanochemical cycle. Thus, the unbinding probability at state [K.ATP] is calculated as

$$P_{ub} = P_{u0} \exp\left[\frac{|\boldsymbol{F}|d_0}{k_B T}\right], \tag{2.8}$$

The unbinding at state [K+ATP] is described based on an unbinding rate k_{ub} (i.e. unbinding probability per unit time). The unbinding probability P_{ub} is calculated as

$$P_{ub}(t_u) = 1 - e^{-k_{ub} t_u}, \tag{2.9}$$

$$k_{ub} = k_{u0} \exp\left[\frac{|\boldsymbol{F}|d_1}{k_B T}\right], \tag{2.10}$$

P_{u0}, d_0, k_{u0}, d_1, are constant parameters. t_u is the total time since the kinesin binds to the MT.

At each time step after unbinding, the kinesin diffuses with the cargo until it rebinds to a new track. The binding of kinesins to a single MT is usually described by a Poisson process with a constant rebinding rate k_b, which was measured in experiments to be 5 s^{-1} [79]. At the MT intersection, the binding rate is influenced by the relative positions of kinesins and MTs. Thus, the probability of a free kinesinto bind to the MTs is calculated as

$$P_b(t_b) = 1 - e^{-k_b t_b}, \tag{2.11}$$

$$k_b = k_{b0}\,\frac{V_b}{V_d}, \tag{2.12}$$

where k_b is the rebinding rate. V_b is the volume surrounding the MT where the kinesin heads can bind, which is named as accessible binding volume of kinesin (ABK); V_d is the volume where the kinesin heads can diffuse, which is named as accessible diffusion volume of kinesin (ADK). t_b represents the time interval from the kinesin unbinding moment to current time.

The MT topology influences V_b and V_d. For example, in Figure 2.3 (A), the kinesin cargo linker is fixed at position S_0 on the surface of the cargo. For kinesin heads diffusing and binding to a position on MT2 behind MT1, the kinesin cargo linker needs to wrap around the surface of MT1. Thus, ABK and ADK are restricted by the length of cargo linker and the MT topology. To numerically calculate V_b and V_d, the entire space of the system is discretized into small cubes with volume ΔV. The position of the center point of a cube is represented as $(i,\ j,\ k)$, where i, j, and k are the positions in the x-, y-, and z-directions, respectively. At time $t = 0$, point S_0 lies in one of the cubes (i.e., $S_0 = (i_0,\ j_0,\ k_0)$). The ADK volume can be computed as

$$V_d = \sum_{i,\,j,\,k} \Delta V \cdot \mathbf{1}_{L_{ijk} \leq L_c} \tag{2.13}$$

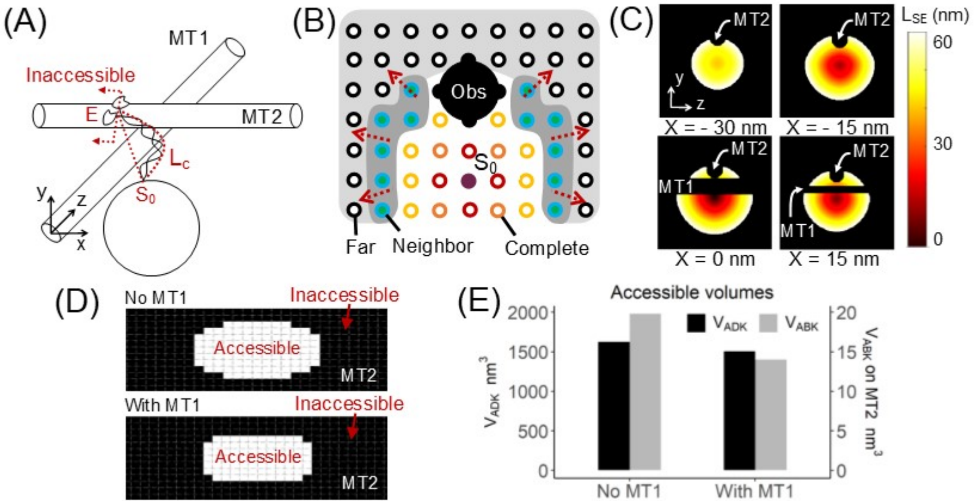

Figure 2.3: **Influence of a perpendicularly intersected MT on ADK and ABK.** (A) The spatial influence of a neighboring MT1 on the transport dynamics along MT2. In the presence of MT1, ADK and ABK are reduced because the cargo linker has to wrap around MT1 and its effective length decreases (from L_c decreases to the distance between S_0 and E); this is referred to as the shadow effect of MT1. (B) Illustration of the classification of locations used in the fast marching method in a 2D space. By solving the upwind approximation of Eikonal equation for the neighbor locations, the algorithm spatially marches out and calculates the shortest path between starting point S_0 and any other locations in the 2D/3D space. (C) Consecutive snapshots of ADK yz projections in the presence of neighboring MT1. Black color represents inaccessible regions. The color contours represent different values of L_{ijk}. (D) The change of ABK on MT2 due to the presence of neighboring MT1. The light color represents accessible binding sites, while the black represents inaccessible sites. The dotted gray lines are borderlines of binding sites. (E) Histograms of the volume of ADK and the volume of ABK around MT2 with and without neighboring MT1, which is a geometrical constraint that reduces the ratio of ABK to ADK and changes the probability of kinesin heads binding to MT2.

where $\mathbf{1}_A$ is an indicator function. L_c is the length of the cargo linker, and L_{ijk} is the length of the shortest path from the initial grid node $S_0 = (i_0,\, j_0,\, k_0)$ to grid node $(i,\, j,\, k)$, subject to the geometrical constraints caused by the MTs. The ABK volume is calculated as

$$V_b = \sum_{i,\, j,\, k} \Delta V \cdot \mathbf{1}_{L_{ijk} \le L_c \,\&\, d_{ijk} \le d_0} \tag{2.14}$$

where d_{ijk} is the shortest distance from location $(i,\, j,\, k)$ to the surface of any of the nearby MTs. Kinesin heads are assumed to be able to bind to the MT when d_{ijk} is smaller than $d_0 = 1\, nm$.

To calculate the shortest path L_{ijk}, Fermats principle was used, according to which the path taken by a light ray between two points is the path that can be traversed in the least time. Thus, the shortest path can be obtained by solving the wave equation for virtual waves traveling from S_0 to points on MT surfaces. A wave front propagates from start point $S_0 = (i_0,\, j_0,\, k_0)$ with unit propagation speed. The speed for all geometrical constraints (e.g. place inside MTs or at the MT surfaces) are set to zero. Then, time $T(i,\, j,\, k)$ required for the wave front to reach point $(i,\, j,\, k)$ can be calculated by solving the Eikonal equation [80, 81]

$$|\nabla T(i,\, j,\, k)| f_{ijk} = 1 \tag{2.15}$$

where $T(i,\, j,\, k)$ is the propagation time to reach location $(i,\, j,\, k)$. f_{ijk}, the propagation speed at location $(i,\, j,\, k)$, is 1 if location $(i,\, j,\, k)$ is outside the geometrical constraints and 0 otherwise.

The fast marching algorithm is used to solve the Eikonal equation [82]. This algorithm classifies grids in the system into complete, neighbor, and far points. Grid S_0 is labeled as complete. The grids adjacent to a complete node are classified as the neighbor points, while the remaining locations are labeled as far points. Figure 4(B) shows a schematic classification of locations in a 2D space. At each step, T values of the neighbor grids are calculated. Neighbor points with the smallest T value are updated as complete points. The T value of neighbor location $(i,\, j,\, k)$ is obtained as follows by solving the Eikonal equation [30]:

$$(max[D^{-x}_{ijk}T(i,\, j,\, k)], -D^{+x}_{ijk}T(i,\, j,\, k)])^2 + \tag{2.16}$$

$$(max[D^{-y}_{ijk}T(i,\, j,\, k)], -D^{+y}_{ijk}T(i,\, j,\, k)])^2 + \tag{2.17}$$

$$(max[D^{-z}_{ijk}T(i,\, j,\, k)], -D^{+z}_{ijk}T(i,\, j,\, k)])^2 = \frac{1}{f^2_{ijk}} \tag{2.18}$$

where D^{-x}_{ijk}, D^{-y}_{ijk}, and D^{-z}_{ijk} are the backward finite difference operators along the x-, y-, and z-directions, respectively. In more detail, the algorithm can be expressed as follows.

1) Initialization

Location $(i_0,\, j_0,\, k_0)$ is labeled as a complete location because $T(i_0,\, j_0,\, k_0) = 0$ from the beginning. All the locations adjacent to the complete location (i.e., locations $(i_0 \pm 1,\, j_0 \pm 1,\, k_0 \pm 1)$) are labeled as neighbor points, while the remaining locations are labeled as far points.

2) Marching Loop

a) $T(i,\, j,\, k)$ is calculated for all locations $(i,\, j,\, k)$ labeled as neighbor points. Next, locations $(i_m,\, j_m,\, k_m)$ with the lowest T value among the newly calculated T values are determined. Then, the label at location $(i_m,\, j_m,\, k_m)$ is labeled as complete.

b) If grids $(i_m \pm 1,\, j_m \pm 1,\, k_m \pm 1)$ are labeled as far points, their labels are updated as neighbors.

3) Repeat the previous step (i.e., marching loop) until any location labeled as neighbor reaches the boundary of the modeling space. Because a unit propagation speed is used, $T(i,\, j,\, k) = L_{ijk}$, which is the length of the shortest path between $(i_0,\, j_0,\, k_0)$ and $(i,\, j,\, k)$.

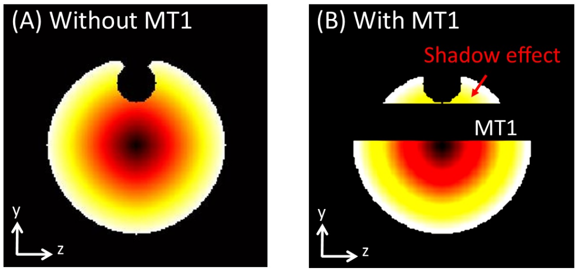

Figure 2.4: **ADK influenced by a neighboring MT.** (A) Without a neighboring MT (MT1 in Figure 2.3), the available diffusion volumes and available binding positions are large. (B) The shadow effect of MT1. Available diffusion volumes surrounding the original MT (MT2 in Figure 2.3) and the available binding positions on the original MT are reduced.

Figure 2.3 (C) shows an example of ADK calculated using the fast marching method. In the calculation, two MTs are perpendicularly attached. Starting point $S_0 = (i_0, j_0, k_0)$ is the location where the cargo linker binds on the cargo. The color map represents the values of L_{ijk} at each location (i, j, k). The black region represents the inaccessible locations (i.e., locations in the MTs and locations where $L_{ijk} > L_c$). In the absence of MTs, the shape of the accessible diffusion region is a sphere. When the cargo is close to the MT intersection, a longer distance is required to reach the regions behind an MT because the cargo linker will wrap around the surface of the MT. Thus, for example, in the third snapshot in Figure 2.3 (C), the size of the accessible region behind MT1 and surrounding MT2 is reduced compared to the size in the absence of MT1. A comparision of the ADKs with and without an intersecting MT (MT1) is shown in Figure 2.4.

This reduction of the accessible region due to an MT is referred to as the shadow effect because this phenomenon is similar to the shadow area behind an object due to the diffraction of light. By using the fast marching method, we accurately calculated the shadow effect of the neighboring MT (Figures 2.3 (D) and (E)). The results indicate that approximately 30% of the ABK on the original MT (namely MT2) becomes inaccessible. The volume of ADK is also reduced by approximately 10%. In addition, new binding sites on the neighboring MT1 are accessible. Therefore,

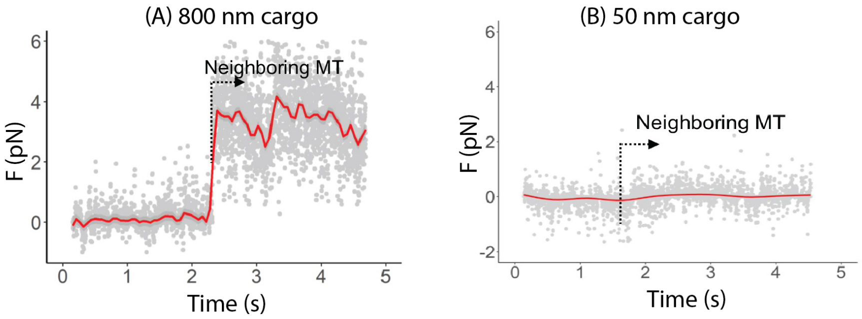

Figure 2.5: **Force $\boldsymbol{F}$ inside kinesin cargo linker.** The gray dots represent the magnitude of $\boldsymbol{F}$ obtained through the model and the red line shows the trend of data acquired by fitting the data with smooth splines. Before the cargo reaches the intersected MT (i.e., $t < 2.3s$ in (A) and $t < 1.8s$ in (B)), the force in the cargo linker fluctuates around 0 pN. The variation in the force is caused by the kinesin walking. (A) For a large cargo, after the kinesin meets the intersected MT, the magnitude of $\boldsymbol{F}$ increases significantly owing to the interference between the cargo and the two MTs. (B) For a small cargo, the interference between cargo and MTs has negligible effects on the force $\boldsymbol{F}$.

the probability of binding to the original MT2 and maintaining the previous walking direction decreases, while binding to the intersecting MT1 becomes probable.

2.3.4 Force inside kinesin

The effective length of the kinesin motor is approximated by the distance between the center of the two heads and the end of the cargo linker as $|\boldsymbol{X}_k - \boldsymbol{X}_h|$, where $\boldsymbol{X}_k$ is the binding position between kinesin cargo linker and cargo surface (e.g. S_0 in Figure 2.3); $\boldsymbol{X}_h$ is the position of the center of two kinesin heads. The force inside the kinesin caused by the extension of the kinesin motor is calculated as

$$\boldsymbol{F} = \frac{\boldsymbol{X}_k - \boldsymbol{X}_h}{|\boldsymbol{X}_k - \boldsymbol{X}_h|}(|\boldsymbol{X}_k - \boldsymbol{X}_h| - L_k)S_k, \tag{2.19}$$

where L_k is the unstretched length of the kinesin motor, and S_k is the stiffness of the cargo linker. Note that, a cable-like linker is used in the model, because it was observed in previous experiments that the stiffness of kinesin is an order of

Unstretched length L_k	60 nm	Stiffness S_k	0.3 pN/nm
Chemical reaction k_0	0.0283 $\mu M^{-1}s^{-1}$	Unbinding k_{u0}	$2.65 \times 10^{-6}s^{-1}$
Chemical reaction k_2	98.875 s^{-1}	Unbinding P_{u0}	0.01
Chemical reaction k_{10}	32.921 s^{-1}	Unbinding d_0	0.0054 nm
Chemical reaction k_{11}	3.302 pN/nm	Unbinding d_1	1.064 nm
Chemical reaction k_{12}	1.2114 nm	Rebinding k_{b0}	$1.3 \times 10^4 s^{-1}$

Table 2.1: Parameters of the model.

magnitude lower for compression than for stretching [83]. In other words, $\boldsymbol{F} = \boldsymbol{0}$ when $|\boldsymbol{X}_k - \boldsymbol{X}_h| \leq L_k$.

k_1, k_{ub}, and P_{ub} are influenced by $\boldsymbol{F}$ according to Equations 2.5, 2.8 and 2.10. As a result, large $\boldsymbol{F}$ slows down the transport and reduces the length kinesin can walk before unbinding. Intracellular obstacles, such as MTs and proteins, can perturb cargo diffusion and increase $\boldsymbol{F}$. For example, when an 800 nm cargo encounters a perpendicularly intersected MT, $\boldsymbol{F}$ increases to around 3.5 pN. Owing to the large force in the cargo linker, k_1, k_{ub}, and P_{ub} increase. Thus, in front of an intersecting MT, kinesin walks slower and is more likely to unbind from the original MT. The influences of the intersecting MT on force $\boldsymbol{F}$ is size dependent. For small-sized cargoes (e.g. 50 nm cargoes), they diffuse faster and are less likely to be trapped at the MT intersection. Thus, force $\boldsymbol{F}$ acting on the small cargo is relatively small (Figure 2.5 (B)). Therefore, the cargo size can significantly influence the walking velocity and unbinding probabilities of kinesin near a MT intersection.

In addition, a comprehensive algorithm used to calculate the walking motion of kinesin influenced by the force $\boldsymbol{F}$ is provided as Algorithm 2.6.

2.4 Results

2.4.1 Parameters acquisition and model validation

When kinesin walks on a MT, the walking velocity and run length under various external loads are measured in the experiments using optical tweezers [5, 6]. The

```
Input: $P_K$, $P_{K.ATP}$, $\boldsymbol{X}_h$, $\boldsymbol{F}$, $r_1$, $r_2$, $state$
  if $state = 1$ then
    Update $P_K$ and $P_{K.ATP}$ based on Eqs. 2.1 - 2.4
    if $P_K \leq r_1$ then
      $state \longleftarrow 2$
    end if
  else if $state = 2$ then
    Update $\boldsymbol{X}_h$ based on $\boldsymbol{F}$ and the stepping probabilities in Figure 2.2.
  else
    Update $P_K$ and $P_{K.ATP}$ based on Eqs. 2.1 - 2.4
    if $P_{K.ATP} + P_K \leq r_2$ then
      $(P_K,\ P_{K.ATP},\ state) \longleftarrow (1,\ 0,\ 1)$
      $(r_1,\ r_2) \longleftarrow i.i.d\ Uniform(0,1)$
    end if
  end if
Output: $P_K$, $P_{K.ATP}$, $\boldsymbol{X}_h$, $r_1$, $r_2$, $state$
```

Algorithm. 2.6: **The walking motion of a kinesin.** r_1 and r_2 are identical and independent random variables uniformly distributed between 0 and 1. When the kinesin binds to the MT, P_K is set to be 1, $P_{K.ATP}$ is set to be 0 and *state* is set to be 1.

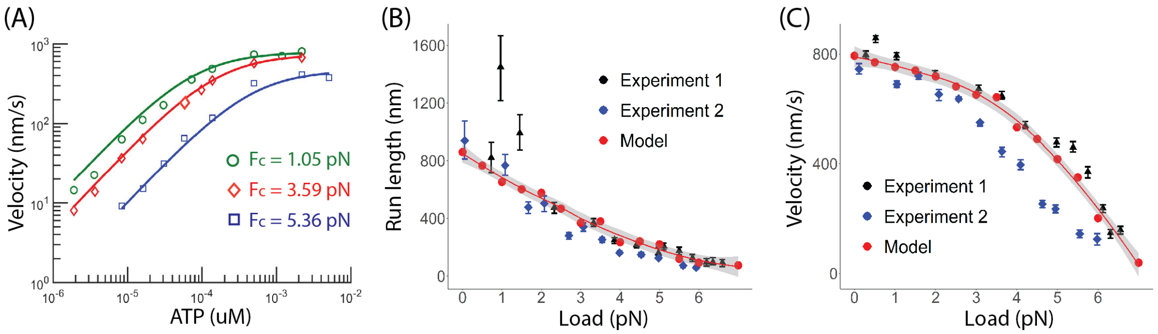

Figure. 2.7: **The walking dynamics of a kinesin on a single MT.** (A) The walking velocity of kinesins over various ATP concentrations is predicted. The circles, diamonds, and squares represent the experimentally measured data [5], and the solid lines represent results of the model. (B) The walking velocity over various loads acting on the cargo when the ATP concentration is 2 mM. The triangles and diamonds represent experimentally measured data (experiment 1 [5], experiment 2 [6]). The dots and solid lines represent results obtained through the model, and the gray bands indicate 95% confidence interval of the results of the model. (C) Run length over various loads.

model is fitted to the force-velocity curves, force-run length curves and velocity-ATP concentration curves to acquire values of parameters k_0, k_{10}, k_{11}, k_{12}, k_2, k_{u0}, d_0, P_{ub} and d_1. The parameter values are shown in Table 2.1 and the fitting results are shown in Figure 2.7.

When the kinesin is close to the MT intersection, the binding and unbinding probabilities of the kinesin can differ from the probabilities when the kinesin is far from the intersection. To evaluate the changes of binding and unbinding rates due to a MT intersection, previous observations on kinesin motion near 90° MT intersections are used [7]. Figure 2.8 (A) shows the topology of the MT intersection in the model and experiment. The bottom MT is bound to a glass slide via proteins whose length is 135 nm. The glass slide is considered as a reflective boundary. The top MT is perpendicularly attached to the surface of the bottom MT. The diameter of an MT is set to be 25 nm [84]. The length of a MT varies from several hundred nanometers to several micrometers [85]. In this study, the length of an MT is determined as 4

μm to prevent the dynamics of kinesins near the intersection from being influenced by the length of the MT. For a green fluorescent protein (GFP) cargo, the diameter of the cargo is determined as 50 nm. For a bead cargo, the diameter of the cargo is determined as 800 nm [7].

First, the motions of the kinesin when it passes the intersection by walking on the bottom and top MT are named as underpass and overpass, respectively. Second, the motion of the kinesincargo complex near the MT intersection is classified into four types of dynamics: pass, pause, switch, and dissociate. If the cargo unbinds from an MT and does not rebind to any of the two MTs for 1 s or longer, that motion is defined as a dissociation. For a GFP-bound kinesin, the two criteria (i.e., 1 s and 300 nm) are used to differentiate motions. Specifically, the pass dynamics is defined as the motion of a kinesin when it passes through the intersection and moves 300 nm further on the same MT in 1 s. The switch dynamics describes the motion when the kinesin reaches the intersection and moves 300 nm further on a different MT in 1 s. If the kinesin stays near the intersection for 1 s or longer, the motion is defined as pause. When the kinesin transports the cargo with a diameter of 800 nm, the time and distance criteria used are 3 s and 1 μm. For example, passing is the motion when the kinesin passes through the intersection and moves 1 μm further on the same MT in 3s.

Experimental data of a GFP-bound kinesin underpassing the intersection is used to obtain the unbinding and rebinding rates k_{u0} and k_{b0} at the intersection. The result of fitting is shown in Figure 2.8 (B). The other three experimental results (i.e., GFP-bound kinesin overpassing the intersection, kinesin bound to an 800-nm cargo underpassing and overpassing the intersection) are used to validate our model, as shown in Figure 2.8 (C). The probabilities of passing, pausing, switching and dissociation are calculated by performing 100 simulations.

When the kinesin transports a small cargo, such as a GFP, the effect of a neighbor-

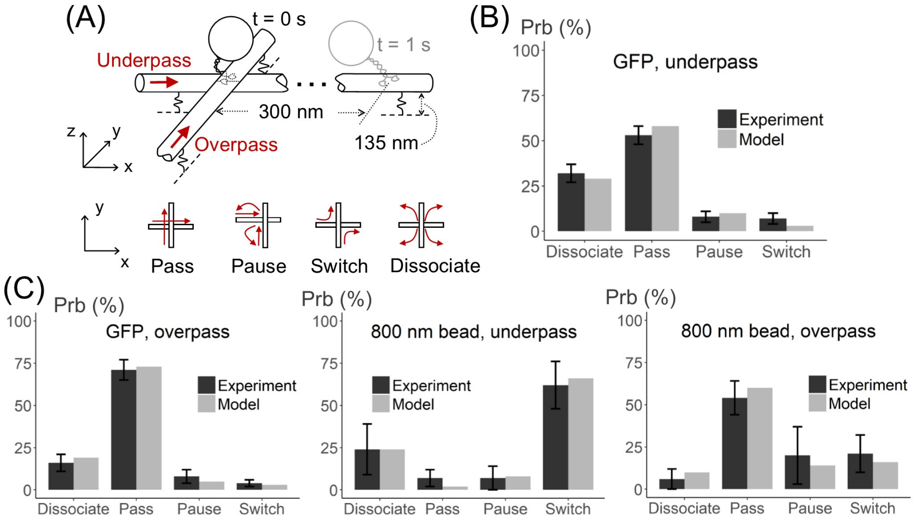

Figure. 2.8: **Transport dynamics at a 90° MT intersection.** (A) Spatial organization of MTs and four types of transport dynamics (passing, pausing, switching and dissociation) predicted by the model and observed in experiments in [7]. The bottom MT is 135 nm above a glass slide (numerically represented as a reflective boundary condition). Projecting on the xy plane, four types of dynamics are defined based on the motion of kinesins, represented by arrows. (B) Model training; experimental data of the GFP-bound kinesin starting from the bottom MT is chosen as the training set to fit the model parameters. (C) Model validation; the fitted model predicted similar transport dynamics through the validation dataset (GFP-bound kinesin overpassing the intersection, and the kinesin bound to an 800-nm cargo underpassing and overpassing the intersection).

ing MT on the motion of the kinesin cargo complex is small. The Brownian motion of the cargo does not change considerably because of the neighboring MT. Force $\boldsymbol{F}$ fluctuates around 0 pN (Figure 2.5 (A)). The active transport velocity and unbinding probability are less influenced. Thus, the passing probability is larger than 0.5. And the probabilities of passing, pausing, switching and dissociation are similar in both underpass and overpass situations, as shown in Figure 2.8 (B) and (C). In addition, compared to a large cargo situation, the probability of dissociation is relatively large because small cargo diffuses faster and is likely to move away from the two MTs and dissociate.

When the kinesin transports a large cargo with a diameter of 800 nm near the intersection, the neighboring MT disrupts the cargo motion and changes the active and passive modes. The dynamics in the underpass and overpass are different. In the underpass situation, the neighboring MT increases the unbinding of kinesin from the original MT. The ABK on the original MT is reduced and more binding sites on the neighboring MT are accessible to the kinesin. Thus, kinesin is more likely to switch to the neighboring MT. In the overpass situation, the cargo is above the two MTs. Force $\boldsymbol{F}$ in the cargo linker and the accessible binding sites on the original MT are less influenced. Thus, the probability of passing the intersection is high. Note that the effects of the cargo size on the ratio of ABK and ADK are very small because this ratio is mostly affected by the cargo linker length and MT diameter. However, the size of cargo can influence force $\boldsymbol{F}$ inside the cargo linker (Figures 2.5 (B)). For example, when a large cargo is trapped at the MT intersection in the underpass situation, the magnitude of $\boldsymbol{F}$ increases, the walking velocity is reduced, and the unbinding probability of the kinesin is increased. Therefore, the dynamics of an 800 nm cargo is different from the dynamics of a GFP cargo in the underpass situation.

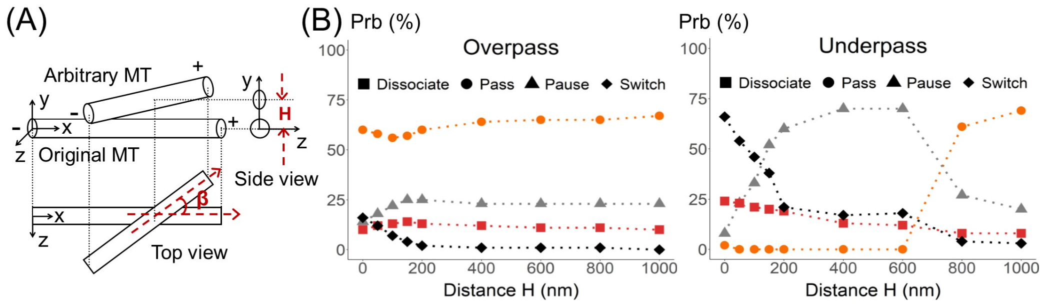

Figure. 2.9: **Influence of distance *H* between two intersected MTs on the transport dynamics.** (A) The relative position of the two MTs is characterized by distance *H* between the center lines of the two MTs and polarity difference β. (B) Transport dynamics over *H*. The shape and color of the markers represent the four types of dynamics (pass, pause, switch and dissociation).

2.4.2 Influence of an arbitrary microtubule

The position of an arbitrary neighboring MT can be characterized by the distance H and polarity difference β (Figure 2.9 (A)). Polarity difference β is defined as the angle between two intersected unidirectional MTs. When the polarity of two MTs is the same, $\beta = 0°$. When the two MTs are aligned in the opposite directions, $\beta = 180°$. H is defined as the distance between the center lines of the two MTs minus the radius of two MTs. When the MTs are linked through cross-bridge proteins in vivo, distance H varies from 0 to 100 nm [86]. In the absence of the cross-bridge proteins, H can vary over wider ranges, from hundreds of nanometers to several micrometers. When the cargo of interest has a diameter of 800 nm, the value of H smaller or similar to 800 nm can interrupt the transport. Thus, in this study, H ranges from 0 to 1,000 nm. Figure 2.9 (B) shows the change in the transport dynamics over distance H. In the overpass situation, H has a small influence on the transport. In this case, kinesins are likely to pass the intersection and maintain the transport direction. The variations in the probabilities at small H values are caused by the interrupted Brownian motion of the cargo.

In the underpass situation, the transport dynamics are significantly affected by

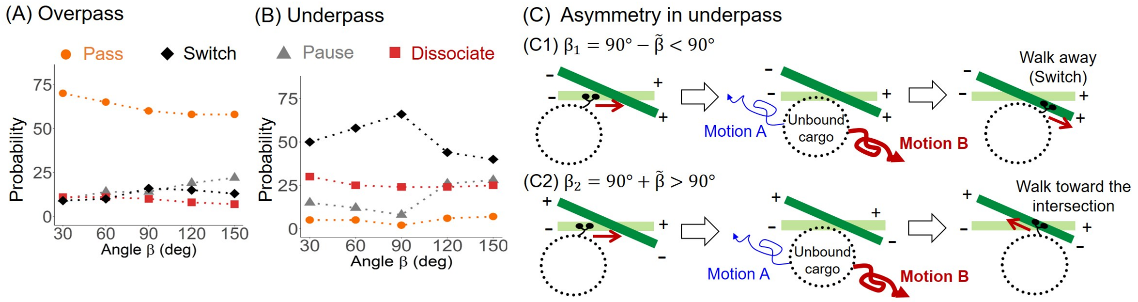

Figure. 2.10: **The influence of polarity difference β between two intersected MTs on the transport dynamics.** (A, B) Probabilities of passing, pausing, switching and dissociation at the intersection. (C) The schematic illustration of the asymmetric motion with respect to $\beta = 90°$ in the underpass situation. The unbound cargo-kinesin complex tends to move with Brownian motion B rather than motion A. When the kinesin rebinds to the top MT, it walks toward the intersection when $\beta > 90°$ and walks away from the intersection when $\beta < 90°$. When the kinesin reaches the MT intersection again, it could pause, dissociate, or switch.

H. That is, when $H < 400\,nm$ (i.e., smaller than the cargo radius), the number of accessible binding sites on the original MT is reduced, whereas the number of accessible binding sites on the neighboring MT is increased. The probability of switching to the neighboring MT is large. When $H > 400\,nm$, the accessible binding sites on both MTs are reduced. The probability of switching decreases and the probability of pausing in front of the neighboring MT increases.

MT polarities play an important role in axonal growth and guidance. Inside the growth cone of a healthy neuronal axon, MTs are aligned parallel to the axonal axis. In impaired neuronal axons, more than a half of the MTs are distributed with intersection angles larger than 30° [87]. This distribution interrupts the transport of intracellular cargoes such as mitochondria and vesicles. Then, the axons stop growing and their growth cones convert into retraction-bulb-like structures. These experimental observations suggest that MTs organized with a large polarity difference affect the cargo transport and axonal regeneration process. Here, our model predicts how the polarity difference β changes the cargo transport dynamics. Figures 2.9 (A) and (B) show the quantitative evaluation of the effects of intersection angle β. In the overpass situation, the motion of cargo is less influenced by the intersecting MT. Kinesin is likely to walk on the original MT and pass the intersection. In the underpass situation, kinesin frequently switches between two MTs owing to the shadow effect of the neighboring MT. The switching probability is large. When $\beta = 90°$, the switching probability is the largest because once the kinesin binds to the neighboring MT, the cargo is transported away from the original MT. The probability of the kinesin switching back to the original MT is small. Moreover, the switching probabilities are not symmetric with respect to $\beta = 90°$. The switching of kinesin depends on the unbinding motion, rebinding motion, and rebinding position. The unbinding of kinesin is affected by the topology of the intersection. Suppose $\tilde{\beta}$ is the angle between 0° and 90° . Then, the MT intersection with angle $\beta_1 = 90° - \tilde{\beta}$ and the MT intersection with $\beta_2 = 90° + \tilde{\beta}$ are symmetric about 90° . For both β_1 and β_2, the topology of the intersections are the same, as shown in Figure 2.10 (C). Thus, both MT intersections affect the unbinding of kinesin with the same amount. However, effects of the intersections on the rebinding of kinesin are different. When the kinesin unbinds at the intersection, its cargo could move with Brownian motion A or move with Brownian motion B, which are depicted in Figure 2.10 (C). However, the unbound cargo is more likely to move with motion B due to the interference between the cargo and the MTs. When $\beta = \beta_1 (< 90°)$, the cargo is likely to rebind on a point close to the plus end of the top MT, as shown in Figure 2.10 (C1). Then, the kinesin walks away from the intersection, which can be classified as switch motion. In contrasts, when $\beta = \beta_2 (> 90°)$, the cargo is likely to rebind on a point close to the plus minus of the top MT, as shown in Figure 2.10 (C2). Then, kinesin walks toward the intersection again. Thus, this walking motion reduces opportunity of switching. This difference leads to the asymmetric switching in the underpass situation.

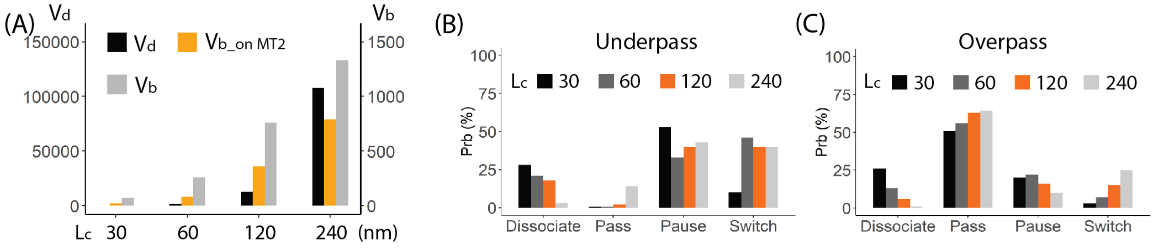

Figure. 2.11: **Influence of cargo linker length L_c on the shadow effect and transport dynamics.** (A) The cargo and kinesin heads are connected through the cargo linker. (B) The volumes of ADK and ABK increase with the cargo linker length. (C) The probabilities change over the cargo linker length both for underpass and overpass situations. In the model, the kinesin transports 800 nm cargo toward a 90° intersection. The distance between two intersected MTs is 100 nm. A longer cargo linker reduces the shadow effect of a neighboring MT and increases the passing and switching probabilities.

2.4.3 Influence of the cargo linker length

The shadow effect of a neighboring MT is not only influenced by the position of the MT but also by the MT diameter and cargo linker length. Although the diameter of MTs is almost constant, the cargo linker length can differ depending on the type of molecular motors. For example, myosin has a longer cargo linker of approximately 160 nm, including the head and tail domain. Myosin can walk on the actin filaments through very complicated dynamics [88]. For the same type of motor, the cargo linker length can change with mutations [89]. This section quantitatively describes the effect of the cargo linker length on the shadow effect and transport dynamics.

Figure 2.11 shows the variation in the volumes of ABK and ADK and changes in the passing, pausing, switching and dissociation probabilities at the intersection over different cargo linker lengths L_c. With a longer cargo linker, kinesin heads can diffuse further to explore available binding positions. In the overpass situation with a short cargo linker length, the probabilities of dissociation and pausing are large, and the probabilities of passing and switching are small. When the cargo linker length increases, kinesin is more likely to reach the binding sites even when the cargo is not close to the MTs. Thus, the probability of dissociation decreases and the passing and switching probabilities increase. In the underpass situation, the transport dynamics is very complicated because the cargo linker length influences the reachable binding positions and the probability for a cargo encountering a neighboring MT when the kinesin is still away from the MT intersection point. Our model predicts the decrease in the probability of dissociating over the cargo linker length and the increase in the probability of passing. The probabilities of pausing and switching show nonmonotonic changes.

Overall, a kinesin (or other type of motors) with a short cargo linker is susceptible to the neighboring MT. The increase of the cargo linker length may potentially help a kinesin overcome the hindrance effect of the neighboring MT but also bring complexity in transport dynamics.

2.5 Conclusions

In the present study, we developed a 3D multiphysical model to study the microscopic dynamics of a kinesin-mediated transport influenced by a neighboring MT. Our model accurately captured the interference of a neighboring MT on kinesin walking, binding and unbinding dynamics, and predicted several key mechanisms of the kinesin-mediated transport.

First, the perpendicularly intersected MT affects the mechano-chemical cycles on kinesin heads by increasing the stresses in the cargo linker. The speed of the cargo transport decreases, and the kinesin unbinding occurs frequently. Moreover, cargoes in a MT-crowded environment move in different manners compared to the Brownian diffusion with external drifting force. The velocity and direction of cargo transport highly depends on the topology of the MT intersection, cargo linker length, and cargo size.

Second, a neighboring MT influences the transport characteristics, such as the pause-and-go choice and transport direction. The shadow effect of a neighboring MT reduces the number of available binding sites on the original MT and increases the probability of switching to other MTs. Moreover, our model quantitatively predicted the effects of an arbitrary neighboring MT on the transport. The effects are considerable when the distance between two MTs is similar to the cargo radius and the polarity difference is large. Furthermore, we showed that the disruption of a neighboring MT can be reduced if the cargo linker is longer.

Our work discussed the effects of a neighboring MT on the comprehensive cargo transport dynamics at the molecular scale. The phenomena, such as the influence of the separating distance and the intersection angle on the passing and switching probabilities, predicted by our model are necessary for future studies of transport through the cytoskeleton network. Our model can be further improved to study the transport by multiple kinesins in the presence of several MTs and obstacles. Effects of intracellular particles, such as proximal cargoes or large-size proteins, can also be predicted by including the interactions between cargoes and the particles. In addition, it is worthy to note that this model can be extended to investigate how the evolution of the cytoskeleton structures modulates the intracellular transport.

CHAPTER III

Collective Transport by Multiple Kinesins

3.1 Abstract

The transport of intracellular organelles is accomplished by groups of molecular motors, such as kinesin, myosin and dynein. Previous studies have demonstrated that the cooperative activity of kinesins on a track is beneficial for long transport. However, within crowded three-dimensional (3D) cytoskeletal networks, surplus motors could impair transport and lead to traffic jams of cargos. A complete understanding of the interaction between molecular motors and tracks and the resulting changes in the 3D cargo transport dynamics are still elusive. In this work, a novel 3D stochastic dynamic model is introduced to study the synergistic and antagonistic motions of kinesin motors walking on multiple mircotubules (MTs). The model shows that multiple kinesins attached to a common cargo interact mechanically through the transient forces in their cargo linkers. Under different environmental conditions, such as different MT topologies and kinesin concentrations, the number of kinesins connecting between the cargo and the MTs, the transient forces in the kinesins, and the stepping frequency and unbinding probabilities of kinesins are changed substantially. Therefore, the macroscopic transport properties, including the stall force of the cargo, the transport direction at track intersections, and the mean square displacement (MSD) of the cargo along the MT bundles vary with the environmental conditions. In gen-

eral, conditions that improve the synergistic motion of kinesins increase the stall force of the cargo and the capability of maintaining the transport. In contrast, the antagonistic motion of kinesins temporarily traps the cargo and slows down the transport. Furthermore, this study predicts an optimal number of kinesins for the cargo transport at MT intersections and along MT bundles.

3.2 Introduction

Many cellular processes, such as mitosis, the transport of proteins and organelles, and the beating of cilia and flagella, are driven by molecular motors [90, 91]. Although an individual motor protein can produce continuous motion, most intracellular processes require multiple motors to function in a cooperative manner [92, 93]. During the last decade, the cooperative cargo transport by multiple motors along a single track, such as a microtubule (MT) or a filament, has been well-characterized through experiments and mathematical models [26, 94, 95, 96, 79]. These studies suggest that the cooperative dynamics of motors along a track improves the reliability and efficiency of the transport because multiple motors generate large pulling forces on the cargo and help it overcome the intracellular obstacles such as MT associate proteins in the highly viscous cytoplasm [97, 73, 74].

However, several experiments observed sluggish cargo motions when multiple motors transport a cargo on intersecting tracks. Schroeder et al. [98] showed that cargoes transported by myosin V and dynein-dynactin are likely to be trapped at the intersection of two filaments. Ross et al. [7] observed the trapping of cargoes at the MT intersection by multiple kinesins. During the temporary trapping intervals, Gao et al.[99] showed that the intracellular cargo exhibits rapid and directional rotation driven by molecular motors. On bundles of multiple MTs, Stepanek et al. [100] observed the existence of distinct anterograde and retrograde transport modes. When a faster transport caught up with a slower one moving in the same direction, they would progress together at the same speed.

In addition, the concentration of motors influences the transport dynamics. Neri et al. [101] showed that when the motion of the cargo is dominated by a large number of kinesins, the heterogeneity of cargo distribution depends on the complexity of the entire track network. When few motors are involved in the transport and the cargo can easily unbind from the track, the cargo distribution is influenced only by the local track topology. Shubeita et al. [102] found that the average transport velocity of the lipid droplets in the embryos is around 5.5% higher when the concentration of the kinesin is reduced. Other studies observed traffic jams of cargoes along MTs when the motor density exceeds a critical value [103, 104, 105]. These observations suggest that the transport speed and distance of the cargo may not necessarily be improved by a large number of motors in dense MT networks. Considering that the force generated by a single motor is not sufficient to overcome the load fluctuations on a cargo, an optimal concentration of motors could exist for achieving fast and robust transport on multiple MTs.

To elucidate the complex transport dynamics, this chapter is going to discuss using a 3D stochastic dynamical model (named multiple kinesin model) to study the collective behavior of multiple kinesins on multiple MTs. The multiple kinesin model captures transient dynamics of the walking motion of each single kinesin, as well as the interactions among all kinesins, their common cargo and MTs. The model predictions are verified based on the distribution of the stall force along a MT and the transport dynamics at a 90° intersection of two MTs measured in previous experiments [7]. The stall force is affected by the non-uniform distribution of external loads among all bound kinesins (explicitly, kinesins that bind and walk on a MT). The transport direction at a 90° intersection of two MTs is likely to be switched when one MT disrupts cargo diffusion and the free kinesins bind to the intersecting track. Next, the collective transport of the cargo by different number of kinesins in different MT topologies was studied. Fixing the number of kinesins on the cargo, two perpendicularly intersecting MTs with intermediate separating distance are shown to have the largest influence on the transport. Inside the same topology of MTs, an intermediate number of kinesins achieves the largest switching and passing probabilities at the 90° MT intersection, and the fast cargo mobility (characterized by the mean square displacement) along the MT bundle. Analysis of the microscopic dynamics of kinesins further helps to illustrate that the impairment of the transport at a large number of kinesins comes from the antagonistic motion of the kinesins that are lagged behind the center of the cargo. Moreover, the transport along a MT bundle interrupted by a neighboring MT was investigated.

3.3 Model and method

3.3.1 Algorithm overview

Consider the case where N identical kinesins are uniformly distributed on the surface of a spherical cargo. The connection between cargo and kinesins are assumed to be intact. Kinesins can bind to and unbind from the MTs. When a kinesin binds to and walks on the MT, it exerts force and moment to the cargo. Thus, kinesins interact mechanically and cargo undergoes Brownian motion influenced by the total force and moment generated by bound kinesins.

To study the collective dynamics of multiple kinesins, most previous modeling works focus on the one dimensional (1D) motion along the axial direction of a single MT. Assuming the velocity, binding and unbinding rates are constants, the probability of having n bound motors at time t was described by a continuous time Markov process [73, 106, 32, 107]. Several studies further considers the fact that a motor cannot bind to positions occupied by other motors. Therefore, the distribution of motors on the MT is described by the totally asymmetric simple exclusion process (TASEP)

[103, 104, 105, 108]. However, since the properties of the kinesin are influenced by the force it experiences [109, 78] and the force fluctuates due to the cargo diffusion and the interactions between kinesins and MTs, Monte Carlo based computational models were proposed to include the force dependent stepping rates and unbinding rates of kinesins [75, 89, 110, 111]. For example, the stepping motion of a kinesin can be modeled as a Poisson process with a rate exponentially decaying with the force[75]. The force dependent unbinding rate are modeled based on the Bell model [77]. Combining the Monte Carlo model with the experiments, it was shown that the transport by pairs of kinesin-1 and kinesin-3 is dominated by the motion of kinesin-1 because kinesin-1 walks slower and has a smaller unbinding probability than kinesin-3 [75]. Blackwell et al. [112] considers the forward and backward stepping motion of motors and modeled the stepping rate through an energy perspective. They found that the Brownian ratchet-like dynamics of motor stepping (specifically, the asymmetric forward and backward stepping rates) lead to fast cargo transport. Recently, Bergman et al. [31] developed a 3D dynamical model to study the effects of a MT intersection on the transport and predict the transport directions.

In this work, there are three major improvements compared to previous models. 1) The MTs are modeled as cylinders with discrete binding sites distributed on the surface of the MT. The 3D stepping motion of kinesins influenced by the force along the axial and tangential direction of the MT is considered. 2) The geometrical constraint of the MTs on kinesin binding and cargo diffusion is considered. 3) Kinesin stepping motion is described by the mechanochemical cycle on its heads. The influence of the force on the chemical reaction speed and the unbinding probability are modeled separately at different chemical reaction states. Specifically, the model considers that the most susceptible state to the force is when the ATP releases from the MT bound head, as suggested by previous experimental findings [30]. In addition, the influence of ATP concentration on the kinesin dynamics is included. Note that the dynamics

```
Input: For all kinesins $i = 1, 2, ..., N$:
            $(P_{Ki},\ P_{ATPi},\ P_{bi},\ P_{ubi},\ t_{bi},\ t_{ubi}) \longleftarrow (1,\ 0,\ 0,\ 1,\ 0,\ 0)$
            $(state\_i,\ onMT\_i) \longleftarrow (1,\ 0)$
            $(\boldsymbol{F}_i,\ \boldsymbol{M}_i) \longleftarrow (\mathbf{0},\ \mathbf{0})$
            $(r_{1i},\ r_{2i},\ r_{bi},\ r_{ubi}) \longleftarrow i.i.d\ Uniform(0, 1)$
        For cargo: $(\boldsymbol{\theta}_c,\ \boldsymbol{X}_c)$
  for $t = 1$ to $N_t$ do
    $(\boldsymbol{\theta}_c, \boldsymbol{X}_c) \longleftarrow$ Diffuse$(\boldsymbol{\theta}_c, \boldsymbol{X}_c, \boldsymbol{F}_1, \boldsymbol{F}_2, ..., \boldsymbol{F}_N, \boldsymbol{M}_1, \boldsymbol{M}_2, ..., \boldsymbol{M}_N)$
    for $i = 1$ to $N$ do
      if $onMT\_i > 0$ then
        $t_{ubi} \longleftarrow t_{ubi} + 1$
        $(\boldsymbol{F}_i,\ \boldsymbol{M}_i) \longleftarrow$ Force$(\boldsymbol{X}_{hi}, \boldsymbol{\theta}_{ki}, \boldsymbol{X}_c, \boldsymbol{\theta}_c)$
        $(P_{Ki}, P_{ATPi}, \boldsymbol{X}_{hi}, r_{1i}, r_{2i}, state\_i) \longleftarrow$ Walk$(P_{Ki}, P_{ATPi}, \boldsymbol{X}_{hi}, \boldsymbol{F}_i, r_{1i}, r_{2i}, state\_i)$
        $(\boldsymbol{F}_i,\ \boldsymbol{M}_i) \longleftarrow$ Force$(\boldsymbol{X}_{hi}, \boldsymbol{\theta}_{ci}, \boldsymbol{X}_c, \boldsymbol{\theta}_c)$
        $P_{ubi} \longleftarrow$ Unbind$(\boldsymbol{F}_i,\ \boldsymbol{M}_i, t_{ubi}, state\_i)$
        if $P_{ubi} \geq r_{ubi}$ then
          $(P_{Ki},\ P_{ATPi},\ P_{ubi},\ \boldsymbol{F}_i,\ \boldsymbol{M}_i,\ t_{ubi}, onMT\_i) \longleftarrow (1,\ 0,\ 0,\ \mathbf{0},\ \mathbf{0},\ 0,\ 0)$
          $r_{ubi} \longleftarrow Uniform(0, 1)$
        end if
      end if
      if $onMT\_i = 0$ then
        $t_{bi} \longleftarrow t_{bi} + 1$
        $(\boldsymbol{X}_{hi},\ P_{bi}) \longleftarrow$ Bind$(\boldsymbol{X}_c,\ \boldsymbol{\theta}_c,\ \boldsymbol{\theta}_{ki},\ t_{bi})$
        if $P_{bi} \geq r_{bi}$ then
          $(P_{bi},\ t_{bi},\ onMT\_i) \longleftarrow (0,\ 0,\ 1)$
          $(r_{1i},\ r_{2i},\ r_{bi}) \longleftarrow i.i.d\ Uniform(0, 1)$
        end if
      end if
    end for
  end for
Output: $(\boldsymbol{\theta}_c,\ \boldsymbol{X}_c,\ \boldsymbol{X}_{hi},\ \boldsymbol{F}_i)_t$, for $i = 1, 2, ..., N$ and $t = 1, 2, ..., N_t$.
```

Algorithm. 3.1: The stochastic multiple kinesin model. r_{1i}, r_{2i}, r_{bi}, r_{ubi} are independent and identically distributed ($i.\,i.\,d$) random variables. Function *Walk*() updates the chemical reaction states and the positions of kinesin heads. Function *Diffuse*() updates the cargo position. Function *Force*() calculates the force and moment exerted by a kinesin. Function *Bind*() and function *Unbind*() calculate the probabilities for a kinesin to bind to or unbind from a MT.

described by the model is no longer a Markov process. The transition between the states of the system is determined by the microscopic interactions between kinesins, cargo and MTs. Thus, the transition is spatial-temporal dependent as well as history dependent.

In the model, the dynamics of a kinesin i is characterized by six time-dependent variables, $\boldsymbol{X}_{hi}(t)$, $\boldsymbol{X}_{ki}(t)$, $P_{Ki}(t)$, $P_{ATPi}(t)$, $P_{bi}(t)$ and $P_{ubi}(t)$. $\boldsymbol{X}_{hi}(t)$ is a vector containing the position of the center of the two kinesin heads at time t. $\boldsymbol{X}_{ki}(t)$ is a vector containing the position where kinesin i attaches on the cargo surface. P_{Ki} and P_{ATPi} are the probabilities of staying at chemical reaction states [K+ATP] and [K.ATP]. $P_{bi}(t)$ is the binding probability. $P_{ubi}(t)$ is the unbinding probability. The Monte Carlo simulation described in Algorithm 3.1 is used to calculate the evolution of the system under pre-defined environmental conditions. Initially, the cargo is located at a position near the MTs, and all kinesins are unbound from the track. A time step Δt is chosen as 0.001 s for simulations. At each time step, five parts of the system are updated: 1) The translational and rotational motions of the cargo, characterized by ($\boldsymbol{X}_c$, $\boldsymbol{\theta}_c$), are updated based on the diffusion motion. $\boldsymbol{X}_c$ is a vector containing the position of cargo center. $\boldsymbol{\theta}_c = [\theta_x, \theta_y, \theta_z]$ is a vector containing the angular position of the cargo center. Where θ_x, θ_y and θ_z are angles with respect to the x, y and z axes. 2) Force $\boldsymbol{F}_i$ and moment $\boldsymbol{M}_i$ exerted on the cargo are calculated. 3) For each bound kinesin i, the chemical reaction, represented by the two probabilities P_{Ki} and P_{ATPi}, as well as the center position of two kinesin heads $\boldsymbol{X}_{hi}$ are updated. When the number of bound kinesins on the MT is n, the calculation of P_{Ki}, P_{ATPi} and $\boldsymbol{X}_{hi}$ are performed n times at every time step. 4) For each bound kinesin i, the unbinding probability P_{ubi} are calculated. The calculation of unbinding probabilities is performed n times at every time step. 5) For each unbound kinesin j, the binding probability P_{bj} are calculated. When there are N kinesins on the cargo and n of them bind to the MT, the calculation is performed $N - n$ times at each time step. It should

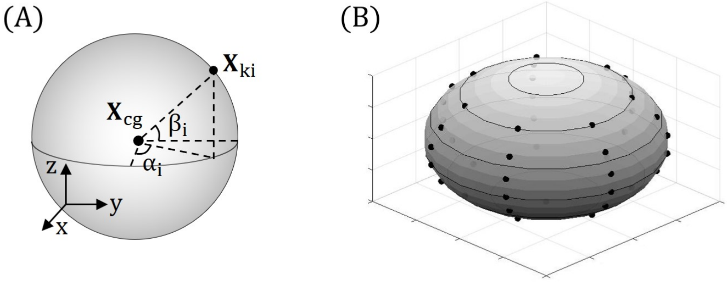

Figure. 3.2: **The distribution of kinesins on the surface of a cargo.** (A)Schematic illustration of the binding position $\boldsymbol{X}_{ki}$ of the cargo linker end of a kinesin i on the surface of the cargo. (B) An example of kinesin distribution when $N = 49$. The black dots represent the binding positions of kinesin cargo linkers and the cargo.

be noted that the six book-keeping variables, $\boldsymbol{X}_{hi}(t)$, $\boldsymbol{X}_{ki}(t)$, $P_{Ki}(t)$, $P_{ATPi}(t)$, $P_{bi}(t)$ and $P_{ubi}(t)$, are updated simultaneously at every time step. However, the kinesin dynamics including the transitions between chemical reaction state, unbinding and rebinding are characterized by $P_{Ki} \leq r_{1i}$, $P_{ATPi} + P_{Ki} \leq r_{2i}$, $P_{ubi} \geq r_{ubi}$ and $P_{bi} \geq r_{bi}$ respectively. These kinesin dynamics occur in a sequential manner in the model.

3.3.2 Distribution of kinesins on the cargo surface

N kinesins are assumed to be uniformly attached to the surface of the cargo. For a kinesin i, the binding position between its cargo linker end and cargo surface is denoted as $\boldsymbol{X}_{ki}$. $\boldsymbol{X}_{ki}$ is characterized by two angles α_i and β_i, as shown in Figure 3.2 (A). Specifically, $\alpha_i = 2\pi u$ and $\beta_i = cos^{-1}(2v - 1)$, where u and v are identical and independent random variables uniformly distributed between 0 and 1. Figure 3.2 (B) shows an example of 49 kinesins attached to the cargo surface.

Thus, the binding position $\boldsymbol{X}_{ki}$ can be calculated based on α_i, β_i and cargo center $\boldsymbol{X}_c$ as

$$\boldsymbol{X}_{ki} = \boldsymbol{X}_c + R\,[\sin\beta_i\cos\alpha_i,\ \sin\beta_i\sin\alpha_i,\ \cos\beta_i], \tag{3.1}$$

3.3.3 Kinesin walking motion

The basic dynamics for a kinesin i is described in Chapter II. Calculation of kinesin walking motion (function *Walk*()) is based on Algorithm 2.6. Calculation of the binding and unbinding probabilities of a kinesin (functions *Bind*() and *Unbind*()) is based on solving Equations 2.8 - 2.12.

3.3.4 Cargo diffusion

The transnational and rotational position of cargo center ($\boldsymbol{X}_c$ and $\boldsymbol{\theta}_c$) are influenced by the total force and moments generated by the bound kinesins as

$$\frac{d}{dt}\boldsymbol{\theta}_c = \frac{\sum_{i=1}^{n} \boldsymbol{M}_i}{8\pi\, R^3\, \delta} + \boldsymbol{r}(\sqrt{2D_r}), \tag{3.2}$$

$$\frac{d}{dt}\boldsymbol{X}_c = \frac{\sum_{i=1}^{n} \boldsymbol{F}_i}{6\pi\, R\, \delta} + \boldsymbol{r}(\sqrt{2D_t}). \tag{3.3}$$

where $\sum_{i=1}^{n} \boldsymbol{F}_i$ and $\sum_{i=1}^{n} \boldsymbol{M}_i$ are the total force and moment exerted on the cargo by n bound kinesins. The torque $\boldsymbol{M}_i$ is calculated as $\boldsymbol{M}_i = (\boldsymbol{X}_{ki} - \boldsymbol{X}_c) \times \boldsymbol{F}_i$.

3.4 Results

3.4.1 Model verification

The 3D dynamical model is verified based on previous experimental studies [7] of kinesins transporting polystyrene cargoes at a 90°intersection of two MTs [7]. In the experiments, first, 800 nm polystyrene cargoes were incubated with various concentrations of kinesins to allow different numbers of kinesins to attach to the surface of the cargo. After the binding between kinesins and cargoes reaches equilibrium, the medium was removed. Next, an optical trap was used to place the cargo near a single MT or an intersection of two MTs. The stall forces of the cargoes incubated with two different kinesin concentrations were measured using the optical trap.

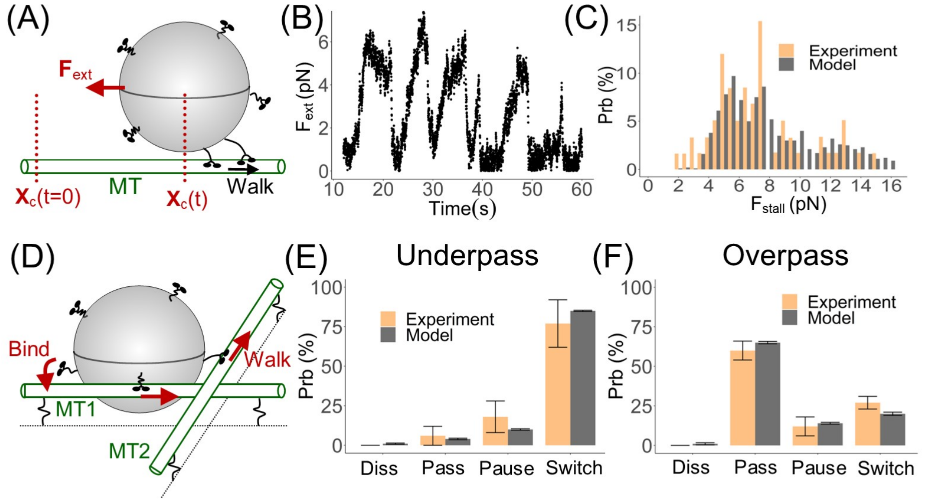

Figure. 3.3: **Verification of the stochastic multi-physics model.** (A) To calculated the stall force, the cargo is transported by kinesins on a single MT under an external load $\boldsymbol{F}_{ext}$. (B) The variation of the force F_{ext} on the cargo along the MT direction. (C) The distribution of the stall force F_{stall}. (D) Schematic illustration of the transport dynamics at a 90° MT intersection. (E) Probabilities for the cargo to pass, pause, switch or dissociate at the intersection when it is moved on the bottom MT (MT1) to the intersection (i.e., underpass). (F) Probabilities of the cargo dynamics when it is transported on the top MT (MT2) to the intersection (i.e., overpass). The experimental data is from the previous study [7].

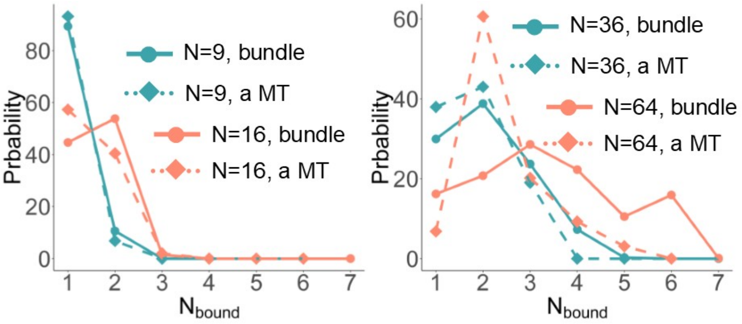

Figure. 3.4: **The distribution of the number of kinesins that bind on a single MT or a parallel MT bundle N_{bound} over the different number of kinesins on the cargo N.**

When the concentration of kinesin is 0.001 μg/ml, it is estimated that only one kinesin is attached to a cargo. The measured stall force distribution follows a normal distribution with mean value of 4.2 pN. More than two kinesins are expected to be attached to the cargo when the kinesin concentration in the medium is 0.02 μg/ml. However, the exact number of kinesins was not determined in the experiment [7]. To acquire the approximate number of kinesins at a concentration of 0.02 μg/ml, the distributions of stall force of a 800 nm cargo are calculated using the model for different numbers of kinesins and compared with experimental measurements [7]. In the calculation, an external force $\boldsymbol{F}_{ext}$ parallel to the MT but opposite to the kinesin walking direction is applied to the cargo. To simulate the behavior of the cargo under the optical trap, the external force is assumed to be proportional to the moving distance of the cargo. Specifically, the magnitude of the external force is calculated as $F_{ext} = k_{eff}[X_c(t) - X_c(t = 0)]$, where the effective stiffness k_{eff} is 0.07 pN/nm, similar to the experimental setup [113]. X_c is the cargo displacement along the MT direction (Figure 3.3 (A)).

Figure 3.3 (B) shows the variation of F_{ext} calculated using the model. F_{ext} increases as the cargo moves away from the starting point. When the cargo is stalled, F_{ext} stops increasing and slightly fluctuates around the maximum value. After a few seconds, all kinesins unbind from the MT and the cargo returns to the starting point. Then, F_{ext} decreases to 0 pN accordingly. Afterwards, cargo diffuses around the starting point until one or more kinesins bind to the MT and the active transport starts again. It is assumed the cargo is stalled when the variation of F_{ext} is less than 2 pN within 2 s. F_{stall} is calculated as the average of F_{ext} during this 2 s time interval. When 36 kinesins are attached to the cargo surface, the stall force distribution calculated using the model shows a good agreement with the distribution measured in the experiments [7] when the kinesin concentration is 0.02 μg/ml (Figure 3.3 (C)).

When the cargo is placed next to a single MT and the number of kinesins N is 36, one or two kinesins are walking on the MT most of the time (Figure 3.4). The stall force of one engaged kinesin follows a Gaussian distribution with a mean value of 4.2 pN. The stall force of two engaged kinesins would be a Gaussian distribution of mean 8.4 pN if the load on the cargo were equally distributed among kinesins. Thus, the distribution of the stall force when $N = 36$ would have two peaks at 4.2 and 8.4 pN. However, both the experiments [7] and simulations show that the two peaks in the distribution of the stall force are not exactly 4.2 pN and 8.4 pN. Particularly, the first peak is larger than 4.2 pN and the second peak is smaller than 8.4 pN. These results suggest that the transient binding and unbinding of kinesins and the non-uniform distribution of forces among the engaged kinesins has a smoothing effect on the probability distribution of the stall force. The stall force is likely to have values between the stall forces of a single kinesin and two kinesins. In addition, a stall force larger than 8.4 pN is frequently observed, as shown in Figure 2 (C).

Next, the cargo is placed near a 90° intersection of two MTs, and the transport direction and time are calculated. Similar to the experimental setup [7], the bottom MT is attached to a glass slide by proteins with an approximate length of 135 nm (Figure 3 (D)).In the underpass situation, at the beginning, the cargo is placed at a random place 1 μm away from the surface of MT2 and 400 nm away from the surface of MT1. No kinesin binds to the MTs. At every time step, the cargo diffuses and the binding probabilities of all kinesins are calculated. When at least one kinesin binds to MT1, the cargo is transported toward the MT intersection. The simulation finishes when the cargo moves 1 μm away from the intersection or the simulation time exceeds 8 s. In the overpass situation, the cargo is placed at a random place 1 μm from the surface of MT1 and 400 nm from the surface of MT2. The cargo motions are classified into four different types based on the following criteria. If the cargo moves 1 μm away from the intersection on the original MT in 3 s, then the motion is defined as passing. If the cargo switches to the intersecting MT, and moves 1 μm away from the intersection in 3 s, the motion is defined as switching. If the cargo remains at the intersection longer than 3 s, the motion is defined as pausing. If the cargo diffuses away from two MTs and does not rebind in 3 s, the motion is defined as dissociation. To verify the model, the probability distribution of the four types of cargo motions is calculated when $N = 36$ and compared with experiments [7]. Note that, to calibrate the variation in probabilities influenced by the number of simulations, one thousand simulations are performed. The results are devided into 10 groups to acquire the error bars shown in Figure 3.3 (E) and (F). In the underpass situation, the top MT impedes the cargo from moving forward on the original MT and increases the switching probability (Figure 3.3 (E)). In the overpass situation, the cargo can be transported above the two MTs and can pass the intersection. Overall, the modeling results show good agreement to the experiments [7]. In addition, the dwell time that a cargo spends at the MT intersection is calibrated (Figure 3.5). In the underpass situation, the mean dwell time at the intersection is 4.7 s. In the overpass situation, the mean dwell time at the intersection is 4.8 s. If the cargo is transported along the MT between two intersections, the time for the cargo to move 2 μm is around 3.3 s (assuming the velocity is 600 nm/s). Thus, the intersection slows down the transport.

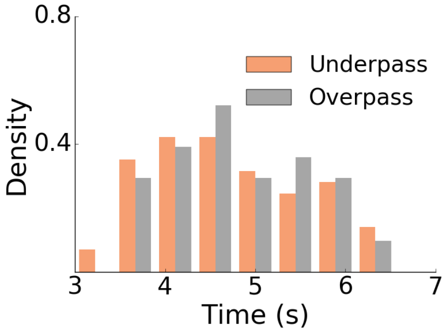

Figure. 3.5: **The distribution of the dwell time T_d at the intersection.** T_d is calculated as $T_d = T_e - T_b$, where T_b is the time when the cargo starts to move from a position located 1 μm away from the intersection, T_e is the time when the cargo passes the intersection and moves 1 μm away from the intersection.

3.4.2 Influence of MT topology

Based on the model, the effects of the topology of a MT intersection on the transport dynamics are studied. As shown in Figure 3.6 (A) and (D), the intersection topology can be characterized by the distance H and angle β. H is defined as the shortest distance between the surfaces of two MTs. The intersection distance H is varied from 0 nm to 1000 nm. When $H > 1000$ nm, the intersected MT has negligible effects on the transport. β is defined as the angle between the two MTs. β varies between 0° and 180°. The number of kinesins on the cargo is 36.

In the overpass situation (Figure 3.6 (B) and (E)), the cargo motion is less influenced by the bottom MT. Cargo is likely to move above the two MTs, and the kinesins is not long enough to bind to the bottom MT. Therefore, the probability of passing is large and less influenced by the intersection topology.

In the underpass situation (Figure 3.6 (C) and (F)), the transport of a cargo by multiple kinesins are less influenced by the intersection distance H compared to the transport by a single kinesin. However, a decrease in the switching probability is still noticeable as H increases. When $H \leq 200\,nm$, the decrease is caused by the geometrical barrier of the intersection. Cargo rotates at the intersection due to

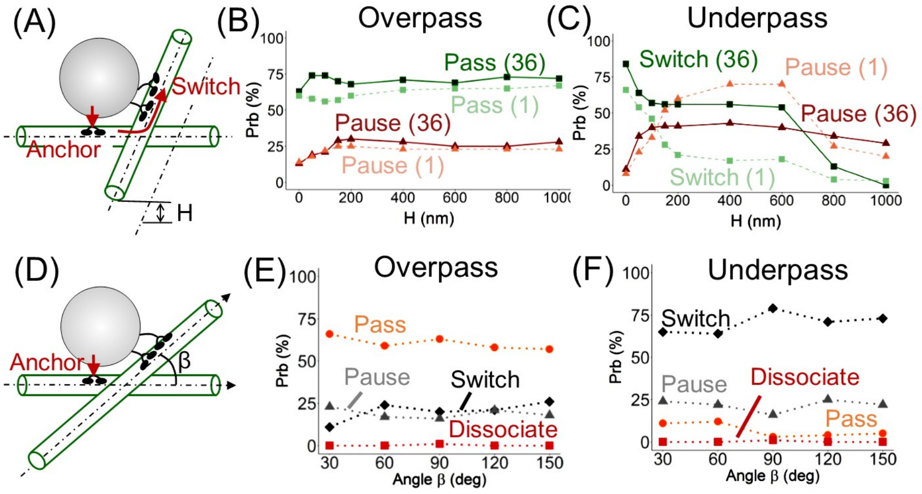

Figure. 3.6: **Transport dynamics at the intersection of two MTs is influenced by the intersection distance H and the angle β.** (A) The schematic illustration of the intersection distance H. (B) The influence of H on the passing and pausing probabilities in the overpass situation when 1 or 36 kinesins are attached on the cargo. (C) The influence of H on the switching and pausing probabilities in the underpass situation. Increasing the intersection distance significantly disrupts the transport in the underpass situation. Multiple kinesins on the cargo (36 kinesins in the case) reduces the impairment of H on the transport. (D) A schematic illustration of the intersection angle β when two MTs are attached to each other. (E) and (F) Transport dynamics influenced by the angle β in the overpass and underpass situations.

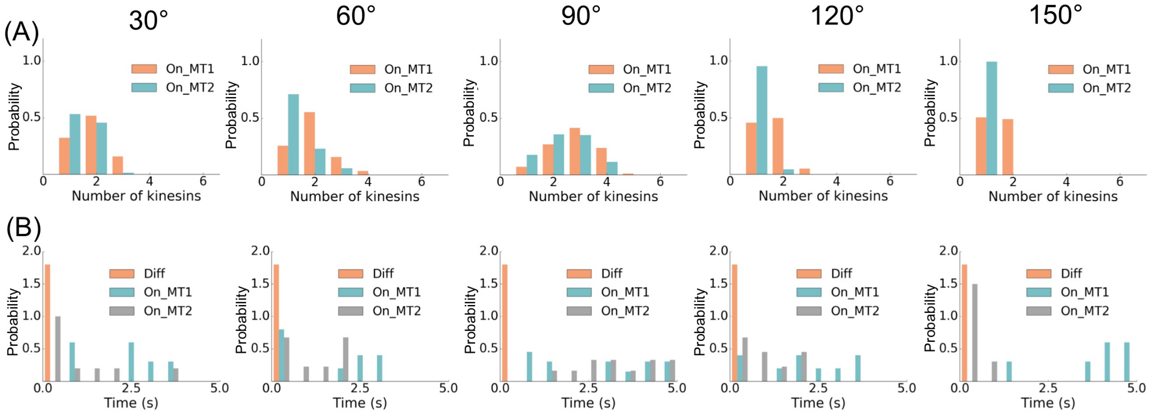

Figure. 3.7: **The influence of intersection angle β on the transport dynamics in the underpass situation.** (A) The distribution of the number of kinesins on MT1 and MT2 at the intersection when N is 36. (B) The distribution of the association time on the two MTs as well as the diffusion time. The association time on a MT is defined as the time interval when at least one kinesin binds to that MT.

the moment generated by kinesins. When $H \geq 800\,nm$, the switching probability decreases because cargo can pass the intersection through the gap between the two MTs. The model also predicts that the switching probability is maximized when the two MTs are perpendicularly attached. When $\beta = 90^\circ$, the average number of kinesins on MT2 and the time duration when at least one kinesin binds to MT2 are the largest (Figure 3.7). Therefore, the switching probability is enhanced because more kinesins pull the cargo along the intersecting MT for a longer time. When $\beta > 90^\circ$, the antagonistic dynamics between kinesins on two MTs accelerates their unbinding probabilities. Note that, when the intersection distance $H > 0\,nm$, the influence of the intersection angle β on transport dynamics can be different. For example, Bergman et al. [31] showed that the switching probability is the largest when $\beta = 90^\circ$ and $H = 0\,nm$. However, when H is equal to the cargo radius or diameter, the switching probability is small at the 90° intersection. In addition, the latest work from Higuchi et al. [114, 115] observed frequent direction changes in very acute or obtuse angles inside MT networks in living cells. Thus, these results

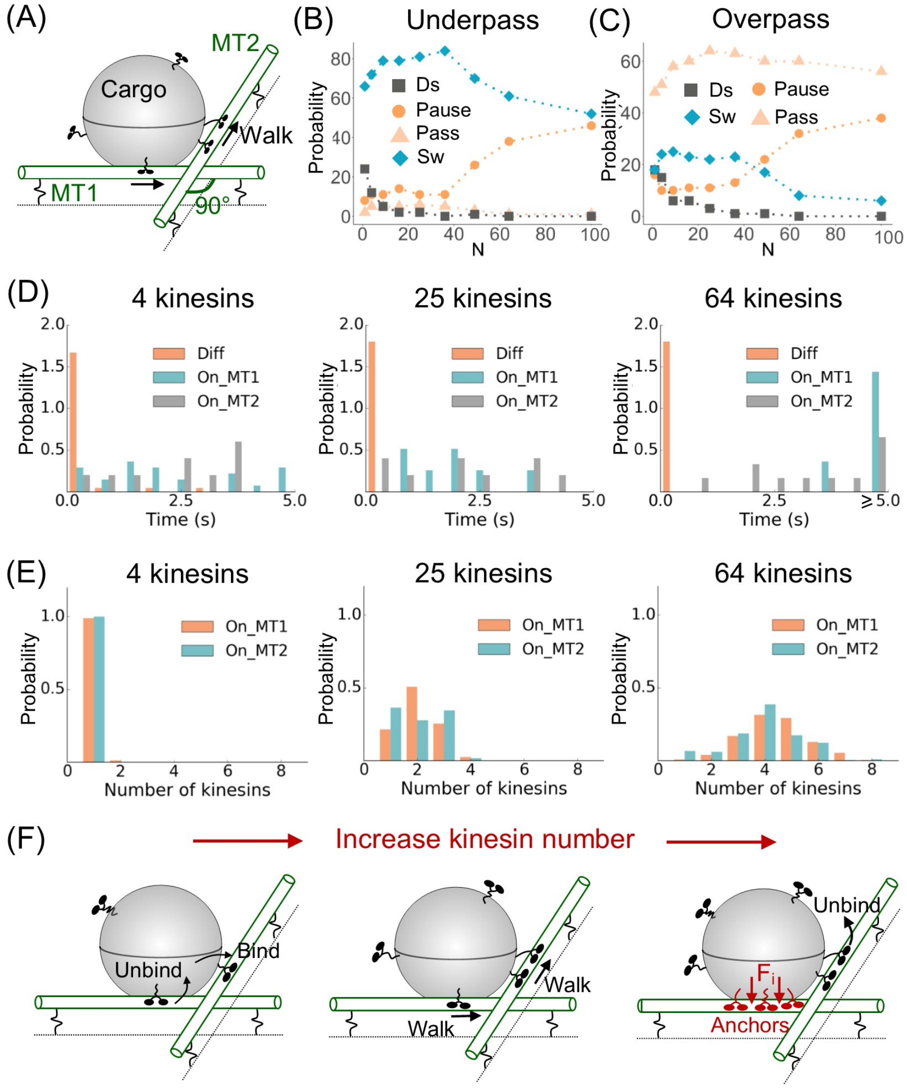

Figure. 3.8: **collective transport dynamics influenced by the number of kinesins N at a 90° MT intersection.** (A) The schematic view of a cargo being transported along the bottom MT and switching to the top MT at the intersection.The intersection distance is 0 nm. (B and C) The influence of the number of kinesins N on the transport dynamics when the cargo is transported along the bottom MT (B) or the top MT (C) toward the intersection. (D) In the underpass situation, the distribution of the association time on MT1 and MT2 as well as the diffusion time when N is 4, 25 and 64. (E) In the underpass situations, the distribution of the number of associated kinesins on MT1 and MT2 over different N. (F) The schematic illustration of the influence of kinesin number N on the transport dynamics.

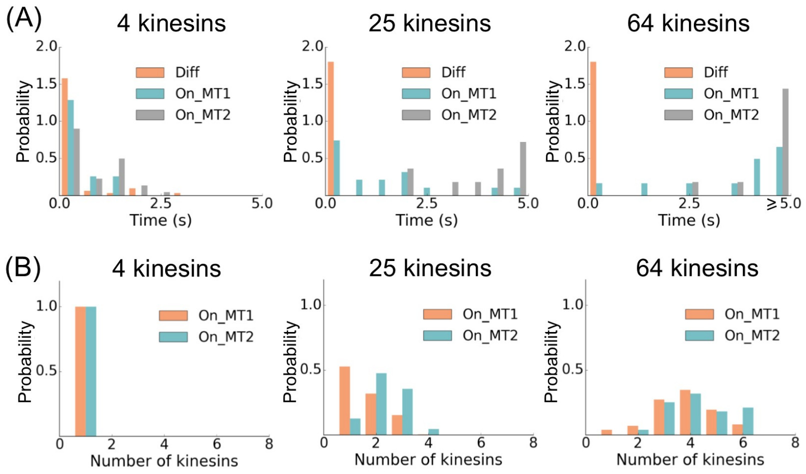

Figure. 3.9: **The collective transport dynamics influenced by the number of kinesins N in the overpass situation.** (A) The distribution of the association time on MT1 and MT2 as well as the diffusion time when N is 4, 25 and 64. (B) The distribution of the number of associated kinesins on MT1 and MT2 over different N. The intersection distance is 0 nm and the intersection angle is 90°.

indicate that the distances between intersected MTs in vivo are likely to be larger than 0 nm and comparable to the radius of intracellular cargoes. Bálint et al. [68] measured the intersection distances inside monkey kidney cells and showed that the intersection distances vary from 100 nm to 600 nm. Therefore, our model predictions are consistent with previous findings.

3.4.3 Influence of kinesin number

To understand the effects of the number kinesins (usually quantified by the kinesin concentration in experiments) on the intracellular cargo transport in different MT topologies, multiple analyses are performed. First, when the cargo is transported toward a 90° intersection of two MTs, the probabilities of an 800 nm-cargo passing, pausing, switching and dissociating at the intersection are calculated over different number of kinesins N. In the underpass situation, when $N < 16$, only one kinesin is likely to bind to the MTs (Figure 3.8 (E)). Thus, the cargo dissociation probability is large. When $N \in [16, 36]$, the cargo has the largest switching probability, because

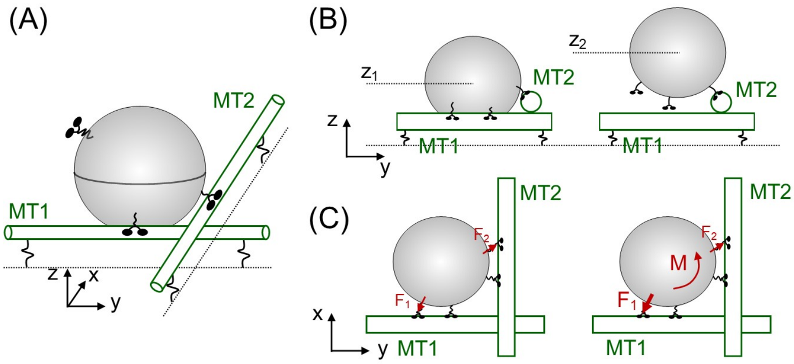

Figure. 3.10: **Schematic illustration of the influence of cargo levitation and torque diffusion on the proportion distribution of motors on different MTs.** (A) Kinesins transport the cargo from MT1 toward the intersection. (B) Cargo levitation increases the proportion of kinesins on MT2 by changing the distances between the cargo and MTs. (C) A counterclockwise torque changes forces inside the kinesins and increases the proportion of kinesins on MT2.

some kinesins bind to MT1 to prevent cargo dissociation and more kinesins start to bind to MT2 to switch transport direction. A longer average association time on MT2 than on MT1 ensures cargo moving away from the intersection (Figure 3.8 (D)). When $N > 36$, the number of kinesins that bind to the original track increases considerably. When $N = 64$, the average number of kinesins bind to MT1 is around 4.4. Since unbinding 4 kinesins simultaneously requires a large force, the cargo is likely to be trapped near MT1. Similarly, in the overpass situation, when an intermediate number of kinesins are attached to the cargo ($N = 25$), multiple kinesins bind to MT2 for a sufficient long time, which leads to the large passing probability (Figure 3.9). Note that, the proportion distribution of kinesins on different MTs at the intersection depends on the cargo levitation and the external torque (Figure 3.10). For example, when the cargo is levitated above, a larger proportion of kinesins are going to bind to MT2 because of the limited length of the cargo linkers. When a counter clockwise torque is applied to the cargo, the forces between kinesins and MT1 increase, which accelerates the unbinding from MT1 and modifies the proportion distribution of kinesins.

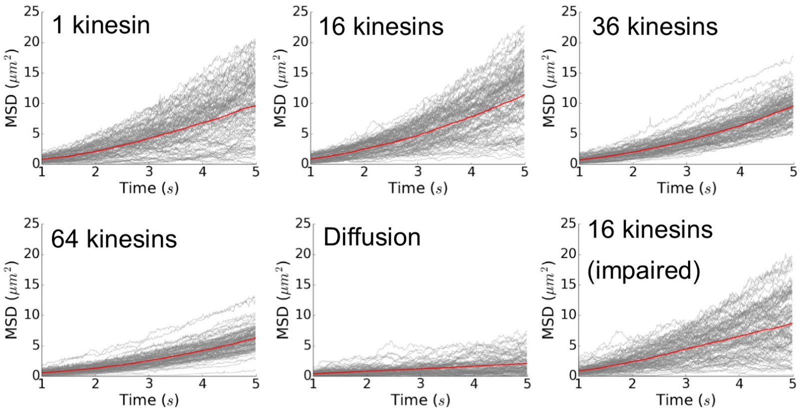

Figure. 3.11: **The realization of 100 simulation results of the MSDs along a parallel MT bundle over different kinesin number N.** The grey lines are the MSDs over time calculated in each of the 100 simulations. Red lines are the ensemble average of the 100 MSD curves.

Next, the transport dynamics on a bundle of two parallel MTs is studied. The distance between the surfaces of the two parallel MTs is set to be 15 nm in this study. Compared to a single MT, a parallel bundle has more binding sites reachable to kinesins. Thus, when $N \geq 36$, the average number of kinesins on the bundle is larger than on a single MT (Figure 3.4). In the simulation, the cargo position $\boldsymbol{X}_c$ over time t is recorded. Then, the mean square displacement (MSD) of the cargo, calculated as $\mathrm{MSD}(t) = \frac{1}{100}\sum_{i=0}^{100}\left[\boldsymbol{X}_{ci}(t) - \boldsymbol{X}_{ci}(t = 0)\right]^2$ is used to represent the cargo motility. $\boldsymbol{X}_{ci}$ is the position of the cargo at time t in i^{th} simulation. We found that the average MSD is the largest when $N = 16$. When $N = 1$, the variation of the MSD curves is large because the only one kinesin connecting between the cargo and the bundle is likely to unbind and the transport is disrupted accordingly. Increasing the kinesin number N reduces the variation, which suggests the transport becomes more robust. However, when $N \geq 36$, the slopes of all MSD curves are low, indicating transport becomes slower. In addition, when the cargo is transported by impaired kinesins which have a larger unbinding probability (i.e. twice of its original value) and smaller binding probability (i.e. half of its original values), the 100 realizations of MSDs become close to the situation when $N = 1$ (Figure 3.11). To understand

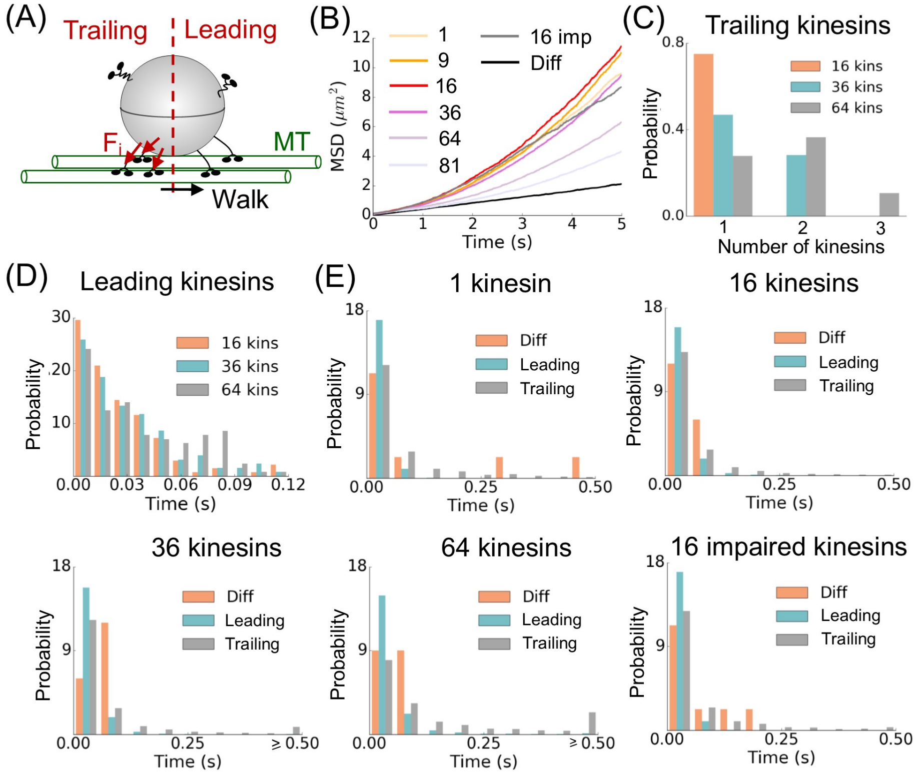

Figure. 3.12: **The collective transport dynamics influenced by kinesin number N along a parallel MT bundle.** (A) The schematic illustration of the kinesins binding between the cargo and the MTs. Kinesins are classified as trailing kinesins and leading kinesins based on whether the positions of their heads locate behind the center of the cargo. (B) The MSDs of the cargo over different number of kinesins N. The motion of the cargo is superdiffusive because of the active forces applied by kinesins. In addition, the grey line represents the MSD of the cargo transported by 16 impaired kinesins. The impairment of the kinesin is defined as decreasing the binding rate k_{b0} to half of its original value and increasing the unbinding rate P_{u0} and k_{u0} to twice of the original values. (C) The distribution of the number of trailing kinesins when N is 16, 36 and 64. (D) The distribution of the duration of a chemical reaction cycle for the leading kinesins over N. (E) The distribution of the association time of the trailing and leading kinesins on the MTs and the diffusion time over N.

(A) Independent

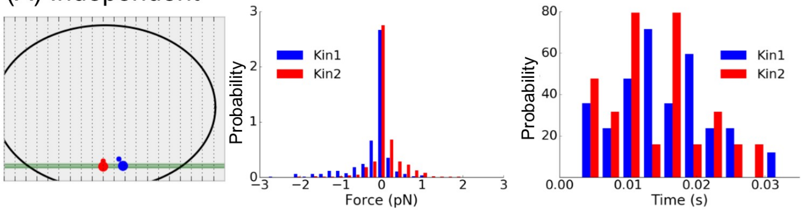

(B) Antagonistic

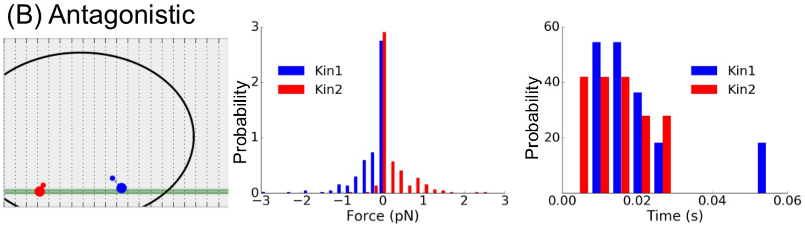

(C) Synergistic

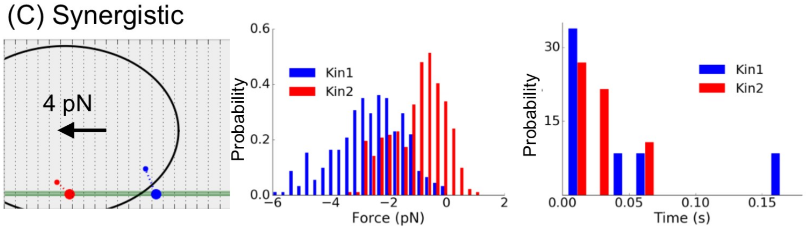

Figure. 3.13: **Three types of collective kinesin dynamics (of two kinesins) along a single MT.** (A) Independent dynamics happens when two identical kinesins walk with similar stepping rate and pull the cargo. (B) Antagonistic dynamics is caused by the two kinesins pull the cargo toward different directions. The leading kinesin experiences a resisting force and the chemical reaction on its heads is likely to be slowed down. (C) Synergistic dynamics helps two kinesins transport the cargo under an external load. The leading kinesin shares a larger load and its chemical reaction happens slower than the trailing kinesins. The first column of the plots contains the schematic representations of the cargo (black circle), MT (green line) and two kinesins. The leading kinesin (kinesin 1) is represented as blue. The trailing kinesin (kinesin 2) is represented as red. The second column of plots represent the distribution of forces inside the two kinesins. Positive values represent the direction of the force is the same as the walking direction. The third column of plots are the distributions of the time a kinesin takes to complete a chemical reaction cycle and walk one step forward.

the mechanism that leads to the decreasing of the transport velocity when N is large, the distribution of the duration of a chemical cycle of leading kinesins, the number of trailing kinesins, and the association time of the trailing and leading kinesins are calculated. Note that, a trailing kinesin is defined as a kinesin whose heads attach to the binding sites behind the center of the cargo along the MT direction. A leading kinesin has heads attaching to positions ahead of the cargo center (Figure 3.12 (A)). Trailing kinesins pull the cargo back and apply resisting force on the leading kinesins. The resisting force slows down the stepping frequency of the leading kinesins (Figure 3.13 (B)). On the MT bundle, as N increases, more kinesins bind behind the cargo center (Figure 3.12 (C)). A large number of trailing kinesins causes the long duration of a chemical reaction on the leading kinesin heads (Figure 3.12 (D)). At the same time, a large N reduces the diffusion time and increases the association time on both MTs. However, the increasing of the association time for the trailing motors is faster than the leading motors. When $N \geq 36$, some trailing motors remain binding to the MT for more than 5 s. Thus, the transport speed and cargo mobility are reduced at the high kinesin concentration.

The interference of a neighboring MT on the transport is considered in order to study the robustness of the transport along a MT bundle for different numbers of kinesins. In the model, the neighboring MT is placed perpendicularly to the bundle consisting of two parallel MTs, and the distance between the surfaces of the intersecting MT and the bundle is chosen to be 850 nm so cargo can move through the gap between the two parallel MTs and the neighboring MT, as shown in Figure 3.14 (A). Initially, the cargo is transported on the MT bundle towards the neighboring MT. When the cargo fails to move 1 μm away from the neighboring track in 3 s, or when the cargo switches moving direction, or when it dissociates from the MT, the transport is defined as disrupted. Based on the model, the probability of passing the neighboring MT without being disrupted is calculated over the number of kinesins N

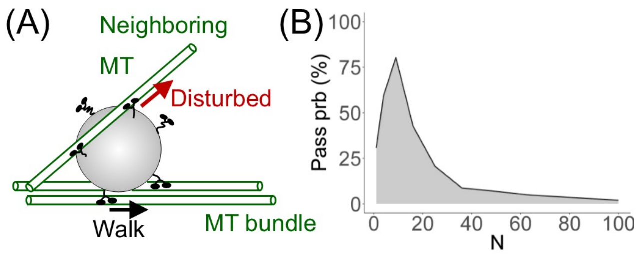

Figure. 3.14: **The interruption of a neighboring MT on the transport for various number of kinesins N.** (A) An illustration of the situation when a cargo is transported by kinesins along two parallel MTs. Extra kinsesins on the cargo can bind to the neighboring track and disrupt the transport. The neighboring track is placed perpendicularly to the two parallel MTs. The shortest distance between the surfaces of the neighboring MT and the two parallel MTs is 850 nm. (B) The probability of passing the neighboring MT without being disrupted over different value of N.

(Figure 3.14 (B)). When $N = 16$, the largest passing probability is achieved. When $N > 16$, some kinesins are expected to bind to the intersecting MT and disturb the transport. When $N \leq 9$, the interference between the cargo and the intersecting MT increases the dissociation probability.

3.5 Conclusion and future outlook

This paper proposed a 3D stochastic multi-physics model to study the collective cargo transport by multiple kinesins in different topologies of MTs. Based on the model, three important biological insights are observed.

First, when two identical kinesins pull a common cargo together along a track, the external load applied on the cargo is not equally distributed among all kinesins such that the contribution of each kinesin to the cargo transport is different. When two kinesins are attached to adjacent positions on the surface of the cargo, the forces inside the two kinesins are small and almost symmetrically distributed about 0 pN. The distribution of the predicted time duration of a chemical reaction cycle is shown in Figure 3.13 (A). The estimated average time duration calculated is 0.015 s. Since kinesin moves 8 nm in each step, the average velocity of the two kinesins is around 533 nm/s. The predicted average time duration of the two kinesins is similar to the experimentally measured value of a single kinesin walks along a MT [116, 5]. Thus, the two kinesins transport the cargo independently. When the two kinesins are attached to distant positions on the surface of the cargo, the average forces in the two kinesins increase. The trailing kinesin experiences an assisting force while the leading kinesin experiences a resisting force (Figure 3.13 (B)). Under an external load opposite to the transport direction, cargo diffuses back. The leading kinesin extends longer than the trailing kinesin and shares a larger force. Therefore, the time duration of the chemical reaction on the leading kinesin heads is significantly increased (Figure 3.13 (C)). The leading kinesin is likely to be stalled and the trailing kinesin keeps walking. Our analysis provides a plausible explanation to the experiments, in which Jamison et al. [74] measured the force velocity curve of two kinesins separated by a DNA-based molecular scaffold with fixed length. They found that the measured force velocity curve of two kinesins is different from the theoretically generated curve assuming each motor shares half of the applied load and two motors do not interact. Specifically, the measured walking velocity of two kinesins is slower than the theoretically predicted values at low loads because of the antagonistic dynamics, and the velocity is faster at large loads because of the synergistic dynamics. Interestingly, Uar et al. showed [117] that two identical dyneins tend to share load equally in both steady state and during the initial building up of internal elastic strains. It is likely the properties of two motors, such as the length, stiffness, binding rate and unbinding rate, play important roles in motor cooperativity. For example, Uar et al. [117] observed that the average force generated by several strong motors with larger stall force and large unbinding rate, such as kinesin-1, deviate strongly from their collective stall force. It suggests that strong motors tend to have a worse cooperativity, probability because motors detach from the track during strain generation. Wang et al. [118] showed that the degree of cooperativity of two kinesin motors is influenced by the stiffness of the cargo linker, unbinding rate, and stepping rate. In particular, a smaller unbinding rate, a lower cargo linker stiffness and a larger stepping rate lead to a higher motor cooperativity and a longer run length. Arpa et al. [75] found that the cotransport by slow kinesin-1 and fast kinesin-3 is likely to be dominated by kinesin-1, because the leading kinesin-3 can rapidly unbind and re-equilibrate their positions near the cargo whereas the trailing kinesin-1 continue to pull. In our study, it is shown that the influence of the cotransport is originated from the different extensions of the kinesin cargo linkers. Therefore, when the length of the cargo linker of the leading kinesin is longer than the trailing kinesin, the transport is expected to be more robust to external loads. To confirm this behavior, additional experiments on the run lengths and velocities of the cargo mediated by motors with different lengths are needed. Second, trailing kinesins could impair the cargo transport. Ross et al. [7] measured the probabilities of passing, switching, pausing and dissociation at the 90° MT intersection over different kinesin concentrations. They found that the pausing probability increases, and the switching probability decreases at high kinesin concentration. Based on the model, we show that the changes in the switching and pausing probabilities over kinesin concentrations are caused by the fact that several trailing kinesins bind to the original MT and act as anchors to prevent cargo being transported away from the intersection. When multiple kinesins walk on the parallel MT bundle toward the same direction, we found that the cargo mobility is reduced when too many kinesins are involved. This phenomenon is reminiscent to the negative correlation between the transport velocity and motor concentration observed in previous experiments [102, 119, 105]. Specifically, Shubeita et al. [102] found that the average transport velocity of the lipid droplets in the embryos with reduced kinesin concentration was approximately 5.5% higher than in wild-type embryos. Telley et al. [119] measured the concentration dependence of motor characteristics, including the run length, dwell time, velocity and binding rate. The slow transport at high motor concentration is usually explained as the binding sites on the MT being fully occupied by the abundant motors such that the unbinding rates of kinesins is increased and binding rates are decreased. In this work, we have shown that the excessive trailing motors could also reduce the transport via the mechanical interactions between motors. In general, the pausing phenomenon during the transport generated by excessive trailing motors could be one of the major causes of the subdiffusive cargo motor inside the cells [120, 121]. Zaburdaev et al. [122] mathematically showed that by varying the power law tails of the distribution of the pausing time, all the diffusion regimes (i.e. normal diffusion, superdiffusion and subdiffusion) can be accessed. However, whether and at what motor concentration the active transport will be overwhelmed by the increased pausing time in different topology of MTs needs to be studied further. Third, the microscopic dynamics of kinesins depends on geometrical information, including the distribution of kinesins on the cargo, the relative position of the cargo on the MTs, and the topology of MTs. Therefore, changing the geometrical information will lead to changes in the microscopic kinesin dynamics. However, as an average outcome of these microscopic dynamics, the macroscopic properties of the transport (i.e., the ability to persist in the transport direction and move fast) show surprising similarities in different MT topologies. Specifically, we predict that there is an optimal number of kinesins to transport a cargo pass MT intersections and along MT bundles.

The 3D stochastic dynamic model proposed here can be extended to characterize more complex and *in vivo*-like situations. For example, the low stiffness of the intracellular cargoes can influence the collective dynamics of kinesins. Due to the compliance of the soft cargo, more kinesins can bind to the MT, but the mechanical coupling among kinesins becomes weaker. In vitro methods, including the DNA scaffolds and modifying the anchor point of motors on the cargo surface [89, 123] have been used to study different mechanical couplings of kinesin motors. Combining our model with these in vitro experiments, general transport dynamics influenced by the coupling stiffness and the distance between kinesins can be investigated. Moreover, it would be also interesting to study whether the selective transport of different types of intracellular cargoes to their own destinations is determined by the cargo stiffness, and whether the failure of intracellular transport under disease conditions is influenced by changes in cargo stiffness.

CHAPTER IV

Anomalous Particle Diffusion

4.1 Abstract

We provide a generalized persistent random walk (GPRW) model to describe the anomalous diffusion-like dynamics influenced by particle velocity and directional persistence. We showed that the GPRW model can be simplified as a Fokker Planck-like equation when the magnitude of velocity is constant and the persistent time is exponentially distributed. At long time scale, the particle motion is diffusion with directional drifting. When the velocity is correlated with persistent time, particle performs Fickian diffusion, but its full distribution diverges from Gaussian. In addition, when the persistent time follows a non-exponential distribution, particle motion is super-diffusive.

4.2 Introduction

Many anomalous diffusion and transport phenomena other than Gaussian and Fickian diffusion have been observed in complex systems, such as particles in turbulent flows, intracellular protein diffusion, bacteria and animal migration and spreading of epidemics [124, 125, 126, 127, 8]. To describe the microscopic dynamics of particles and the macroscopic diffusion and transport process, there are two key complimentary approaches in statistical physics. The first approach is based on the concept of (continuous-time) random walks and partial differential equations (diffusion equations), and the second is based on stochastic differential equations (Langevin approach). The random walk based approach has strength in the flexibility of model construction and explicit physical meanings of model variables and parameters. It has been widely applied to study and understand the real-world observations.

In the random walk based approach, the most well-known one is the diffusion equation derived based on heat conduction by Fourier for more than a century [128]. The diffusion equation describes Gaussian and Fickian motion of the particle where its mean square displacement (MSD, denoted as $\langle \boldsymbol{x}^2 \rangle$) is linear in time, $\langle \boldsymbol{x}^2 \rangle = 4Dt$, where D is referred to as diffusion coefficient. The MSD $\langle \boldsymbol{x}^2 \rangle$ can be either ensemble average over n particles, $\langle \boldsymbol{x}^2 \rangle_n = \dfrac{1}{n} \sum_{i=1}^{n} |\boldsymbol{x}_i(t) - \boldsymbol{x}_i(0)|^2$ or time average, $\langle \boldsymbol{x}^2 \rangle_t = \dfrac{1}{t} \int_0^t |\boldsymbol{x}(t') - \boldsymbol{x}(0)|^2 dt'$. In Gaussian and Fickian diffusion, $\langle \boldsymbol{x}^2 \rangle_n = \langle \boldsymbol{x}^2 \rangle_t$. However, a non-physical drawback of the diffusion equation is the possibility of having infinite particle speed. At the same time, experiments show that the MSDs can be nonlinear in time. Specifically, $\langle \boldsymbol{x}^2 \rangle = 4D_\alpha t^\alpha$. When $\alpha < 1$, the particle motion is named as subdiffusion. When $1 < \alpha < 2$, particle performs superdiffusion. To consider the finite speed of the moving particle, the persistent random walk (PRW) model is proposed. The basic schematization of the PRW model can be described as: " a particle starts from a point 0 and moves with a constant speed v in a straight line for time t_1; it then turns through an angle θ and moves in a second straight line for time t_2. In two dimensional (2D) case, θ is uniformly distributed between 0 and 2π. The particle repeats this process n times. Thus, the PRW model describes the probability that after these n stretches the particle is at a distance between r and $r + dr$ from its starting point 0." When the moving time is a constant ($t_i = t_j$, $\forall\, i, j \in [1, n]$), the PRW model can be simplified into the telegraph equation, which captures the transient ballistic motion at short times and Gaussian Fickian diffusion at long times [129]. When the particle moves under random external forces (i.e. particle has random walking time) and one disregards the random effects occurs in the order of γ^{-1} (i.e. walking time follows exponential distribution with parameter γ), the PRW model is simplified into a Fokker Planck equation [130]. When the walking time follows a long tailed distribution, the particle motion is superdiffusive. To consider the subdiffusive dynamics where particles spread slower than Fickian diffusion, a long-tailed distributed waiting time between two consecutive random walks is taken into account. Fractional telegraph equation and fractional Fokker Planck equation can further be derived from PRW model for the superdiffusive and subdiffusive motions [131, 132]. Furthermore, several other researches modified the framework of PRW model and consider the different distributions of particle speed [133, 134, 122], such as the random walks with random velocities (RWRV) model [133]. While most works focus on the particle moving time and speed, the effects of directional heterogeneity (specifically, the probability of a particle moving in a specific direction θ) on diffusion and transport dynamics is largely unknown.

In this work, we proposed a generalized persistent random walk (GPRW) model to study three different situations where the switching of particle moving direction is non-uniform in θ and correlated with particle speed and moving history. In the first situation, the directional switching probability is non-uniformly distributed over θ and spatially dependent. We showed that the particle probability density in phase space is determined by the spatial and angular particle flux. At long times, particles maintain Fickian diffusion with directional drifting influenced by angular heterogeneity. In the second situation when the probability of maintaining the same walking direction is reinforced by the particle speed (i.e. particle directional persistence is positively correlated with speed), particle performs Fickian diffusion with a significantly improved diffusion coefficient and its distribution diverges from Gaussian. In the third situation, we showed that the motion of the particle is superdiffusive when the probability of maintaining the walking direction is reinforced by the distances the particle has already traveled.

4.3 Model

The particle motion is simplified as a series of connected line segments as in the PRW model [135, 136]. Each line segment is named as a sojourn. For example, in Figure 4.1 a, from $(\boldsymbol{x}', t')$ to $(\boldsymbol{x}, t)$ is a sojourn. The particle velocity during a sojourn is assumed to be invariant, and it can be represented by its magnitude and direction, represented as $\boldsymbol{u} = f(U, \theta)$. Where U is the magnitude and θ is the direction. The time interval of a sojourn is referred to as persistence (or persistent time), denoted as t_p. For example, $t - t'$ is the persistence of a sojourn from $(\boldsymbol{x}', t')$ to $(\boldsymbol{x}, t)$. The distribution of t_p is $\phi(t_p)$, and the cumulative distribution is $\Phi(t_p) = \int_{t_p}^{\infty} \phi(t)dt$. At the end of a sojourn (e.g. $(\boldsymbol{x}, t)$), particle changes moving velocity. The probability of switching from velocity $\boldsymbol{u}'$ to $\boldsymbol{u}$ is denoted as $r(\boldsymbol{u};\, \boldsymbol{u}', \chi)$, where χ represents factors that influence the switching of particle direction. For example, $r(\boldsymbol{u};\, \boldsymbol{u}', \boldsymbol{x}, t)$ represents the switching probability at position $\boldsymbol{x}$ and time t. Note that, $\int r(\boldsymbol{u};\, \boldsymbol{u}', \chi)d\boldsymbol{u} = 1$.

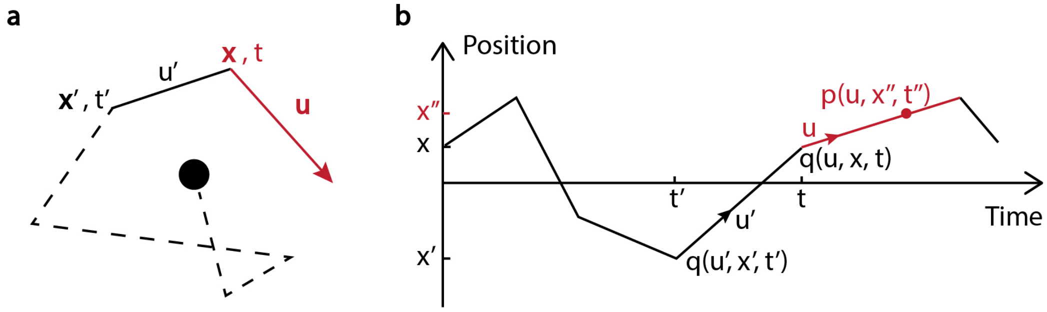

Figure. 4.1: **Schematic illustration of the microscopic motion of a particle.** **a**, 2D particle motion represented by connected line segments. **b**, 1D particle motion over time, where rates $q(\boldsymbol{u}', \boldsymbol{x}', t')$, $q(\boldsymbol{u}, \boldsymbol{x}, t)$ and probability density $p(\boldsymbol{u}, \boldsymbol{x}'', t'')$ are indicated.

For easy understanding, an example of the 1D particle motion along vertical direction is plotted in terms of time in Figure 4.1 b. The particle distribution at phase space is described by probability density $p(\boldsymbol{u}, \boldsymbol{x}, t)$, which is the probability of observing a particle at position $\boldsymbol{x}$ at time t with velocity $\boldsymbol{u}$. $\int p(\boldsymbol{u}, \boldsymbol{x}, t)\, d\boldsymbol{u}\, d\boldsymbol{x}\, dt = 1$. We further define a rate $q(\boldsymbol{u}, \boldsymbol{x}, t)$ to represent particles whose sojourns end at position $\boldsymbol{x}$ and time t and are going to move with a new velocity $\boldsymbol{u}$ in the next time step. Note that $\int q(\boldsymbol{u}, \boldsymbol{x}, t)\, d\boldsymbol{u}\, d\boldsymbol{x}\, dt \neq 1$. $p(\boldsymbol{u}, \boldsymbol{x}, t)$ and $q(\boldsymbol{u}, \boldsymbol{x}, t)$ satisfy master equations

$$q(\boldsymbol{u}, \boldsymbol{x}, t) = p_0(\boldsymbol{u}, \boldsymbol{x})\delta(t) + \int r(\boldsymbol{u};\, \boldsymbol{u}', \boldsymbol{x}, t)\, d\boldsymbol{u}' \int d\boldsymbol{x}' \int_0^t dt' q(\boldsymbol{u}', \boldsymbol{x}', t')\, \delta(\boldsymbol{x} - \boldsymbol{x}' - \boldsymbol{u}'(t - t'))\, \phi(t - t') \tag{4.1}$$

$$p(\boldsymbol{u}, \boldsymbol{x}, t) = \int d\boldsymbol{x}' \int_0^t dt' q(\boldsymbol{u}, \boldsymbol{x}', t')\, \delta(\boldsymbol{x} - \boldsymbol{x}' - \boldsymbol{u}(t - t'))\, \Phi(t - t') \tag{4.2}$$

$p_0(\boldsymbol{u}, \boldsymbol{x})$ is the initial probability distribution. Equation 4.1 is derived from the consideration that when a particle arrives at $\mathbf{x}$ and t, it is because at previous time $t^{'}$ $(0 < t^{'} < t)$ the particle starts moving from location $\mathbf{x}^{'}$ with a velocity $\mathbf{u}^{'}$, where $\mathbf{x} - \mathbf{x}^{'} = \mathbf{u}^{'}(t - t^{'})$. After arriving at $\mathbf{x}$ and time t, its velocity changes from $\mathbf{u}^{'}$ to $\mathbf{u}$. Equation 4.2 considers that when a particle passes by location $\mathbf{x}$ at time t, it means at a previous time $t^{'}$ $(0 < t^{'} < t)$ the particle starts moving from location $\mathbf{x}^{'}$ with a velocity $\mathbf{u}$, where $\mathbf{x} - \mathbf{x}^{'} = \mathbf{u}(t - t^{'})$, and the persistence time of the particle is equal to or longer than $t - t^{'}$. It should be noted that $q(\boldsymbol{u}, \boldsymbol{x}, t)$ only represents particles at the end of a sojourn, while $p(\boldsymbol{u}, \boldsymbol{x}, t)$ represents particles along a sojourn and at the end of a sojourn,

4.4 Fickian diffusion with drifting

First, we consider the particle moves in a static and memoryless environment. That is $r(\boldsymbol{u};\, \boldsymbol{u}', \chi) = r(\boldsymbol{u};\, \boldsymbol{u}', \boldsymbol{x})$ and $\phi(t_p) = \gamma e^{-\gamma t_p}$, where γ is a model parameter.

Equation 4.1 can be rewritten as

$$q(\boldsymbol{u},\boldsymbol{x},t) = p_0(\boldsymbol{u},\boldsymbol{x})\delta(t) + \int r(\boldsymbol{u};\mathbf{u}',\mathrm{x})d\boldsymbol{u}' \int_0^t q[\boldsymbol{x}-\boldsymbol{u}'(t-t'),\boldsymbol{u}',t']\phi(t-t')dt' \quad (4.3)$$

Based on Taylor expansion,

$$q[\boldsymbol{x}-\boldsymbol{u}'(t-t'),\boldsymbol{u}',t'] = \sum_{n=0}^{\infty} \frac{[-\boldsymbol{u}'\cdot\bigtriangledown]^n}{n!} q(\boldsymbol{x},\boldsymbol{u}',t')(t-t')^n \quad (4.4)$$

Perform Laplace transform to get

$$\hat{q}(\boldsymbol{u},\boldsymbol{x},s) = \hat{p_0}(\boldsymbol{u},\boldsymbol{x}) + \int r(\boldsymbol{u};\boldsymbol{u}',\mathrm{x}) \frac{\gamma\hat{q}(\boldsymbol{u}',\boldsymbol{x},s)}{s+\gamma+\boldsymbol{u}'\cdot\bigtriangledown} d\boldsymbol{u}' \quad (4.5)$$

Perform Taylor expansion and Laplace transform on equation 4.2 to get

$$\hat{p}(\boldsymbol{u},\boldsymbol{x},s) = \frac{\hat{q}(\boldsymbol{u},\boldsymbol{x},s)}{s+\gamma+\boldsymbol{u}\cdot\bigtriangledown} \quad (4.6)$$

Combine equations 4.5 and 4.6 to get

$$s\hat{p}(\boldsymbol{u},\boldsymbol{x},s) - \hat{p_0}(\boldsymbol{u},\boldsymbol{x}) + \boldsymbol{u}\cdot\bigtriangledown\hat{p}(\boldsymbol{u},\boldsymbol{x},s) = \gamma \int r(\boldsymbol{u};\boldsymbol{u}',\boldsymbol{x})\hat{p}(\boldsymbol{u}',\boldsymbol{x},s)d\boldsymbol{u}^{'} - \gamma\hat{p}(\boldsymbol{u},\boldsymbol{x},s) \quad (4.7)$$

Performing inverse Laplace transform leads to

$$(\partial_t + \boldsymbol{u}\cdot\bigtriangledown)p(\boldsymbol{u},\boldsymbol{x},t) = \gamma \int r(\boldsymbol{u};\boldsymbol{u}',\boldsymbol{x})\, p(\boldsymbol{u}',\boldsymbol{x},t)d\boldsymbol{u}' - \gamma p(\boldsymbol{u},\boldsymbol{x},t) \quad (4.8)$$

The partial differential equation (PDE) 4.8 states that the changing rate of particles at $(\boldsymbol{u},\boldsymbol{x})$ is determined by their spatial motion (particles move into or out of position $\boldsymbol{x}$) and motion in phase space (particles change velocity between $\boldsymbol{u}$ and $\boldsymbol{u}'$). Note that a similar PDE is reported in study [137] derived based on the Langevin approach. Assuming the magnitude of velocity U is constant, and the changing of velocity direction is independent of space and follows Gaussian distribution. Specifically, $r(\boldsymbol{u};\, \boldsymbol{u}', \chi) = r(\theta;\, \theta') = (\frac{\Lambda}{2\pi k})^{3/2} exp\Big[-\frac{(\theta - \theta' + \alpha\theta'/\Lambda)^2}{4k/\Lambda}\Big]$, the PDE can be further simplified to Kramers-Fokker-Planck equation [138] as

$$(\partial_t + U\boldsymbol{n}_\theta \cdot \bigtriangledown)p(\theta, \boldsymbol{x}, t) = \frac{\gamma}{\Lambda}\big[\alpha \bigtriangledown_\theta \cdot(\boldsymbol{n}_\theta p(\theta, \boldsymbol{x}, t)) + k\Delta_\theta p(\theta, \boldsymbol{x}, t)\big] \tag{4.9}$$

Next, we derive the asymptotic solution for equation 4.8. When the magnitude of velocity is a constant U, $r(\boldsymbol{u}; \boldsymbol{u}^{'}, \chi) = r(\theta; \boldsymbol{x})$, where θ is the angular difference between $\boldsymbol{u}$ and $\boldsymbol{u}'$. Perform a moment expansion on PDE 4.8 to get

$$\partial_t p_x + \frac{U}{2} \bigtriangledown \cdot[\overline{p}_x + \rho,\, \overline{p}_y] = \gamma(\boldsymbol{x})\rho \int r(\theta; \boldsymbol{x}) \cos\theta d\theta - \gamma(\boldsymbol{x})p_x \tag{4.10}$$

$$\partial_t p_y + \frac{U}{2} \bigtriangledown \cdot[\overline{p}_y,\, \rho - \overline{p}_x] = \gamma(\boldsymbol{x})\rho \int r(\theta; \boldsymbol{x}) \sin\theta d\theta - \gamma(\boldsymbol{x})p_y \tag{4.11}$$

$$\partial_t \rho + U \bigtriangledown \cdot[p_x,\, p_y] = 0 \tag{4.12}$$

Where $p = p(\theta, \boldsymbol{x}, t)$, $p_x = pcos\theta$, $p_y = psin\theta$, $\overline{p}_x = \int p \cos 2\theta d\theta$, $\overline{p}_y = \int p \sin 2\theta d\theta$, and $\rho = \int pd\theta$. At long times, $\overline{p}_x = \overline{p}_y = \partial_t p_x = \partial_t p_y = 0$ [137]. Therefore, at long time, particle motion follows

$$\partial_t \rho = U \bigtriangledown \cdot\big[\frac{U}{2\gamma(\boldsymbol{x})} \bigtriangledown \rho\big] - U\, \rho \bigtriangledown \cdot\big[\int r(\theta; \boldsymbol{x}) \cos\theta d\theta,\, \int r(\theta; \boldsymbol{x}) \sin\theta d\theta\big] \tag{4.13}$$

Equation 4.13 shows that at the long time scale, the particle motion is a combination of diffusion and directional drifting. Diffusion, described by the right first term, can be represented by a point-wise diffusion coefficient $D(\boldsymbol{x}) = \frac{U^2}{2\gamma(\boldsymbol{x})}$. Directional drifting, described by the right second term, can be represented by a net velocity (advection velocity) $\boldsymbol{u}_{av} = [U \int r(\theta; \boldsymbol{x}) \cos\theta d\theta,\ U \int r(\theta; \boldsymbol{x}) \sin\theta d\theta]$.

The PDE 4.8 is numerically solved with periodic boundaries. In the first case, the model is applied to study the diffusion of particles in homogeneous (specifically,

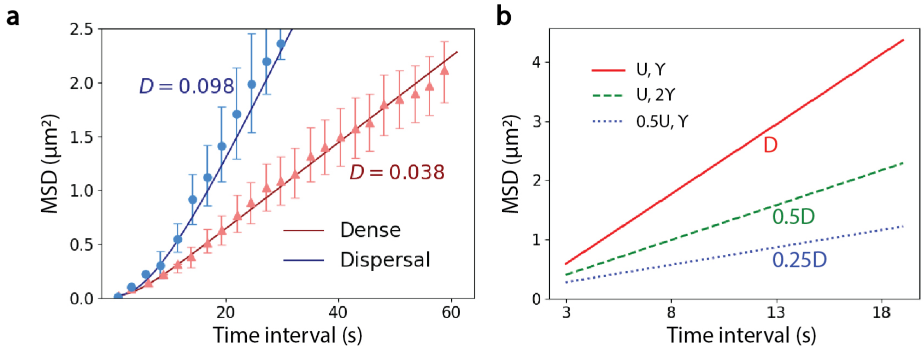

Figure. 4.2: **The MSD of the particle in dense and dispersal networks of tracks.** In a dense network, the particle speed and persistent time are reduced due to frequent collisions with the tracks and switching directions at the intersections, the diffusion coefficient is smal. Vice versa. Triangles and dots represent the experimental measurements. Solid lines are the results calculated from PDE 4.8.

$r(\theta; \boldsymbol{x}) = \dfrac{1}{2\pi}$) polymer networks. In the experiment [139], particle speed is measured as $72 \pm 4\, nm/s$ in a dense network and $80 \pm 5\, nm/s$ in a dispersal network. Mean particle persistence (value of $1/\gamma$) is $200 \pm 20\, nm$ in a dense network and $600 \pm 40\, nm$ in a dispersal network. The mean square displacement (MSD) of the particle calculated by PDE is compared with the experimental measurements, as shown in Figure 4.2 a. At the initial transient stage, the particle motion is superdiffusive. At long times, particle performs diffusion with a diffusion coefficient $D = \dfrac{U^2}{2\gamma}$ (Figure 4.2 b). In the second case, the probabilities of switching from velocity direction θ_1 to θ_2 are non-uniformly distributed and are influenced by the difference between two angles, denoted as $r(\theta) = r(|\theta_1 - \theta_2|)$. Specifically, three types of distribution are studied. Type 1: $r(\theta) = \dfrac{\cos^4 \theta}{\int_0^{2\pi} \cos^4 \theta d\theta}$; Type 2: $r(\theta) = \dfrac{\cos^2 \theta}{\int_0^{2\pi} \cos^2 \theta d\theta}$; Type 3: $r(\theta) = \dfrac{\cos^2 \theta + 0.5}{\int_0^{2\pi} (\cos^2 \theta + 0.5) d\theta}$. At long time, particle motion is diffusive with directional drifting. The MSD follows power law (MSD $\propto t^{\alpha}$, $\alpha > 1$), as shown in Figure 4.3. The second case could potentially be used to investigate and explain the relationships between polymer heterogeneity and particle motions. For example, the formation of the outgoing flux of intracellular particles toward the cell periphery [140] could be explained based on the model by considering the majority of the tracks are pointing outward.

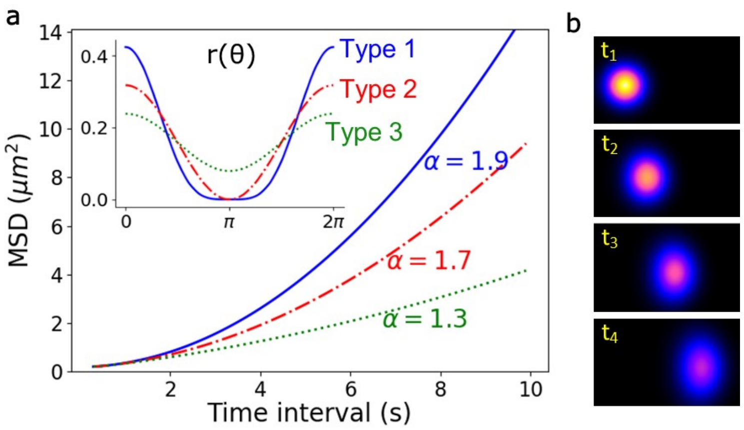

Figure. 4.3: **The angular heterogeneity leads to the directional drifting of particles.** **a**, Three types of distributions $r(\theta)$ and the corresponding MSDs of particles. **b**, Snapshots of particle probability distributions at different time with type 1 angular heterogeneity.

4.5 Anomalous Fickian diffusion

Next, we consider the particle moves in a static, homogeneous environment. However, particles that move fast are likely to maintain or terminate moving direction at the end of a sojourn. That is $r(\theta;\, \theta', \chi) = r(\theta;\, \theta', U')$. Consequently, the persistent time of each sojourn is correlated with its moving speed. Thus, we let $r(\theta;\, \theta', \chi) = \dfrac{1}{2\pi}$, but $U = f(t_p)$. The correlation between particle speed and persistence is widely seen in many biological systems. For example, Maiuri et al. found that cells that migrate faster are likely to maintain their migration direction because actin flows generated in motile cells reinforce cell polarity and consequently cell persistence [42]. They showed that the correlation between persistent time t_p and instantaneous velocity v of cells with either a mesenchymal migration mode (e.g. retinal pigment epithelial cells) or an amoeboid migration mode (e.g. bone marrow-derived dendritic cells) follows a simple exponential distribution as $t_p = Ae^{\lambda v}$. In the intracellular cytoplasm, the active components, such as motor proteins and polymerization of cytoskeleton, modify the fluctuating forces on the particle. Since the particle velocity and persistence are originated from random active forces, factors that influence forces will inevitably lead to simultaneous changes in velocity and persistence. For example, when motor proteins transport a particle along the track, the external load on the particle reduces the transport velocity as well as the persistent time [141, 142]. Therefore, particles that frequently switch directions and that persist a very long distance can both be observed in the cytoplasm [58].

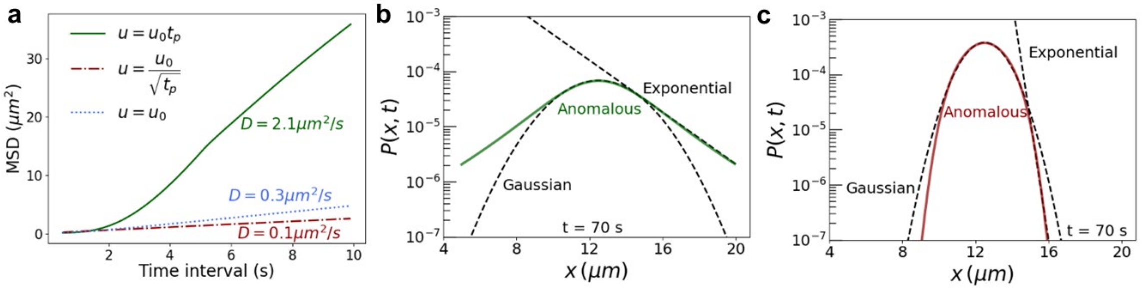

Figure. 4.4: **Anomalous Fickian diffusion stems from the correlated velocity and persistence.** **a**, The MSD at long times is proportional to time when the speed U is positively, negatively correlated and uncorrelated to the persistent time t_p. **b**, **c** The probability distribution of the particle displacements at the center horizontal line of the space when $t = 70s$. The velocity is positively correlated (in **b**) and negatively correlated (in **c**) to the persistent time. The center portion of the distributions follows Gaussian ($\propto e^{-x^2}$) and the tails are exponentially distributed ($\propto e^{-x}$).

In this section, two types of velocity-persistence correlations are discussed. Specifically, particle speed U is proportional to persistent time t_p or $t_p^{-1/2}$. By numerically solving Equations 4.1 and 4.2 with periodic boundaries, the results show that the time required for initial transition to equilibrium has been extended, but the particle motions remain Fickian diffusive (i.e. $\langle \Delta \mathbf{x}^2 \rangle \propto t$) at long times (Fig. 4.4 a). When velocity is positively correlated to persistence ($U = U_0 t_p$, where U_0 is a constant parameter), the diffusion coefficient is strikingly larger than it in Gaussian Fickian diffusion. Since the diffusion coefficient only holds information of second-order cumulants, we then analyzed the full probability distribution of the particle displacements (Fig. 4.4 b and c). We find that the center portion of the distribution remains Gaussian, but the large displacements decay exponentially slower. The exponential distribution in Fig. 4.4 b stems from the self-reinforced particle persistent direction. And it causes the significant increment of the diffusion coefficient. When velocity is negatively correlated to persistence ($U = U_0 t_p^{-1/2}$), the large displacements decay exponentially faster than the Gaussian distribution. It should also be noted that the anomalous particle distribution will eventually recover to a Gaussian as required by the center limit theorem.

The non-Gaussian distribution in anomalous Fickian diffusion (also named as anomalous *yet* Brownian diffusion by Wang et al. [143, 144]) has been observed in several physical systems, including beads on the surface of a lipid bilayer tube, beads in an entangled solution of actin filaments, and liposomes in a nematic solution [143, 144, 145]. Granick's group and Chubynsky, Mykyta et al. analyzed this strange diffusion phenomenon by decomposing particle displacement distribution into normal modes and representing each mode by an effective diffusivity [144, 146]. They found that the environmental heterogeneity can be reflected by the distribution of the effective diffusivities. Here, from a physical and biological point of view, our results indicate that a fundamental cause of the unevenly distributed diffusivities is the correlation between particle velocity and persistence. That is the switching of direction at the end of a sojourn depending on the historical traveling speed. We expect further experiments to test our hypothesis that particles in the cytoplasm or other systems with the universal velocity-persistence correlation will show Fickian but Non-Gaussian diffusion.

4.6 Anomalous diffusion

Finally, the effects of self-reinforced directionality influenced by historical traveling distance are studied based on the GPRW model. Recall that in a memoryless system, the direction of each sojourn is independent of the history and the persistent time is exponentially distributed. However, in many biological and ecological systems, the distribution of persistent time is observed as long-tailed [127, 126, 8]. A possible view of the long-tailed distribution is that the directionality can be reinforced at the end of a sojourn. Particles that have performed a long sojourn are likely to maintain the traveling direction and move an extremely long distance.

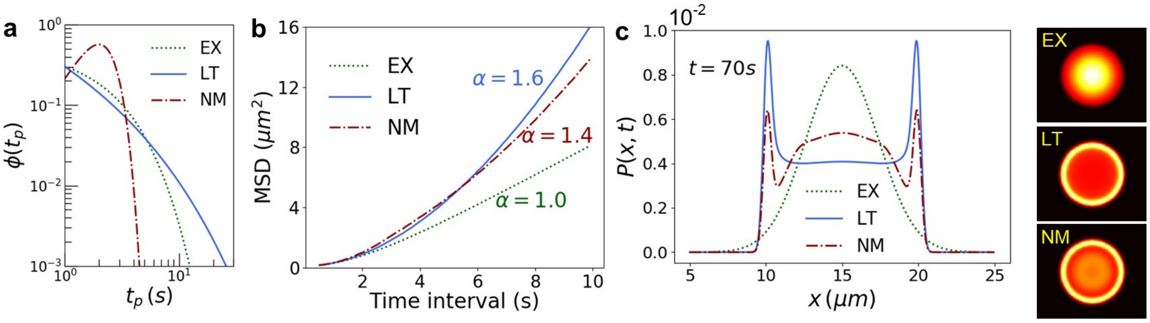

Figure. 4.5: **The self-reinforced directionality leads to the superdiffusion of particle.** **a**, The distribution of persistent time. EX represents the exponential distribution ($\gamma e^{-\gamma t_p}$, $\gamma = 0.5$); LT represents the long tailed distribution ($\gamma t_p^{\gamma-1} e^{-t_p^{\gamma}}$, $\gamma = 0.5$); NM represents the normal distribution ($t_p \sim N(2,1)$). **b**, The MSD over time. $\alpha = 1$ is Brownian; $\alpha > 1$ is superdiffusive. **c**, The probability distribution of particle displacement at the center horizontal line of the space (plot, normalized) and in the 2D space (images). The color in the 2D images represents the probability $P(\mathbf{x}, t)$.

Two types of persistence distribution other than exponential distribution are studied here. Specifically, the long tail distribution ($\phi(t_p) = \gamma t_p^{\gamma-1} e^{-t_p^{\gamma}}$) and normal distribution ($t_p \sim N(2,1)$) (Figure 4.5 a). Figure 4.5 b shows that other than exponentially distributed persistence, the long tail and normal distribution of persistence lead to superdiffusion of particle at both short and long times. While the majority of particles remains close to the initial position in the Gaussian Fickian diffusion, in superdiffusion, most particles move away and form circular patterns (Figure 4.5 c and d). In addition, when the experimentally measured distribution $\phi(t_p)$ of endosomal proteins in intracellular cytoplasm is used [8], the results also show a superdiffusion phenomenon (Figure 4.6). Specifically, in the experiments, more than 40000 runs of endosomes are measured, and the persistent distance (i.e. distance the endosome is transported before switching moving direction) follows power law distribution. By assuming the endosome moves with constant speed, the distribution of persistent time $\phi(t_p)$ also follows same power law distribution, shown by the grey dots in Figure 4.6 a. To calculate the endosomal distribution and its MSD over time based on the GPRW model, the distribution of persistent time is approximated based on fitting the long-tailed distribution formula $\phi(t_p) = \gamma t_p^{\gamma-1} e^{-t_p^{\gamma}}$ to the experimental data. When $\gamma = 0.45$, the continuous approximation curve, shown by the blue curve in Figure 4.6 a, can be used to replace the discrete experimental measurements. Using the continuous analytic formula $\phi(t_p)$, the particle distribution and MSD are calculated based on master equations 4.1 and 4.2. The results in Figure 4.6 b show that the MSD is super-linear in time, which indicates that endosomes perform superdiffusive motion.

Note that, the superdiffusion is usually described by a generalized Langevin equation (GLE) as

$$m\frac{d}{dt}u(t) = -m\int\limits_0^t \Gamma(t-t_1)u(t_1)dt_1 + F(t) \tag{4.14}$$

where $\Gamma(t)$ is the memory kernel. When $\Gamma(t) \sim t^{-\alpha}$, it can be shown that $\lim_{t\to\infty}\langle x^2(t)\rangle \propto t^{\alpha}$ [147]. The GLE indicates that when the viscosity decreases fast enough with the time the particle has persisted ($\alpha > 1$), the process is superdiffusive at long times. In other words, superdiffusion happens when the probability of maintaining traveling directions increases along the persistent path.

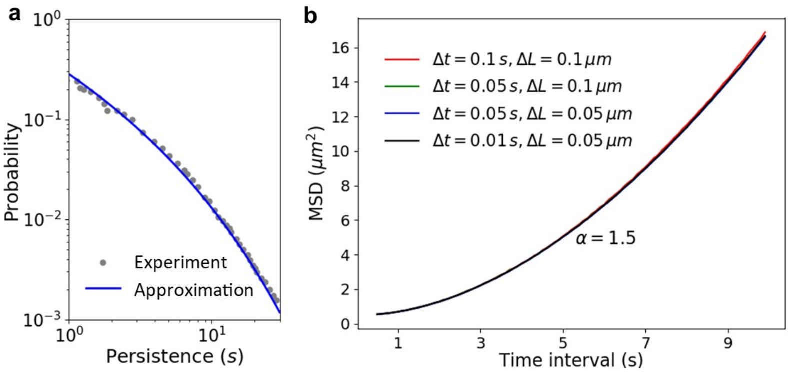

Figure. 4.6: **The superdiffusion originated from the long tailed distribution of persistence.** **a**, the experimentally measured distribution of the persistent time [8] is shown by grey dots and an analytic formula $\phi(t_p) = 0.45 t_p^{-0.55} e^{-t_p^{0.45}}$, used to approximate the experimental results, shown by the solid line. **b**, the MSD of the particle over time calculated by the master equations using the approximation formula $\phi(t_p)$. The MSD follows power law (i.e. $MSD \propto t^{\alpha}$, $\alpha = 1.5$). Different discretizations of time and space lead to the same calculation results.

4.7 Discussion

In this work, we extended the PRW model to study effects of angular heterogeneity on the anomalous diffusion and transport. We showed that when the angular heterogeneity is spatial dependent but memoryless, analytic results can be formally derived by performing Laplace transform and the results indicate particles perform drift diffusion asymptotically. In the system with memory, the mechanism of self-reinforced directionality influenced by historical speed and persistent time drives the system away from Gaussian Fickian diffusion. Specifically, when speed and persistence is correlated, particles perform Fickian but non-Gaussian diffusion. When persistence is long-tailed distributed, particles perform superdiffusion. The self-reinforced directionality indicates that the time and space are no longer linked by a simple constant velocity as in the PRW model. The distorted (stretched) spatial-temporal coupling is probably the origin of the anomalous diffusion and transport phenomena. But further careful analysis and formal proves are needed. It is also interesting to study and understand if and how the external energy input could help reconstruct the diffusion process by modifying the spatial-temporal coupling and maintaining the system out of equilibrium.

CHAPTER V

Developmental Progression of Embryonic-like Tissues

5.1 Abstract

Early human embryonic development involves complex spatial cellular organization, lineage specification and tissue dynamics. To reveal mechanisms that govern early embryonic development and how they are disrupted in disease, in vitro 3D stem cell models that can self-organize into embryonic-like structures have been proposed and start to become more widely accepted and used. However, the heterogeneity and complexity inside self-organizing stem cell models limits the ability to clearly identify reliable and significant factors that control tissue growth and pattern formation. Here, we proposed a high-throughput automatic tissue profiling technique for fast and easy extraction of morphological and proteinomic features from embryonic-like tissue images, as well as exploration and quantification of large image feature data sets with single-cell resolution. Based on the tissue profiling technique, the similarity between tissue samples is measured and used to inference a bifurcating developmental trajectory and recover essential tissue developmental stages.

5.2 Introduction

Embryonic development, regulated by multi-level signaling interactions, is a robust and complex process involving a series morphological transformations. Despite its fundamental and clinical importance, mechanisms that refine cellular patterns and lead to diverse adult forms are less understood because of the limited accessibility to human embryo specimens and ethical restrictions. Studies based on mouse and other mammalian embryos have provided informed knowledge about pre-implantation development until the formation of blastocyst because pre-implantation is fairly conserved among species. During post-implantation period, however, distinct embryonic architectures among species emerge and direct application of mouse embryology to human system become questionable. Human embryonic stem cells (hESCs) exhibit many molecular and cellular similarities with post-implantation epiblast cells in human embryo, and are shown to have the potential to differentiate into three germ layers [55]. Therefore, in vitro synthetic models constructred from hESCs are important alternatives for studying post-implantation human embryo development [148, 54]. Recently proposed synthetic embryonic models that can recapitulate some level of in vivo-like cell patterns and morphologies include 2D micro-patterned hESC colonies, 3D hESC aggregates embedded in gel matrix or cultured in engineered microfluidic devices. Specifically, Warmflash et al. showed that cells within geometrically defined colonies exposed to BMP4 are able to form ordered array of germ layers including trophectoderm, ectoderm and mesendoderm along the radial axis [149]. In three dimensional (3D) conditions, Shao et al. observed the in vivo-like lumenogenesis and amniogenesis of hESC aggregates cultured inside a thick gel bed. They found that a fluid-filled cavity is formed inside the cell aggregates and some cells are able to differentiate into amniotic-like cells at a proper initial cell seeding density [50, 51]. Zheng et al. achieved controllable generation of asymmetric amniotic cavity with dorsal-ventral patterning by applying BMP4 to one side of the cell aggregates using a microfluidic device [52]. And Simunovic et al. studied the spontaneous anterior-posterior patterning by embedding hESC aggregates in polymeric hydrogel supplemented with a small dose of BMP4 [53]. Until now, however, only limited phenomenological observations have been provided based on the synthetic embryonic models, because of the heterogeneity inside self-organizing systems (i.e. systems proposed by Shao et al. [50, 51] and Simunovic et al. [53]) and limited culturing time and space and complicated experimental procedures in engineered systems (i.e. systems proposed by Warmflash et al. [149] and Zheng et al. [52]). To perform high-throughput and unbiased quantification of the phenotype of synthetic embryonic models, identify underlying regulatory factors and gain insights about early human development, we developed an automated and highthroughput imaging analysis workflow, also being known as a tissue profiling technique, that enables systematic evaluation of morphology and protein expressions of hESC aggregates cultured inside 3D gel matrix. In this chapter, I will first introduce the self-organizing embryonic models used to generate asymmetric embryonic-like tissues in a high-throughput manner. This experimental method enables acquiring a large amount of immunostaining images at different time points to study tissue developmental progression. Next, I will discuss the image analysis pipeline, containing two major parts segmentation and feature extraction, developed to measure morphological and staining features and use these features as a full phenotypical spectrum of biological tissues. In the end, the high dimensional feature set is analyzed based on advanced statistical tools to inference a continuous bifurcating developmental trajectory. Some preliminary biological insights about the embryonic-like tissue development acquired from the analysis will also be presented.

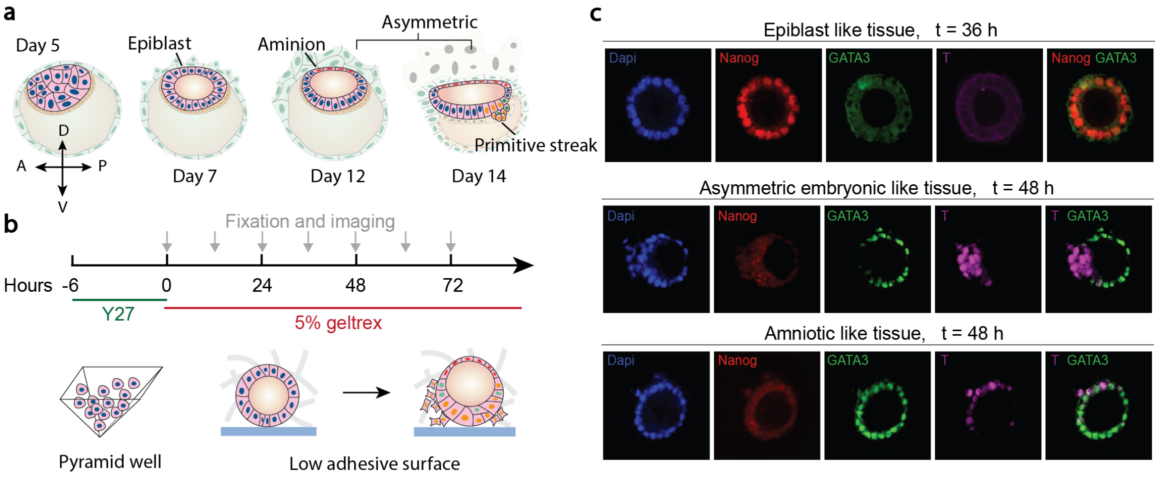

Figure. 5.1: **Controlled generation of three dimensional (3D) embryonic like tissues.** **a**, In vivo development of post-implantation human embryo. **b**, Workflow of generating embryonic like tissues from human embryonic stem cells (hESCs). **c**, Representative confocal images of the epiblast like tissue, asymmetric embryonic like tissue and amniotic like tissue stained for DAPI (nuclei), NANOG (stem cell), GATA3 (amniotic like cell) and T (primitive streak like cell).

5.3 Results

5.3.1 Generation of embryonic-like tissues

At day 5 of embryo development, the blastocyst contains a spherical aggregate of epiblast cells at one side of the cavity. Epiblast cells undergo apical-basal polarization and lumenogenesis which results in the formation of pro-amniotic cavity. At around day 12, the amniotic cavity becomes asymmetric where on side of epiblast cells differentiate into squamous amniotic ectoderm and another side of cells maintain columnar shape. The formation of bipolar amniotic cavity defines the dorsal-ventral body axis. Afterwards, the posterior epiblast cells go through epithelial-mesenchymal transition and form primitive streak (Figure 5.1 a) [52]. We sought to reproducibly generate aggregate of hESCs which mimic day 5 epiblast cells in pyramidal devices. Isolated hESCs cultured in pyramid wells establish cell-cell contact and merge together after 6 hours. Cell aggregates are then transferred to the 96 well plates with low adhesive surface for long-time 3D suspension culture. We found that 5% geltrex mixed with mTeSR medium is the optimal matrix to support the growth of hESC aggregates (Figure 5.1 b). At different time points after culturing hESC aggregates in the 3D matrix, a part of tissues are harvested for immunofluorescent staining. In general, we observed the existence of three types of tissues. The first type tissue has a single spherical lumen surrounded by a layer of NANOG^{+}, OCT^{+} pluripotent columnar epiblast-like cells. Because the tissue structure and cell type are similar to day 7 epiblast, it is referred to as epiblast-like tissue. After culturing for 48 h, all cells have lost NANOG expression and exited from pluripotency. A part of tissues grow into asymmetric structures with GATA3+ and T+ cells. Squamous cells express GATA3, a putative amniotic ectoderm marker, and columnar cells express T and acquire mesenchymal like property. The asymmetric structures recapitulate the bipolar posterior-side embryonic sac at around 12 days in vivo. Thus, this type of tissue is is referred to as asymmetric embryonic-like tissues. Another part of tissues, usually small-size tissues, containing only GATA3+ cells, are referred to as amniotic-like tissues (Figure 5.1 c).

5.3.2 Image based tissue profiling

To quantify tissue properties, including tissue morphology and cell type, we transferred fluorescent confocal images to statistical measurements based on a self-developed automatic image processing workflow. The workflow contains two major steps, segmentation and feature extraction. Segmentation is used to provide a simplified representation of a tissue image, which contains only boundaries of tissues and individual cells. Feature extraction provides mathematical quantification of tissue structure and fluorescent intensity. Specifically, for whole tissue segmentation, an intensity based watershed segmentation algorithm on a binary mask generated by Gaussian filter (or median filter) is applied to the image (Figure 5.2 a). To identify individual cells based

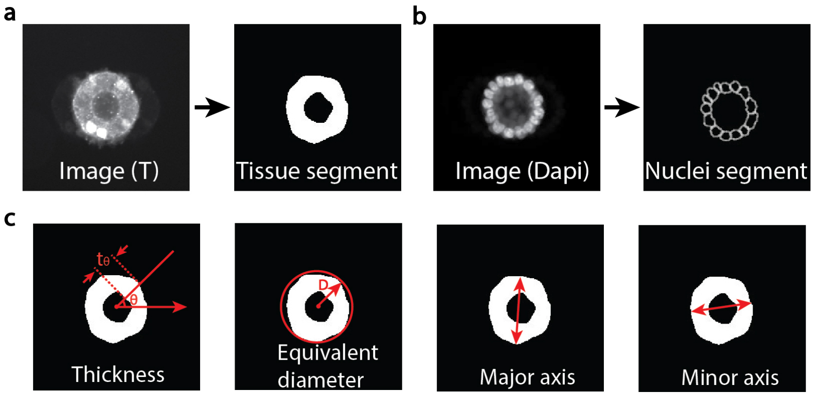

Figure. 5.2: **Schematic illustrations of tissue segmentation, nuclei segmentation and morphological features.** **a**, Tissue segmentation based on fluorescent staining image of marker T. Tissue area is labeled in white. **b**, Nuclei segmentation based on fluorescent staining of Dapi. Boundaries of cell nucleus are labeled as white. **c**, Schematic representation of four morphological features, including thickness t_θ, equivalent diameter D, major axis length and minor axis length.

on nuclei staining, a shape based watershed algorithm is used because clumped cells usually can not be separated by less intense borders. First, cell clusters are separated by applying Otsu thresholding. Then the thresholding image is transformed into a distance image where the intensity of each pixel represent the distance from that pixel to the nearest background pixel. Watershed algorithm is then applied to the inverted intensity image to separate cells within a cluster based on roundness. In the end, objects whose size beyond the manually defined size range is filtered out (Figure 5.2 b).

Fourteen meaningful morphological features are extracted from tissue segmentation and used to distinguish symmetric and asymmetric tissues. Asymmetric tissues have a thin amniotic epithelium at one side of the cavity and a thick cell layer at the opposite side, while symmetric tissue has a relatively uniform cell layer surrounding the cavity (Figure 5.1 c). Therefore, tissue thickness, t_θ, is introduced. As shown in Figure 5.2 c, t_θ is defined as the thickness at angle θ ($\theta \in [0,\ 2\pi]$) in polar coordinate, where the center of the coordinate system is at the mass center of the cavity. The

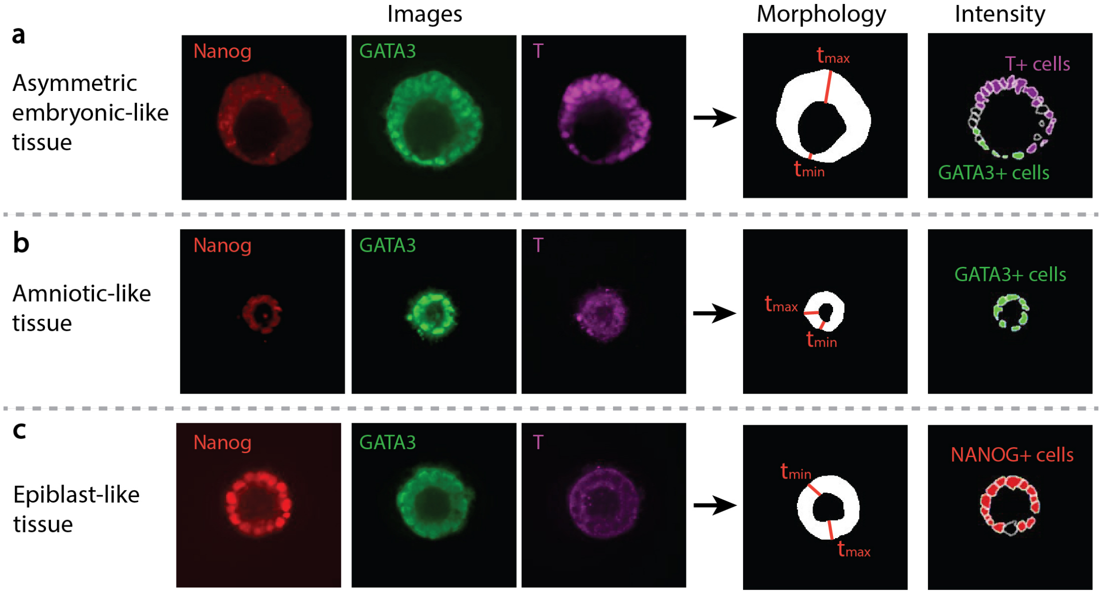

Figure. 5.3: **Morphological and intensity features of three types of tissues.** **a**, Asymmetric embryonic-like tissue. **b**, Amniotic-like tissue. **c**, Epiblast-like tissue. Left three image columns are tissues co-stained with NANOG, GATA3 and T. Right two image columns are tissue segmentation and nuclei segmentation. In nuclei segmentation, GATA3$^+$ cells identified by the algorithm is labeled as green, T$^+$ cells are labeled in purple and NANOG$^+$ cells are labeled as red. Cells labeled in black are identified as not expressing any marker.

symmetry of a tissue is quantified by thickness ratio r, where $r = \dfrac{\max(t_\theta)}{\min(t_\theta)}$. For a symmetric amniotic-like tissue or epiblast-like tissue, r is close to 1. For an asymmetric embryonic-like tissue, r is much larger than 1. To quantify the size of a tissue, equivalent diameter defined as the diameter of the smallest circle that can cover the whole tissue area is used (Figure 5.3 c). To quantify the roundness of a tissue, major axis length and minor axis length are calculated. Major axis length is defined as the length between two furthest vertices on the outer boundary of the tissue, and minor axis length is the length between two closest vertices on the boundary (Figure 5.3 c). More morphological features and their definitions are listed in Table 5.1.

Thirteen intensity features are extracted based on nuclei segmentation. For each tissue, three markers, GATA3, NANOG and T, are co-stained. The average intensity of a cell nuclei is calculated, and a manually defined threshold is used to identify GATA3$^+$, NANOG$^+$ and T$^+$ cells, as shown in Figure 5.3. Furthermore, to quantify the distribution of different types of cells, intensity gyration is introduced. Intensity gyration is defined as the distance between mass center of positive cells and tissue center. For example, GATA3_gyration represents the distance between mass center of GATA3$^+$ cells and tissue center. GATA3_T gyration is the distance between mass center of GATA3$^+$ cells and mass center of T$^+$ cells. Therefore, if GATA3_T gyration is large, it suggests that GATA3$^+$ cells and T$^+$ cells are distributed at two opposite sides of the tissue. More intensity features and their definitions are listed in Table 5.1.

5.3.3 Analysis of tissue properties

After automatically acquiring 27 features for more than 600 tissue samples, for each feature i ($i \in [1, 27]$), feature values of all samples are normalized to zero mean and unit variance. The Pearson correlation heatmap of 27 normalized features is shown in Figure 5.4. The 14 morphological features except lumen eccentricity

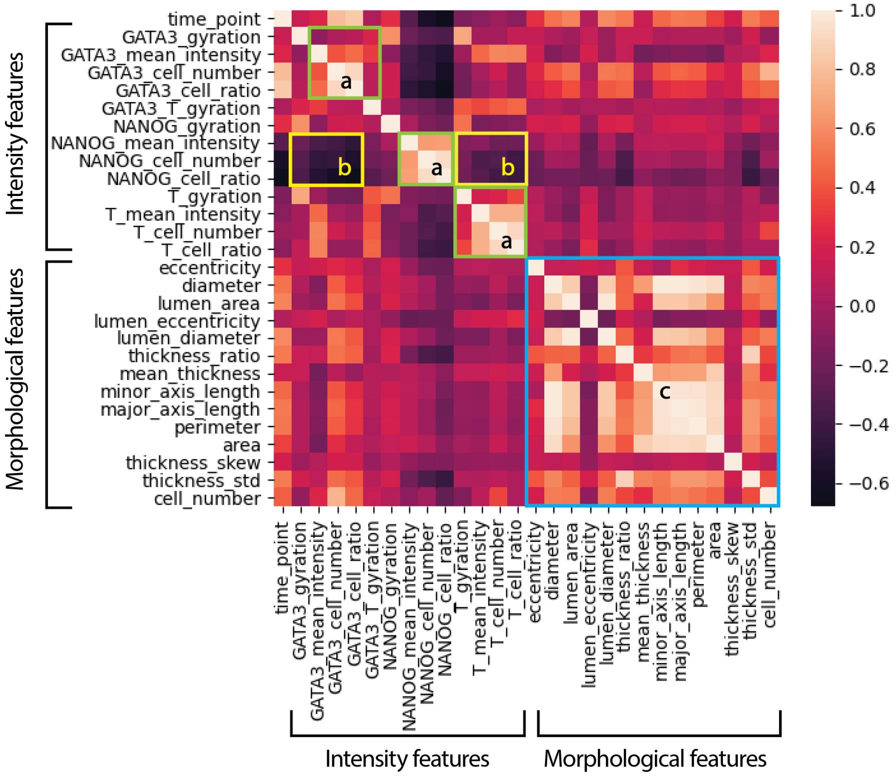

Figure. 5.4: **Pearson correlation heatmap of normalized morphological and intensity features.** Colors represent correlation between each pair of features.

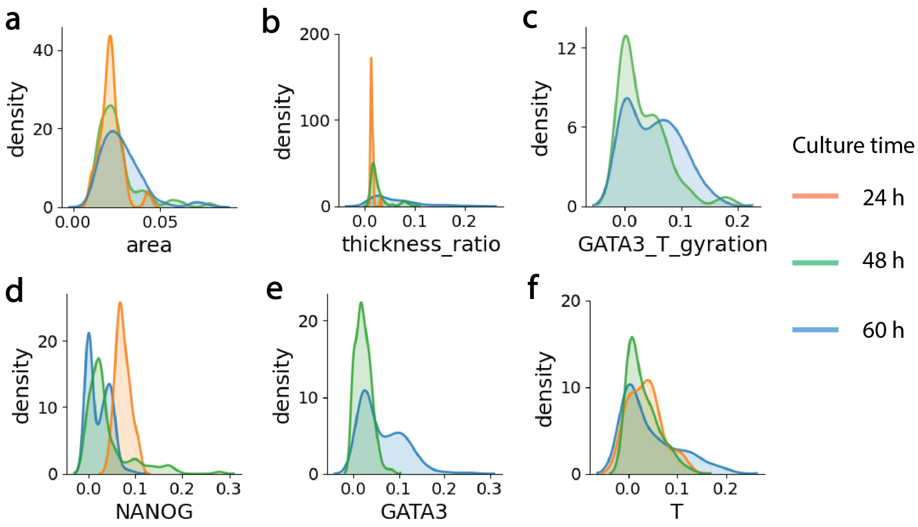

Figure. 5.5: **Distributions of six representative features, including area, thickness ratio, GATA3 T gyration, NANOG mean intensity, GATA3 mean intensity and T mean intensity, of tissues fixed at different time points.** Colors represent time duration of culturing tissues in gel matrix. Kernel density estimation is used to acquire continuous feature distribution from discrete samples.

are positively correlated (Figure 5.4 c). Intensity features of the same marker have stronger correlation with each other (Figure 5.4 a). NANOG intensity features are negatively correlated with GATA3 intensity features and T intensity features (Figure 5.4 b), which indicates NANOG and GATA3, T are exclusively expressed in cells. It agrees with the fact that NANOG is expressed in pluripotent cells and GATA3 and T are expressed when cells begin to differentiate. In addition, some features such as major axis length, minor axis length and perimeter are highly correlated; thus, not all of them are needed in later analysis.

Next, tissue properties characterized by morphological and intensity features are analyzed. From density distribution profiles of tissue features, it is shown that the average of tissue area and thickness ratio increases over time (Figure 5.5 a and b), which indicates that tissues keep growing and could become structural asymmetric. GATA3 is not expressed in cells at 24 hours. At 48 and 60 hours, the distributions of GATA3_T_gyration, which represents the separation between GATA3$^+$ cells and

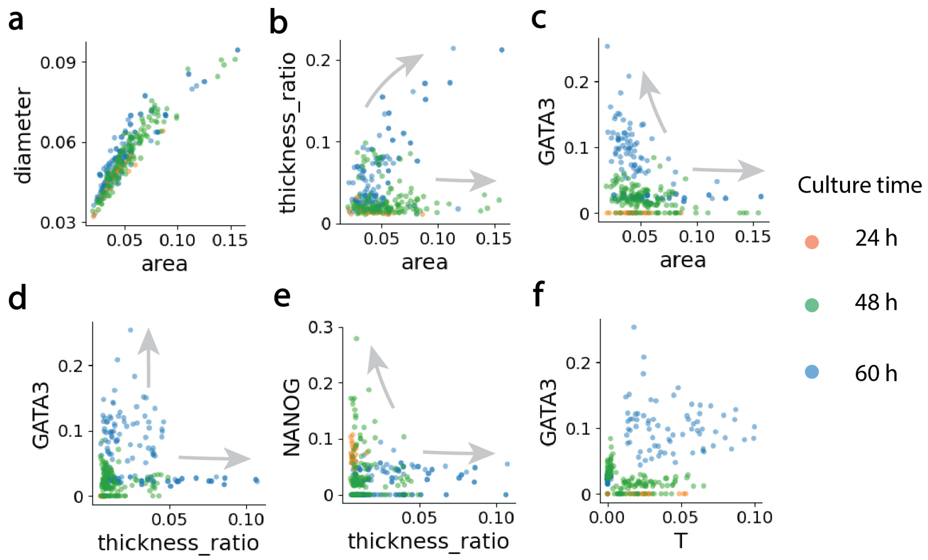

Figure. 5.6: **Scatter plots of pairs of tissue features.** **a**, Tissue equivalent diameter is positively correlated with tissue area. **b**, Tissue thickness ratio separates into two branches at large area. **c**, GATA3 mean intensity over tissue area. **d**, GATA3 mean intensity over thickness ratio. **e**, NANOG mean intensity over tissue thickness ratio. **f**, Relationship between GATA3 mean intensity and T mean intensity. Each dot represents one tissue sample. Colors represent the culturing time of tissues in gel matrix.

T^+ cells, have two peaks. In asymmetric tissues, $GATA3^+$ cells and T+ cells locate at two opposite sides of the tissue, which are represented by the peak that has large GATA3_T_gyration value. Another peak whose center locates at around 0 suggests that these differentiated cells are randomly or uniformly distributed in symmetric tissues. At 60 hours, the density of having separated two types of cells and their separation distance is large (Figure 5.5 c). The average expression level of NANOG is the highest at 24 hours and decreases in later times (Figure 5.5 d). GATA3 intensity increases over time, indicating a proportion of cells differentiate into amniotic-like cells (Figure 5.5 e). The average expression level of T is the lowest at 48 hours (Figure 5.5 f).

Furthermore, relationships between pairs of tissue features are studied. As expected, tissue diameter increases with tissue area, because they are both describing tissue size. Sizes of the majority of tissues at 24 hours are smaller than tissue sizes at 48 and 60 hours. But the size difference at 48 and 60 hours is not substantial (Figure 5.6 a). For large size tissues, a part of them has large thickness ratio and another part is symmetric (Figure 5.6 b). At 60 hours, small size tissues have higher GATA3 expression level than large tissues (Figure 5.6 c). And the thickness ratio of tissues that have strong GATA3 expression is usually small (Figure 5.6 d), which indicates those are symmetric amniotic-like tissues. NANOG is expressed at 24 hours and in a small portion of symmetric tissues at 48 hours (Figure 5.6 e). At 48 hours, one group of tissues expresses GATA3 but not T and another group of tissues expresses T but not GATA3. At 60 hours, many tissues have both GATA3 and T expressions (Figure 5.6 f).

5.3.4 Bifurcating developmental progression of tissues

From scatter plots of tissue features, separated branches with distinct properties are observed (indicated by grey arrows in Figure 5.6). We therefore hypothesize that tissue development following bifurcating trajectory and yields different structures and cell types. To quantify the tissue developmental progression and pinpoint when bifurcation happens, continuous single-tissue trajectory is learned using the imaging multidimensional feature space. Specifically, tissue samples are first ordered based on their morphological similarities. Then, a continuous trajectory is inferred from subsamples of temporal progression with fixed tissue time courses. Furthermore, intensity features are mapped onto the developmental trajectory to acquire the dynamical expression of NANOG, GATA3 and T (Figure 5.7). Details of trajectory inference method are provided in section 5.57.

In Figure 5.8 a, three distinct branches can be observed. The trunk part contains small symmetric tissues. During development, a part of these small tissues follow branch 2 trajectory to grow large as well as maintaining symmetry. Another part

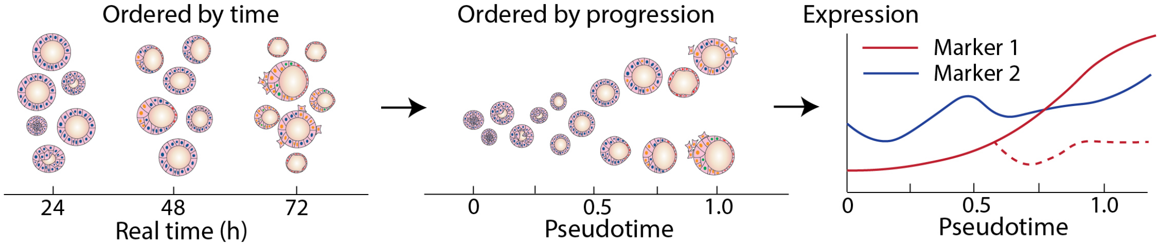

Figure. 5.7: **Schematic illustration of the inference of tissue developmental trajectory.** Tissue samples are harvested and imaged at discrete time points. Based on morphological similarities, tissue samples are projected onto a new coordinate system to acquire bifurcating trajectory. Along trajectory, the dynamical changes of tissue morphology and fluorescent maker intensity are predicted.

of tissues goes through symmetry breaking along branch 1 trajectory. The developmental bifurcation starts around 0.4 psuedotime. Afterwards, two groups tissues acquire different morphological and intensity features. In symmetric branch, tissue area keeps increasing while thickness ratio is always low. In asymmetric branch, a transient plateau of tissue growth appears right after the bifurcation point, probably because cells undergo differentiation instead of proliferation. The growth of asymmetric tissues is rewoke after 0.7 psuedotime (Figure 5.8 b). We also examined trends of mean intensities of NANOG and T along the trajectory. However, since the average intensities are calculated over the whole tissue without any image preprocessing such as illumination correction, the standard deviation of the results is large. Moreover, the mixture of amniotic-like tissue and epiblast tissue in one branch also influence results, because cells in epiblast-like tissue express NANOG but cells in amniotic-like tissue should express GATA3. Nevertheless, some interesting findings can be observed based on the intensity trajectories. For example, in the asymmetric branch, the NANOG intensity decreases after bifurcation because cells loose pluripotency and then increases probably because some cells differentiate into PGC-like cells and start to express NANOG again [52]. The increasing of NANOG intensity happens also around 0.7 psuedotime when tissues start to regrowth. T intensity keeps

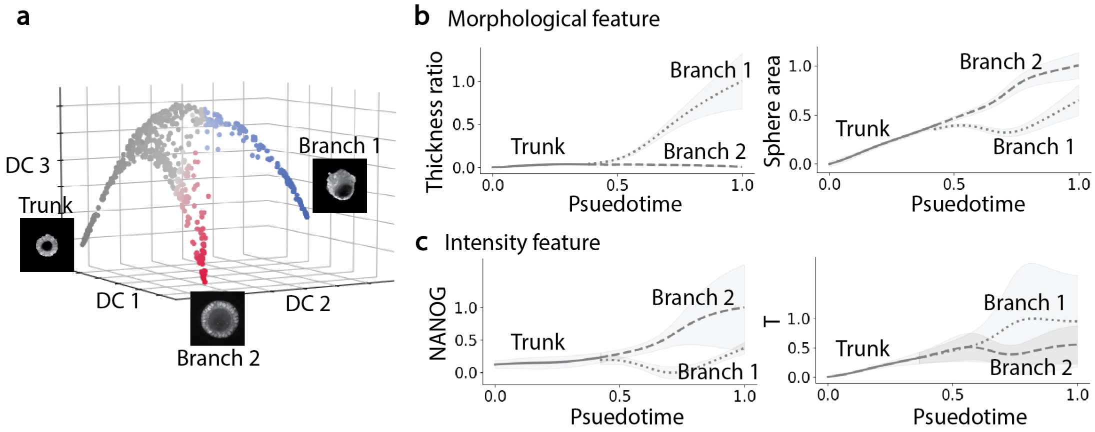

Figure. 5.8: **Trajectory of embryonic-like tissue development.** **a**, Diffusion map for embryonic-like tissues (n = 694 tissues). Colour-coding denotes the trunk and two bifurcating branches. **b**, Morphological features, thickness ratio and area, along trajectory. **c**, Intensity features, NANOG mean intensity and T mean intensity, along trajectory. The light grey areas represent the standard deviation.

increasing before bifurcation. After bifurcation, T intensity quickly reaches to the maximum value at around 0.7 psuedotim (Figure 5.8 c). Furthermore, to verify the inference results, live cell imaging of the growth of tissues can be acquired. For example, the increasing of tissue area inferred based on different tissue samples acquired at discrete time points can be compared with the growing of an individual tissue measured based on continuous live cell imaging. A parametric sensitivity analysis can also be performed to study the influence of modeling parameters, including the intensity thresholds used to extract tissue morphology and identify individual cells and parameters for trajectory inferences (Table 5.2).

5.4 Conclusion and future outlook

In this chapter, we developed a high throughput image based cell profiling strategy to quantify the bifurcating developmental progression of embryonic-like tissues. We described the experimental and computational methods developed and showed preliminary results to demonstrate the feasibility of the proposed methods.

The image based tissue profiling strategy can be further improved and used to investigate mechanisms that controls symmetry breaking and cell fate selection, and provide insights about post-implantation embryo development. For example, it would be interesting to explore the influence of mechanobiological factors on the differentiation of amniotic-like cells and formation of asymmetric cavity. In the experiments, we discovered that symmetry breaking and formation of three types of tissues (asymmetric embryonic-like tissue, amniotic-like tissue and epiblast-like tissue) is influenced by initial cell seeding density and initial tissue size. At an intermediate cell seeding density, the percentage of asymmetric embryonic-like tissues is the highest, and amniotic-like tissues and epiblast-like tissues are observed simultaneously. At a large cell seeding density, tissue keeps growing large while maintains symmetric structure. Inside the large symmetric tissues, cells start to differentiate into mesoendoderm like cells and express protein Brachyury (T), which agrees with the phenomenon reported by Simunovic et al. [53]. At a small cell seeding density, the majority of tissues are symmetric amniotic-like tissues with a squamous cavity. Therefore, it is possible that single cells could sense the 'population context', resulting in microenvironmental effects that regulate gene expression and cell differentiation. Recently, it has been shown that many extracellular mechanical cues, including matrix rigidity, external stretch and cell density can lead to prominent F-actin cytoskeleton formation and promote a high nuclear YAP/TAZ activity [150]. We therefore stained and visualized YAP distribution in three types of tissues, shown in Figure 5.9. Interestingly, nuclear accumulation of YAP was observed in small amniotic-like tissues and the squamous side of asymmetric embryonic-like tissues, which indicates that the differentiation of amniotic-like cells may be correlated with the nuclear accumulation of YAP protein. To test whether the bifurcating differentiation of ESCs into amniotic-like cells and mesodermal-like cells is influenced by mechanobiological factors (e.g. tissue size and extracellular matrix stiffness) through YAP/TAZ signaling, the proposed methods

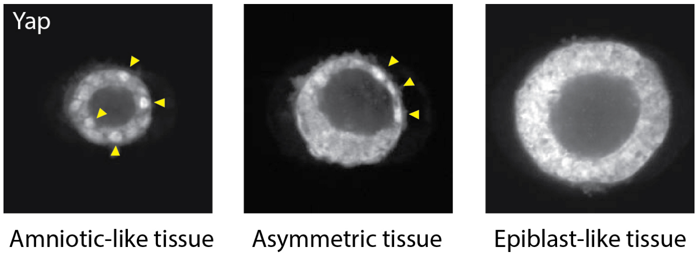

Figure. 5.9: **Nuclear accumulation of YAP in small amniotic-like tissue (left), asymmetric embyronic-like tissue (middle) and large epiblast-like tissue (right).**

can be used to analyze the expression level and spatial distribution of YAP proteins during the development when tissues are cultured inside various gel matrix or under different drug perturbations.

Inference of protein expression profiles along the developmental trajectory, such as Figure 5.8 c, is limited by the availability of primary antibodies and immunostaining accuracy. To improve the inference accuracy and acquire a comprehensive understanding of the genetic and proteinomic fluctuations during development, mapping the bulk RNA sequencing or single cell RNA sequencing results onto the developmental trajectory becomes important. Traditionally, RNA sequencing and trajectory inference focus on identifying stages and fates of cells cultured in 2D conditions [151]. For 3D tissues, RNA sequencing datasets provide only limited information because important spatial positions of different types and stages of cells has been lost during sequencing. To reconstruct spatially resolved gene expression data, one recent study proposed to measure the mRNA content of tissue cells based on fluorescence *in situ* hybridization and then map the RNA sequencing data onto the tissue based on a panel of landmark genes [152]. Another method is to optimize sequencing technique such that the spatial information of cells is included in the DNA barcodes [153]. It would be interesting to explore the possibility of combining the image based tissue profiling algorithm with strategies that can spatially map sequencing data onto the tissues in order to reconstruct a spatial-temporal evolution of gene expression during tissue development.

5.5 Methods

5.5.1 Ethics statement

The embryonic like tissues lack the primitive endoderm and the trophoblast, and thus cannot form yolk sac and placenta, respectively. Therefore, these embryonic-like tissues do not have human organismal form or potential. Furthermore, all experiments were terminated by no later than day 4 in vitro. All protocols used in this work with hESCs to model early post-implantation human embryo development have been approved by Human Pluripotent Stem Cell Research Oversight Committee at University of Michigan, Ann Arbor.

5.5.2 Cell line

H9 human embryonic stem cell (WA09, WiCell; NIH registration number: 0062) is used in this study. The H9 cell line has been authenticated by the original sources as well as by immunostaining for pluripotency markers and successful differentiation to three germ layer cells. The H9 cell line was authenticated as karyotypically normal at the indicated passage number by Cell Line Genetics (Madison, USA). The H9 cell line was tested negative for mycoplasma contamination (LookOut Mycoplasma PCR Detection Kit, SigmaAldrich).

5.5.3 Cell culture

H9 cell line is maintained in a standard feeder-free culture system using mTeSR1 medium (STEMCELL Technologies) and lactate dehydrogenase-elevating virus (LDEV)-free hESC-qualified reduced growth factor basement membrane matrix Geltrex$^{\text{TM}}$ (Thermo Fisher Scientific; derived from Engelbreth-HolmSwarm tumors similarly as

Matrigel) per the manufacturers instructions. H9 cells were used before P70.

5.5.4 Tissue generation and culturing

PDMS-based pyramidal devices are generated by replica-molding using AggreWell^{TM} 400 (StemCell Technologies). Briefly, to make a template containing an array of pyramidal posts, PDMS prepolymer was poured over the AggreWell, cured at 60 °for 12 hours, peeled off, oxidized with air plasma (Plasma Prep II; SPI Supplies) and silanized with (tridecafluoro-1,1,2,2,-tetrahydrooctyl)-1-trichlorosilane vapor 1 hour under vacuum. To generate the final PDMS pyramidal wells, PDMS prepolymer was poured over the template, degassed under vacuum, cured at 60 °for another 12 hours and peeled off the template.

Low adhesive 96 well plate were prepared one day before the tissue generation experiment. To prepare the hydrogel coating solution, 1.2 g poly-HEMA (Sigma-Aldrich) is dissolved in 40 ml ethanal at 37 °for 6 hours on the plate rotator. The hydrogel coating solution is then added to the 96 well plate (30 μl per well) in a fully opened hood overnight to dry.

To generate aggregates of hESCs, cultured hESCs were dissociated with Accutase (Sigma-Aldrich) at 37 °for 10 min, centrifuged and resuspended in mTeSR1 containing 10 μM Y27632 (Tocris). hPSC were plated as single cells into the pyramidal device. After 6 hours, single cells already merge together to form cell aggregates. Cell aggregates were transferred out of device, centrifuged and resuspended in mTeSR1 with 5% geltrex without Y27632. Medium with cell aggregates was added to the 96 well plate with low adhesive surfaces (150 μl per well) for long term culture.

5.5.5 Immunocytochemistry and microscopy

H9 cell aggregates or long-time cultured tissues were fixed in 4% paraformaldehyde (prepared in 1× PBS) for 3 hours, and permeabilized in 0.1% SDS (sodium dodecylsulfate, dissolved in PBS) solution for another 3 hours. Samples were blocked in 4% donkey serum solution (Sigma-Aldrich) at 4 °for 24 hours before incubation with primary antibody solution at 4 °for another 24 hours. Samples were labeled with donkey secondary antibodies (1:500 dilution) at 4 °for 24 hours. Dapi (Thermo Fisher Scientific) was used for counterstaining cell nuclei. Alexa-fluor 488, 561 or 640 dye-conjugated wheat germ agglutinin (WGA; Thermo Fisher Scientific) was used as a pan-cell membrane marker. Primary antibodies and their sources and dilutions are based on the work of Zheng et al. [52]. More than 600 tissues are fixed at different time points and stained for NANOG, GATA3, T, TFAP2A and YAP.

Images were acquired on an Olympus 1X81 fluorescent microscope equipped with a CSU-X1 spinning-disc unit (YOKOGAWA) or a Nikon-A1 laser scanning confocal microscope (Nikon).

5.5.6 Trajectory inference

The dataset that contains 14 morphological features of 694 tissues is first normalized to zero mean and unit variance. Then, similarities between any two tissue samples i and j ($i, j \in [1,\ 694]$), defined as $c_{ij} = e^{-|\boldsymbol{x}_i - \boldsymbol{x}_j|^2/2\epsilon}$, are calculated. where $\boldsymbol{x}_i$ is the column vector of the morphological features of tissue i; ϵ is a model parameter and $\epsilon = 0.05$ in this study. When tissues i and j have similar morphology, $|\boldsymbol{x}_i - \boldsymbol{x}_j|$ is close to 0, and the similarity of the two tissues c_{ij} is close to 1. When tissues i and j have different morphology, $|\boldsymbol{x}_i - \boldsymbol{x}_j|$ is large and c_{ij} is close to 0. In a statistical point of view, defining a similarity matrix $C = c_{ij}$ for the dataset in a nonlinear way as $c_{ij} = e^{-|\boldsymbol{x}_i - \boldsymbol{x}_j|^2/2\epsilon}$ ensures the relationship between analogous tissues (close data points) being preserved while distinct tissues (data points far way from each other) playing negligible role in the calculation. Next, eigendecomposition is applied to the similarity matrix C and the first three eigenvectors, also referred to as diffusion components (DCs), are used as a low dimensional representation of the information inside

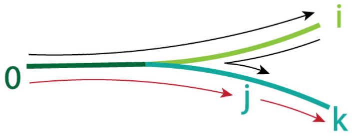

Figure. 5.10: **Schematic illustration of branch identification based on mutual disagreement matrix.**

the dataset. Note that, the eigendecomposition process also helps reduce unnecessary noise inside the dataset by projecting the information onto a new coordinate system, and the low dimensional visualization of the dataset is also referred to as diffusion map in many other studies [154].

Morphological similarity c_{0i} between a tissue 0 at initial developmental stage and a tissue i at late developmental stage is used to represent the maturity of tissue i. Therefore, tissue developmental progression can be obtained by tissue ordering based on values of c_{0i}. Specifically, based on the first eight diffusion components, previously proposed algorithm Wishbone is slightly adopted to order tissues and calculate their developmental maturity, which is also referred to as developmental psuedotime [155]. Specifically, we first manually select a small symmetric tissue which locates at the left end of the trunk branch in Figure 5.8 a as the initial stage of development (psuedotime = 0). Then, the shortest path between a tissue i ($i \in [1, 694]$) and the initial stage, denoted as D_{0i} on diffusion map is calculated. All the lengths D_{0i}, $i \in [1, 694]$ are normalized between 0 and 1. These normalized lengths provide a quantitative measure of the morphological difference between a tissue and the initial developmental stage, and therefore is used to represent tissue developmental maturity (developmental psuedotime). Afterwards, to distinguish branches, we select a sub-sample of tissues (150 tissues in this study) and calculate the mutual disagreement matrix Q between pairs of sub-sampled tissues. For sub-sampled tissues i and j, the mutual disagreement is calculated as $Q_{ij} = |D_{0i} + D_{ij} - D_{0j}|$, where D_{ij} represents the shortest path length between i and j. If tissues i and j are on two different branches, as shown in Figure 5.9, $D_{0i} + D_{ij}$ shown by black arrows is much larger than D_{0j} shown by a red arrow. Thus, $Q_{ij} \gg 0$. Otherwise, if tissues j and k are on the same branch, $Q_{jk} = D_{0j} + D_{jk} - D_{0k}$ is close to zero. Finally, continuous traces of morphological and intensity features during development are calculated as weighted averages of tissue feature values. To acquire a continuous traces from scattered tissue data points, for each single tissue, we assume its feature value follows a Gaussian distribution whose center is the development psuedotime and variance is determined by the variance of the whole dataset based on Silverman's approximation [156]. For the trunk part, the weighted average and variance over all tissues are calculated. For bifurcating branches, the influence of tissues on a different branch is muted before calculating the weighted average.

5.5.7 Feature extraction

5.5.8 Model parameters

Feature Name	**Definition**
Mean thickness $\bar{t}$	$\frac{1}{N}\sum_{i=1}^{i=N} t(\frac{2\pi i}{N})$, where $t(\theta)$ is tissue thickness at angle θ.
Thickness standard deviation σ_t	$\sqrt{\frac{1}{N-1}\sum_{i=1}^{i=N}[t(\frac{2\pi i}{N})-\bar{t}]^2}$.
Thickness ratio r_t	$\max(t)/\min(t)$.
Thickness skewness	The skewness of thickness distribution. If an asymmetric tissue has a longer thin amniotic membrane, there is more weight in the left tail of thickness distribution and skewness value $>$ 0.
Area	Area of the cell layer surrounding the lumen in pixel.
Lumen area	Area of the lumen in pixel.
Eccentricity	A measure of how non-circular the outer tissue boundary is. Calculated by python module Scikit-Image.
Lumen eccentricity	A measure of how non-circular the inner tissue boundary (also the outer lumen boundary).
Diameter	The equivalent diameter (Figure 5.2 c) of tissue.
Lumen diameter	The equivalent diameter of lumen.
Major axis length	Length of major axis of tissue (Figure 5.2 c).
Minor axis length	Length of minor axis of tissue (Figure 5.2 c).
Perimeter	Perimeter of tissue outer boundary.
Cell number	Number of cell nucleus calculated based on nuclei segmentation results.
GATA3 gyration	Intensity gyration of GATA3 marker.
GATA3 mean intensity	Mean intensity of GATA3 among all cell nucleus.
GATA3 cell number	Number of GATA3$^+$ cells.
GATA3 cell ratio	The percentage of GATA3$^+$ cells.
NANOG gyration	Intensity gyration of NANOG marker.
NANOG mean intensity	Mean intensity of NANOG among all cell nucleus.
NANOG cell number	Number of NANOG$^+$ cells.
NANOG cell ratio	The percentage of NANOG$^+$ cells.
T gyration	Intensity gyration of T marker.
T mean intensity	Mean intensity of T among all cell nucleus.
T cell number	Number of T$^+$ cells.
T cell ratio	The percentage of T$^+$ cells.
GATA3_T_gyration	Length between mass center of GATA3$^+$ cells and mass center of T$^+$ cells.

Table 5.1: Summary of morphological and intensity features.

Parameter name	**Definition and value**
Intensity threshold I_1, I_2	I_1, I_2 are used to create tissue mask. Depending on the image intensity and quality, Otsu threshold or manually defined threshold are used.
Intensity threshold I_3, I_4	I_3, I_4 are used to identify cell clusters. Depending on the image intensity and quality, Otsu threshold or manually defined threshold are used.
Size range	Size range is used for nuclear segmentation. Areas beyond the size range will not be regarded as a cell nuclear. Size range = (5, 30) pixels.
Intensity threshold factor f	f is used to identify if cells express a specific marker, such as GATA3, T and NANOG. $f = \frac{\text{mean nuclear intensity}}{\text{cavity intensity}}$. If $f > 2.5$, cell expresses that specific marker. Otherwise, cell does not express the marker.
Parameters for diffusion map	metric = euclidean. alpha = 0.01. k = 10. n_evecs = 8. $\epsilon = 0.05$. The definition of these parameters is introduced in package website [157]
Parameters for Wishbone trajectory inference	k = 15. num_waypoints = 150. The definition of these parameters is introduced in paper [155].

Table 5.2: Parameters used in tissue profiling pipeline.

CHAPTER VI

Outlooks

As the famous statement by George E.P. Box and Norman R. Draper said, "*essentially, all models are wrong, but some are useful*". The computational models and tools developed in this dissertation only try to capture a part of the dynamics inside a complex biological system and study whether these dynamics play an important role in determining or influencing system functions. I think it is necessary to point out some limitations of these three proposed methods in the end of this dissertation and discuss possible future improvements and related applications.

6.1 Limitations of current models

- The multi-physics Monte Carlo model of intracellular cargo transport relies on accurate understanding and describing transport components, including cargo diffusion, kinesin walking motion, cargo-kinesin interaction and kinesin attaching to and detaching from microtubules. Since many simplifications are made for each transport component, it becomes hard to evaluate the effect of all simplifications on model predictions. For example, cargo is assumed to be a rigid sphere in the model, which is different from any in vivo cargoes such as soft spherical vesicles and long cylindrical neurofilaments. The walking motion of kinesins is assumed to be influenced only by resistant forces (i.e. forces pulling on the kinesin opposite to its walking direction) in the model, however, experimental observations have shown that assistant forces could also influence kinesin walking motion. Though validation of the model based on current experimental results suggest that these simplifications do not have significant influence on model predictions, it is not clear whether these simplifications matter and how accurate the model predictions can be applied in more general situations. In addition, this computational model contains a lot of model parameters and could suffer from overfitting issue. The model variance is reduced but the biased is increased at the same time.

- The probabilistic model developed to describe particle diffusion and transport in heterogeneous environment neglects physical sources that generate the motion, but only focuses on particle dynamics. It contains fewer parameters which avoid overfitting problem. At the same time, the proposed model provides a generalized and flexible framework to connect microscopic particle movements with macroscopic distributions. The limitation of this probabilistic model is the complicated formula of the two master equations in the model, which can be simplified to PDEs and asymptotic solutions only under few ideal conditions. Solving the two master equations numerically requires a large computational cost and could lead to large calculation errors.
- The image-based tissue profiling and trajectory inference algorithm is a data-driven and practical method for analyzing experimental measurements. Like many other statistical models, the proposed algorithm does not have a solid physics foundation nor requiring understanding of underlying mechanisms. It analyzes only the mathematical relationships between measured data points and results and conclusions do not provide explanation of causality. The model accuracy largely depend on features extracted from images. And for different

data types and structures, the trajectory inference algorithm should be modified accordingly. On the other hand, however, the proposed model contains less empirical guesses and assumptions, and could be helpful for understanding complex systems where system dynamics can not be simplified as a few physical laws.

6.2 Future outlooks

In practical perspective, I think it is important to connect computational models to experiments for meaningful predictions and conclusions. For example, when transport properties (e.g. transport length, speed, cargo distribution) inside healthy and impaired neuron axons are measured to be different, it would be interesting to apply the multi-physics model in chapters II and III to identify influential transport components and help understand possible mechanisms of neuronal impairment. Having measurements of protein distribution inside cells over time, the generalized walk model in chapter IV could be used to extract new protein diffusion statistics other than diffusion coefficient.

During my PhD, the computational models and tools I developed are becoming more generalized and relying on less physical laws. I believe though generalized models have large variance on predictions, they can be applied to many other different systems with reduced bias and potentially become more useful and impactful. For example, the image-based analysis and trajectory inference algorithm can potentially be used to study morphological changes of human body or moving objects, and predict future motions and dynamics.

REFERENCES

[1] L.A. Amos. Kinesin from pig brain studied by electron microscopy. *Journal of Cell Science*, 87(1):105–111, 1987.

[2] https://valelab4.ucsf.edu/external/moviepages/moviesmolecmotors.html.

[3] Patrick P. L. Tam and David A. F. Loebel. Gene function in mouse embryogenesis: get set for gastrulation. *Nature Reviews Genetics*, 8:368 – 381, 2007.

[4] Kotaro Sasaki, Tomonori Nakamura, Ikuhiro Okamoto, Yukihiro Yabuta, Chizuru Iwatani, Hideaki Tsuchiya, Yasunari Seita, Shinichiro Nakamura, Naoto Shiraki, Tetsuya Takakuwa, Takuya Yamamoto, and Mitinori Saitou. The germ cell fate of cynomolgus monkeys is specified in the nascent amnion. *Developmental Cell*, 39(2):169 – 185, 2016.

[5] Mark J. Schnitzer, Koen Visscher, and Steven M. Block. Force production by single kinesin motors. *Nature Cell Biology*, 2:718–723, 2000.

[6] Johan Andreasson, Bojan Milic, Geng-Yuan Chen, Nicholas Guydosh, William Hancock, and Steven Block. Examining kinesin processivity within a general gating framework. *Elife*, 4:e07403, 2015.

[7] Jennifer L. Ross, Henry Shuman, Erika L.F. Holzbaur, and Yale E. Goldman. Kinesin and dynein-dynactin at intersecting microtubules: Motor density affects dynein function. *Biophysical Journal*, 94(8):3115 – 3125, 2008.

[8] Kejia Chen, Bo Wang, and Steve Granick. Memoryless self-reinforcing directionality in endosomal active transport within living cells. *Nature Materials*, 14:589–593, 2015.

[9] Tsung-Li Liu, Srigokul Upadhyayula, Daniel E. Milkie, Ved Singh, Kai Wang, Ian A. Swinburne, Kishore R. Mosaliganti, Zach M. Collins, Tom W. Hiscock, Jamien Shea, Abraham Q. Kohrman, Taylor N. Medwig, Daphne Dambournet, Ryan Forster, Brian Cunniff, Yuan Ruan, Hanako Yashiro, Steffen Scholpp, Elliot M. Meyerowitz, Dirk Hockemeyer, David G. Drubin, Benjamin L. Martin, David Q. Matus, Minoru Koyama, Sean G. Megason, Tom Kirchhausen, and Eric Betzig. Observing the cell in its native state: Imaging subcellular dynamics in multicellular organisms. *Science*, 360(6386), 2018.

[10] Jan Drenth. principles of protein x-ray crystallography. *Springer Science and Business Media*, 2007.

[11] Daniel M. Suter and Kyle E. Miller. The emerging role of forces in axonal elongation. *Progress in Neurobiology*, 94(2):91 – 101, 2011.

[12] Lukas C. Kapitein and Casper C. Hoogenraad. Building the neuronal microtubule cytoskeleton. *Neuron*, 87(3):492 – 506, 2015.

[13] Scott T. Brady and Gerardo A. Morfini. Regulation of motor proteins, axonal transport deficits and adult-onset neurodegenerative diseases. *Neurobiology of Disease*, 105:273 – 282, 2017.

[14] Christine Stadelmann. Multiple sclerosis as a neurodegenerative disease: pathology, mechanisms and therapeutic implications. *Current Opinion in Neurology*, 24:224 – 229, 2011.

[15] A Jon Stoessl. Neuroimaging in the early diagnosis of neurodegenerative disease. *Translational Neurodegeneration*, 1, 2012.

[16] Stèphanie Millecamps and Jean-Pierre Julien. Axonal transport deficits and neurodegenerative diseases. *Nature Reviews Neuroscience*, 14:161 – 176, 2013.

[17] P. Hemachandra Reddy and Ulziibat P. Shirendeb. Mutant huntingtin, abnormal mitochondrial dynamics, defective axonal transport of mitochondria, and selective synaptic degeneration in huntington's disease. *Biochimica et Biophysica Acta (BBA) - Molecular Basis of Disease*, 1822(2):101 – 110, 2012.

[18] Kurt J. [De Vos] and Majid Hafezparast. Neurobiology of axonal transport defects in motor neuron diseases: Opportunities for translational research? *Neurobiology of Disease*, 105:283 – 299, 2017.

[19] Nobutaka Hirokawa, Shinsuke Niwa, and Yosuke Tanaka. Molecular motors in neurons: Transport mechanisms and roles in brain function, development, and disease. *Neuron*, 68(4):610 – 638, 2010.

[20] Judith Eschbach and Luc Dupuis. Cytoplasmic dynein in neurodegeneration. *Pharmacology and Therapeutics*, 130(3):348 – 363, 2011.

[21] John A. Hammer III and James R. Sellers. Walking to work: roles for class v myosins as cargo transporters. *Nature Reviews Molecular Cell Biology*, 13:13 – 26, 2012.

[22] Kristen J. Verhey, Debra Meyer, Rene Deehan, John Blenis, Bruce J. Schnapp, Tom A. Rapoport, and Ben Margolis. Cargo of Kinesin Identified as Jip Scaffolding Proteins and Associated Signaling Molecules. *Journal of Cell Biology*, 152(5):959–970, 2001.

[23] Gorazd B. Stokin, Concepción Lillo, Tomás L. Falzone, Richard G. Brusch, Edward Rockenstein, Stephanie L. Mount, Rema Raman, Peter Davies, Eliezer Masliah, David S. Williams, and Lawrence S. B. Goldstein. Axonopathy and

transport deficits early in the pathogenesis of alzheimer's disease. *Science*, 307(5713):1282–1288, 2005.

[24] Nathan A. Reed, Dawen Cai, T. Lynne Blasius, Gloria T. Jih, Edgar Meyhofer, Jacek Gaertig, and Kristen J. Verhey. Microtubule acetylation promotes kinesin-1 binding and transport. *Current Biology*, 16(21):2166 – 2172, 2006.

[25] Ram Dixit, Jennifer L. Ross, Yale E. Goldman, and Erika L. F. Holzbaur. Differential regulation of dynein and kinesin motor proteins by tau. *Science*, 319(5866):1086–1089, 2008.

[26] N. J. Carter and R. A. Cross. Mechanics of the kinesin step. *Nature*, 435:308 – 312, 2005.

[27] Dawen Cai, Dyke P. McEwen, Jeffery R. Martens, Edgar Meyhofer, and Kristen J. Verhey. Single molecule imaging reveals differences in microtubule track selection between kinesin motors. *PLOS Biology*, 7(10):1–14, 10 2009.

[28] Shaul Yogev, Roshni Cooper, Richard Fetter, Mark Horowitz, and Kang Shen. Microtubule organization determines axonal transport dynamics. *Neuron*, 92(2):449 – 460, 2016.

[29] Brigette Y. Monroy, Danielle L. Sawyer, Bryce E. Ackermann, Melissa M. Borden, Tracy C. Tan, and Kassandra M. Ori-McKenney. Competition between microtubule-associated proteins directs motor transport. *Nature Communications*, 9(1487), 2018.

[30] Qian Wang, Michael R. Diehl, Biman Jana, Margaret S. Cheung, Anatoly B. Kolomeisky, and José N. Onuchic. Molecular origin of the weak susceptibility of kinesin velocity to loads and its relation to the collective behavior of kinesins. *Proceedings of the National Academy of Sciences*, 114(41):E8611–E8617, 2017.

[31] Jared P. Bergman, Matthew J. Bovyn, Florence F. Doval, Abhimanyu Sharma, Manasa V. Gudheti, Steven P. Gross, Jun F. Allard, and Michael D. Vershinin. Cargo navigation across 3d microtubule intersections. *Proceedings of the National Academy of Sciences*, 115(3):537–542, 2018.

[32] Paul C. Bressloff and Jay M. Newby. Stochastic models of intracellular transport. *Rev. Mod. Phys.*, 85:135–196, Jan 2013.

[33] Merja Joensuu, Ramon Martnez-Mármol, Pranesh Padmanabhan, Nick R Glass, Nela Durisic, Matthew Pelekanos, Mahdie Mollazade, Giuseppe Balistreri, Rumelo Amor, Justin J Cooper-White, Geoffrey J Goodhill, and Frédéric A Meunier. Visualizing endocytic recycling and trafficking in live neurons by subdiffractional tracking of internalized molecules. *Nature Protocols*, 12:25902622, 2017.

[34] Adekunle T. Bademosi, Elsa Lauwers, Pranesh Padmanabhan, Lorenzo Odierna, Ye Jin Chai, Andreas Papadopulos, Geoffrey J. Goodhill, Patrik Verstreken, Bruno van Swinderen, and Frédéric A. Meunier. In vivo single-molecule imaging of syntaxin1a reveals polyphosphoinositide- and activity-dependent trapping in presynaptic nanoclusters. *Nature Communications*, 7(13660), 2016.

[35] Tajie H. Harris, Edward J. Banigan, David A. Christian, Christoph Konradt, Elia D. Tait Wojno, Kazumi Norose, Emma H. Wilson, Beena John, Wolfgang Weninger, Andrew D. Luster, Andrea J. Liu, and Christopher A. Hunter. Generalized lévy walks and the rold of chemokines in migration of effector cd8+ t cells. *Nature*, 485:545 – 548, 2012.

[36] G. Matthew Fricke, Kenneth A. Letendre, Melanie E. Moses, and Judy L. Cannon. Persistence and adaptation in immunity: T cells balance the extent and thoroughness of search. *PLoS Computational Biology*, 12(3):e1004818, 2016.

[37] Edward J. Banigan, Tajie H. Harris, David A. Christian, Christopher A. Hunter, and Andrea J. Liu. Heterogeneous cd8+ t cell migration in the lymph node in the absence of inflammation revealed by quantitative migration analysis. *PLoS Computational Biology*, 11(2):e1004058, 2015.

[38] Sabil Huda, Bettina Weigelin, Katarina Wolf, Konstantin V. Tretiakov, Konstantin Polev, Gary Wilk, Masatomo Iwasa, Fateme S. Emami, Jakub W. Narojczyk, Michal Banaszak, Siowling Soh, Didzis Pilans, Amir Vahid, Monika Makurath, Peter Friedl, Gary G. Borisy, Kristiana Kandere-Grzybowska, and Bartosz A. Grzybowski. Lvy-like movement patterns of metastatic cancer cells revealed in microfabricated systems and implicated in vivo. *Nature Communications*, 9(4539), 2018.

[39] Renske M. A. Vroomans, Athanasius F. M. Mare, Rob J. de Boer, and Joost B. Beltman. Chemotactic migration of t cells towards dendritic cells promotes the detection of rare antigens. *Plos Computational Biology*, 8(11):e1002763, 2012.

[40] Pei-Hsun Wu, Anjil Giri, Sean X. Sun, and Denis Wirtz. Three-dimensional cell migration does not follow a random walk. *Proceedings of the National Academy of Sciences*, 111(11):3949–3954, 2014.

[41] Elizaveta A. Novikova, Matthew Raab, Dennis E. Discher, and Cornelis Storm. Persistence-driven durotaxis: Generic, directed motility in rigidity gradients. *Phys. Rev. Lett.*, 118:078103, 2017.

[42] Paolo Maiuri, Jean-Franois Rupprecht, Stefan Wieser, Verena Ruprecht, Olivier Bnichou, Nicolas Carpi, Mathieu Coppey, Simon De Beco, Nir Gov, Carl-Philipp Heisenberg, Carolina Lage Crespo, Franziska Lautenschlaeger, Mal Le Berre, Ana-Maria Lennon-Dumenil, Matthew Raab, Hawa-Racine Thiam, Matthieu Piel, Michael Sixt, and Raphal Voituriez. Actin flows mediate a

universal coupling between cell speed and cell persistence. *Cell*, 161(2):374 – 386, 2015.

[43] Robert Kchl, Flavian Thelen, Lesley Vanes, Tiago F Brazo, Kathryn Fountain, Jian Xie, Chou-Long Huang, Ruth Lyck, Jens V Stein, and Victor L J Tybulewicz. Wnk1 kinase balances t cell adhesion versus migration in vivo. *Nature immunology*, 17:1075 – 1083, 2016.

[44] Thomas E. Angelini, Edouard Hannezo, Xavier Trepat, Manuel Marquez, Jeffrey J. Fredberg, and David A. Weitz. Glass-like dynamics of collective cell migration. *Proceedings of the National Academy of Sciences*, 108(12):4714–4719, 2011.

[45] Jin-Ah Park, Jae Hun Kim, Dapeng Bi, Jennifer A. Mitchel, Nader Taheri Qazvini, Kelan Tantisira, Chan Young Park, Maureen McGill, Sae-Hoon Kim, Bomi Gweon, Jacob Notbohm, Robert Steward Jr, Stephanie Burger, Scott H. Randell, Alvin T. Kho, Dhananjay T. Tambe, Corey Hardin, Stephanie A. Shore, Elliot Israel, David A. Weitz, Daniel J. Tschumperlin, Elizabeth P. Henske, Scott T. Weiss, M. Lisa Manning, James P. Butler, Jeffrey M. Drazen, and Jeffrey J. Fredberg. Unjamming and cell shape in the asthmatic airway epithelium. *Nature Materials*, 14:1040–1048, 2015.

[46] Dapeng Bi, J. H. Lopez, J. M. Schwarz, and M. Lisa Manning. A density-independent rigidity transition in biological tissues. *Nature Physics*, 11:1074–1079, 2015.

[47] Sri Ram Krishna Vedula, Man Chun Leong, Tan Lei Lai, Pascal Hersen, Alexandre J. Kabla, Chwee Teck Lim, and Benoît Ladoux. Emerging modes of collective cell migration induced by geometrical constraints. *Proceedings of the National Academy of Sciences*, 109(32):12974–12979, 2012.

[48] Alberto Puliafito, Lars Hufnagel, Pierre Neveu, Sebastian Streichan, Alex Sigal, D. Kuchnir Fygenson, and Boris I. Shraiman. Collective and single cell behavior in epithelial contact inhibition. *Proceedings of the National Academy of Sciences*, 109(3):739–744, 2012.

[49] Dapeng Bi, Xingbo Yang, M. Cristina Marchetti, and M. Lisa Manning. Motility-driven glass and jamming transitions in biological tissues. *Phys. Rev. X*, 6:021011, 2016.

[50] Yue Shao, Kenichiro Taniguchi, Ryan F. Townshend, Toshio Miki, Deborah L. Gumucio, and Jianping Fu. A pluripotent stem cell-based model for post-implantation human amniotic sac development. *Nature Communications*, 8(208), 2017.

[51] Yue Shao, Kenichiro Taniguchi, Katherine Gurdziel, Ryan F. Townshend, Xufeng Xue, Koh Meng Aw Yong, Jianming Sang, Jason R. Spence, Deborah L. Gumucio, and Jianping Fu. Self-organized amniogenesis by human pluripotent stem cells in a biomimetic implantation-like niche. *Nature materials*, 16:419 – 425, 2017.

[52] Yi Zheng, Xufeng Xue, Yue Shao, Sicong Wang, Sajedeh Nasr Esfahani, Zida Li, Jonathon M. Muncie, Johnathon N. Lakins, Valerie M. Weaver, Deborah L. Gumucio, and Jianping Fu. Controlled modelling of human epiblast and amnion development using stem cells. *Nature*, 573:421 – 425, 2019.

[53] Mijo Simunovic, Jakob J. Metzger, Fred Etoc, Anna Yoney, Albert Ruzo, Iain Martyn, Gist Croft, Dong Shin You, Ali H. Brivanlou, and Eric D. Siggia. A 3d model of a human epiblast reveals bmp4-driven symmetry breaking. *Nature cell biology*, 21:900 – 910, 2019.

[54] Marta N. Shahbazi, Eric D. Siggia, and Magdalena Zernicka-Goetz. Self-

organization of stem cells into embryos: A window on early mammalian development. *Science*, 364(6444):948–951, 2019.

[55] Tomonori Nakamura, Ikuhiro Okamoto, Kotaro Sasaki, Yukihiro Yabuta, Chizuru Iwatani, Hideaki Tsuchiya, Yasunari Seita, Shinichiro Nakamura, Takuya Yamamoto, and Mitinori Saitou. A developmental coordinate of pluripotency among mice, monkeys and humans. *Nature*, 537:57 – 62, 2016.

[56] Jennifer L Ross, M Yusuf Ali, and David M Warshaw. Cargo transport: molecular motors navigate a complex cytoskeleton. *Current Opinion in Cell Biology*, 20(1):41 – 47, 2008.

[57] David Breuer, Jacqueline Nowak, Alexander Ivakov, Marc Somssich, Staffan Persson, and Zoran Nikoloski. System-wide organization of actin cytoskeleton determines organelle transport in hypocotyl plant cells. *Proceedings of the National Academy of Sciences*, 114(28):E5741–E5749, 2017.

[58] Eugene A. Katrukha, Marina Mikhaylova, Hugo X. van Brakel, Paul M. van Bergen en Henegouwen, Anna Akhmanova, Casper C. Hoogenraad, and Lukas C. Kapitein. Probing cytoskeletal modulation of passive and active intracellular dynamics using nanobody-functionalized quantum dots. *Nature Communications*, 8(14772), 2017.

[59] Amy Reilein, Soichiro Yamada, and W. James Nelson. Self-organization of an acentrosomal microtubule network at the basal cortex of polarized epithelial cells . *Journal of Cell Biology*, 171(5):845–855, 11 2005.

[60] Ai hong Song, Dong Wang, Gang Chen, Yuju Li, Jianhong Luo, Shumin Duan, and Mu ming Poo. A selective filter for cytoplasmic transport at the axon initial segment. *Cell*, 136(6):1148 – 1160, 2009.

[61] Wen Lu, Margot Lakonishok, and Vladimir I. Gelfand. Kinesin-1powered microtubule sliding initiates axonal regeneration in drosophila cultured neurons. *Molecular Biology of the Cell*, 26(7):1296–1307, 2015.

[62] Jeffrey J. Nirschl, Amy E. Ghiretti, and Erika L. F. Holzbaur. The impact of cytoskeletal organization on the local regulation of neuronal transport. *Nature Reviews Neuroscience*, 18:585 – 597, 2017.

[63] Charles L. Asbury, Adrian N. Fehr, and Steven M. Block. Kinesin moves by an asymmetric hand-over-hand mechanism. *Science*, 302(5653):2130 – 2134, 2003.

[64] Ahmet Yildiz, Michio Tomishige, Ronald D. Vale, and Paul R. Selvin. Kinesin walks hand-over-hand. *Science*, 303(5658):676 –678, 2004.

[65] Anatoly B. Kolomeisky, Evgeny B. Stukalin, and Alex A. Popov. Understanding mechanochemical coupling in kinesins using first-passage-time processes. *Phys. Rev. E*, 71:031902, 2005.

[66] Comert Kural, Hwajin Kim, Sheyum Syed, Gohta Goshima, Vladimir I. Gelfand, and Paul R. Selvin. Kinesin and dynein move a peroxisome in vivo: A tug-of-war or coordinated movement? *Science*, 308(5727):1469–1472, 2005.

[67] Yunxin Zhang and Michael E. Fisher. Dynamics of the tug-of-war model for cellular transport. *Phys. Rev. E*, 82:011923, 2010.

[68] Štefan Bálint, Ione Verdeny Vilanova, Ángel Sandoval Álvarez, and Melike Lakadamyali. Correlative live-cell and superresolution microscopy reveals cargo transport dynamics at microtubule intersections. *Proceedings of the National Academy of Sciences*, 110(9):3375–3380, 2013.

[69] Victor Racine, Martin Sachse, Jean Salamero, Vincent Fraisier, Alain Trubuil, and Jean-Baptiste Sibarita. Visualization and quantification of vesicle traf-

ficking on a three-dimensional cytoskeleton network in living cells. *Journal of Microscopy*, 225(3):214–228, 2007.

[70] Avi Caspi, Rony Granek, and Michael Elbaum. Enhanced diffusion in active intracellular transport. *Phys. Rev. Lett.*, 85:5655–5658, 2000.

[71] Adam G. Hendricks, Bogdan I. Epureanu, and Edgar Meyhofer. Mechanistic mathematical model of kinesin under time and space fluctuating loads. *Nonlinear Dynamics*, 53:303–320, 2008.

[72] Woochul Nam and Bogdan I. Epureanu. Effects of obstacles on the dynamics of kinesins, including velocity and run length, predicted by a model of two dimensional motion. *Nonlinear Dynamics*, 11(1):e0147676, 2016.

[73] Stefan Klumpp and Reinhard Lipowsky. Cooperative cargo transport by several molecular motors. *Proceedings of the National Academy of Sciences*, 102(48):17284–17289, 2005.

[74] D. Kenneth Jamison, Jonathan W. Driver, Arthur R. Rogers, Pamela E. Constantinou, and Michael R. Diehl. Two kinesins transport cargo primarily via the action of one motor: Implications for intracellular transport. *Biophysical Journal*, 99(9):2967 – 2977, 2010.

[75] Gker Arpa, Stephen R. Norris, S. Iman Mousavi, Virupakshi Soppina, Kristen J. Verhey, William O. Hancock, and Erkan Tzel. Motor dynamics underlying cargo transport by pairs of kinesin-1 and kinesin-3 motors. *Biophysical Journal*, 116(6):1115 – 1126, 2019.

[76] Robert P. Erickson, Zhiyuan Jia, Steven P. Gross, and Clare C. Yu. How molecular motors are arranged on a cargo is important for vesicular transport. *PLoS computational biology*, 7(5):e1002032, 2011.

[77] GI Bell. Models for the specific adhesion of cells to cells. *Science*, 20(4342):618 – 627, 1978.

[78] Koen Visscher, Mark J. Schnitzer, and Steven M. Block. Single kinesin molecules studied with a molecular force clamp. *Nature*, 400:184 – 189, 1999.

[79] Janina Beeg, Stefan Klumpp, Rumiana Dimova, Rubn Serral Graci, Eberhard Unger, and Reinhard Lipowsky. Transport of beads by several kinesin motors. *Biophysical Journal*, 94(2):532 – 541, 2008.

[80] R. Kimmel and J. A. Sethian. Computing geodesic paths on manifolds. *Proceedings of the National Academy of Sciences*, 95(15):8431–8435, 1998.

[81] Ron Kimmel and James A. Sethian. Optimal algorithm for shape from shading and path planning. *Journal of Mathematical Imaging and Vision*, (14):237–244, 2001.

[82] J A Sethian. A fast marching level set method for monotonically advancing fronts. *Proceedings of the National Academy of Sciences*, 93(4):1591–1595, 1996.

[83] Sylvia Jeney, Ernst H. K. Stelzer, Helmut Grubmller, and Ernst-Ludwig Florin. Mechanical properties of single motor molecules studied by three-dimensional thermal force probing in optical tweezers. *ChemPhysChem*, 5(8):1150–1158, 2004.

[84] Jonas Ries, Charlotte Kaplan, Evgenia Platonova, Hadi Eghlidi, and Helge Ewers. A simple, versatile method for gfp-based super-resolution microscopy via nanobodies. *Nature Methods*, 9:582 – 584, 2012.

[85] Jonathon Howard and Anthony A Hyman. Microtubule polymerases and depolymerases. *Current Opinion in Cell Biology*, 19(1):31 – 35, 2007.

[86] N Hirokawa. Cross-linker system between neurofilaments, microtubules and membranous organelles in frog axons revealed by the quick-freeze, deep-etching method . *Journal of Cell Biology*, 94(1):129–142, 1982.

[87] Ali Ertürk, Farida Hellal, Joana Enes, and Frank Bradke. Disorganized microtubules underlie the formation of retraction bulbs and the failure of axonal regeneration. *Journal of Neuroscience*, 27(34):9169–9180, 2007.

[88] Justin E. Molloy and Claudia Veigel. Myosin motors walk the walk. *Science*, 300(5628):2045–2046, 2003.

[89] Ken'ya Furuta, Akane Furuta, Yoko Y. Toyoshima, Misako Amino, Kazuhiro Oiwa, and Hiroaki Kojima. Measuring collective transport by defined numbers of processive and nonprocessive kinesin motors. *Proceedings of the National Academy of Sciences*, 110(2):501–506, 2013.

[90] Jin-Wu Tsai, Wei-Nan Lian, Shahrnaz Kemal, Arnold R Kriegstein, and Richard B Vallee. Kinesin 3 and cytoplasmic dynein mediate interkinetic nuclear migration in neural stem cells. *Nature Neuroscience*, 13:1463–1471, 2010.

[91] Timothy Sanchez, David Welch, Daniela Nicastro, and Zvonimir Dogic. Cilia-like beating of active microtubule bundles. *Science*, 333(6041):456–459, 2011.

[92] Praveen D. Chowdary, Daphne L. Che, Luke Kaplan, Ou Chen, Kanyi Pu, Moungi Bawendi, and Bianxiao Cui. Nanoparticle-assisted optical tethering of endosomes reveals the cooperative function of dyneins in retrograde axonal transport. *Scientific Reports*, 5:18059, 2015.

[93] David Ando, Michelle K. Mattson, Jing Xu, and Ajay Gopinathan. Cooperative protofilament switching emerges from inter-motor interference in multiple-motor transport. *Scientific Reports*, 4:7255, 2014.

[94] Michael Vershinin, Brian C. Carter, David S. Razafsky, Stephen J. King, and Steven P. Gross. Multiple-motor based transport and its regulation by tau. *Proceedings of the National Academy of Sciences*, 104(1):87–92, 2007.

[95] Cécile Leduc, Felix Ruhnow, Jonathon Howard, and Stefan Diez. Detection of fractional steps in cargo movement by the collective operation of kinesin-1 motors. *Proceedings of the National Academy of Sciences*, 104(26):10847–10852, 2007.

[96] Ken'ya Furuta, Akane Furuta, Yoko Y. Toyoshima, Misako Amino, Kazuhiro Oiwa, and Hiroaki Kojima. Measuring collective transport by defined numbers of processive and nonprocessive kinesin motors. *Proceedings of the National Academy of Sciences*, 110(2):501–506, 2013.

[97] Shreyas Bhaban, Donatello Materassi, Mingang Li, Thomas Hays, and Murti Salapaka. Interrogating emergent transport properties for molecular motor ensembles: A semi-analytical approach. *PLOS Computational Biology*, 12(11):1–30, 11 2016.

[98] Harry W. Schroeder, Chris Mitchell, Henry Shuman, Erika L.F. Holzbaur, and Yale E. Goldman. Motor number controls cargo switching at actin-microtubule intersections in vitro. *Current Biology*, 20(8):687 – 696, 2010.

[99] Yuan Gao, Stephen M. Anthony, Yanqi Yu, Yi Yi, and Yan Yu. Cargos rotate at microtubule intersections during intracellular trafficking. *Biophysical Journal*, 114(12):2900 – 2909, 2018.

[100] Ludek Stepanek and Gaia Pigino. Microtubule doublets are double-track railways for intraflagellar transport trains. *Science*, 352(6286):721–724, 2016.

[101] Izaak Neri, Norbert Kern, and Andrea Parmeggiani. Modeling cytoskeletal

traffic: An interplay between passive diffusion and active transport. *Phys. Rev. Lett.*, 110:098102, 2013.

[102] George T. Shubeita, Susan L. Tran, Jing Xu, Michael Vershinin, Silvia Cermelli, Sean L. Cotton, Michael A. Welte, and Steven P. Gross. Consequences of motor copy number on the intracellular transport of kinesin-1-driven lipid droplets. *Cell*, 135(6):1098 – 1107, 2008.

[103] Cécile Leduc, Kathrin Padberg-Gehle, Vladimír Varga, Dirk Helbing, Stefan Diez, and Jonathon Howard. Molecular crowding creates traffic jams of kinesin motors on microtubules. *Proceedings of the National Academy of Sciences*, 109(16):6100–6105, 2012.

[104] Louis Reese, Anna Melbinger, and Erwin Frey. Crowding of molecular motors determines microtubule depolymerization. *Biophysical Journal*, 101(9):2190 – 2200, 2011.

[105] Daniël M. Miedema, Vandana S. Kushwaha, Dmitry V. Denisov, Seyda Acar, Bernard Nienhuis, Erwin J. G. Peterman, and Peter Schall. Correlation imaging reveals specific crowding dynamics of kinesin motor proteins. *Phys. Rev. X*, 7:041037, 2017.

[106] Reinhard Lipowsky, Stefan Klumpp, and Theo M. Nieuwenhuizen. Random walks of cytoskeletal motors in open and closed compartments. *Phys. Rev. Lett.*, 87:108101, 2001.

[107] Jing Xu, Stephen J. King, Maryse Lapierre-Landry, and Brian Nemec. Interplay between velocity and travel distance of kinesin-based transport in the presence of tau. *Biophysical Journal*, 105(10):L23 – L25, 2013.

[108] Matthias Rank and Erwin Frey. Crowding and pausing strongly affect dynamics

of kinesin-1 motors along microtubules. *Biophysical Journal*, 115(6):1068 – 1081, 2018.

[109] Steven M. Block, Charles L. Asbury, Joshua W. Shaevitz, and Matthew J. Lang. Probing the kinesin reaction cycle with a 2d optical force clamp. *Proceedings of the National Academy of Sciences*, 100(5):2351–2356, 2003.

[110] Karthik Uppulury, Artem K. Efremov, Jonathan W. Driver, D. Keeneth Jamison, Michael R. Diehl, and Anatoly B. Kolomeisky. How the interplay between mechanical and nonmechanical interactions affects multiple kinesin dynamics. *J. Phys. Chem. B*, 116(30):8846–8855, 2012.

[111] Hamid Khataee and Jonathon Howard. Force generated by two kinesin motors depends on the load direction and intermolecular coupling. *Phys. Rev. Lett.*, 122:188101, 2019.

[112] R. Blackwell, D. Jung, M. Bukenberger, and A. S. Smith. The impact of rate formulations on stochastic molecular motor dynamics. *Scientific Reports*, 9(18373), 2019.

[113] Keiko Hirose Kuniyoshi Kaseda, Hideo Higuchi. Alternate fast and slow stepping of a heterodimeric kinesin molecule. *Nature Cell Biology*, 5:1079–1082, 2003.

[114] Seohyun Lee and Hideo Higuchi. 3d rotational motion of an endocytic vesicle on a complex microtubule network in a living cell. *Biomed. Opt. Express*, 10(12):6611–6624, 2019.

[115] Seohyun Lee, Hyuno Kim, and Hideo Higuchi. Numerical method for vesicle movement analysis in a complex cytoskeleton network. *Opt. Express*, 26(13):16236–16249, 2018.

[116] Susan P. Gilbert, Michele L. Moyer, and Kenneth A. Johnson. Alternating site mechanism of the kinesin atpase. *Biochemistry*, 37(3):792–799, 1998.

[117] Mehmet Can Uar and Reinhard Lipowsky. Collective force generation by molecular motors is determined by strain-induced unbinding. *Nano Letters*, 20(1):669–676, 2020.

[118] Qian Wang and Anatoly B. Kolomeisky. Theoretical analysis of run length distributions for coupled motor proteins. *The Journal of Physical Chemistry B*, 123(27):5805–5813, 2019.

[119] Ivo A. Telley, Peter Bieling, and Thomas Surrey. Obstacles on the microtubule reduce the processivity of kinesin-1 in a minimal in vitro system and in cell extract. *Biophysical Journal*, 96(8):3341 – 3353, 2009.

[120] S. M. Ali Tabei, Stanislav Burov, Hee Y. Kim, Andrey Kuznetsov, Toan Huynh, Justin Jureller, Louis H. Philipson, Aaron R. Dinner, and Norbert F. Scherer. Intracellular transport of insulin granules is a subordinated random walk. *Proceedings of the National Academy of Sciences*, 110(13):4911–4916, 2013.

[121] Marcus Otten, Amitabha Nandi, Delphine Arcizet, Mari Gorelashvili, Benjamin Lindner, and Doris Heinrich. Local motion analysis reveals impact of the dynamic cytoskeleton on intracellular subdiffusion. *Biophysical Journal*, 102(4):758 – 767, 2012.

[122] V. Zaburdaev, S. Denisov, and J. Klafter. Lévy walks. *Rev. Mod. Phys.*, 87:483–530, 2015.

[123] Ashim Rai, Divya Pathak, Shreyasi Thakur, Shampa Singh, Alok Kumar Dubey, and Roop Mallik. Dynein clusters into lipid microdomains on phagosomes to drive rapid transport toward lysosomes. *Cell*, 164(4):722 – 734, 2016.

[124] Lewis Fry Richardson. Atmospheric diffusion shown on a distance-neighbour graph. *Proc. R. Soc. Lond.*, 110, 1926.

[125] Benjamin M. Regner, Dejan Vuini, Cristina Domnisoru, Thomas M. Bartol, Martin W. Hetzer, Daniel M. Tartakovsky, and Terrence J. Sejnowski. Anomalous diffusion of single particles in cytoplasm. *Biophysical Journal*, 104(8):1652 – 1660, 2013.

[126] I. Rhee, M. Shin, S. Hong, K. Lee, S. J. Kim, and S. Chong. On the levy-walk nature of human mobility. *IEEE/ACM Transactions on Networking*, 19(3):630–643, 2011.

[127] Gil Ariel, Amit Rabani, Sivan Benisty, Jonathan D. Partridge, Rasika M. Harshey, and Avraham Be'er. Swarming bacteria migrate by lèvy walk. *Nature Communications*, 6(8396), 2015.

[128] Baron Fourier and Jean Baptiste Joseph. Thorie analytique de la chaleur. *F. Didot*, 1822.

[129] George H Weiss. Some applications of persistent random walks and the telegrapher's equation. *Physica A: Statistical Mechanics and its Applications*, 311(3):381 – 410, 2002.

[130] K. Razi Naqvi, S. Waldenstro/m, and K. J. Mork. On the rate of absorption of brownian particles by a black sphere: The connection between the fokker-planck equation and the diffusion equation. *The Journal of Chemical Physics*, 78(5):2710–2712, 1983.

[131] Cascaval RC, Eckstein EC, Frota CL, and Goldstein JA. Fractional telegraph equations. *Journal of Mathematical Analysis and Applications*, 1(276):145–159, 2002.

[132] E. Barkai, R. Metzler, and J. Klafter. From continuous time random walks to the fractional fokker-planck equation. *Phys. Rev. E*, 61:132–138, 2000.

[133] Vasily Zaburdaev, Michael Schmiedeberg, and Holger Stark. Random walks with random velocities. *Phys. Rev. E*, 78:011119, Jul 2008.

[134] V. Zaburdaev, S. Denisov, and P. Hänggi. Perturbation spreading in many-particle systems: A random walk approach. *Phys. Rev. Lett.*, 106:180601, 2011.

[135] Jaume Masoliver, Katja Lindenberg, and George H. Weiss. A continuous-time generalization of the persistent random walk. *Physica A: Statistical Mechanics and its Applications*, 157(2):891 – 898, 1989.

[136] Jaume Masoliver, Josep M. Porr, and George H. Weiss. Some two and three-dimensional persistent random walks. *Physica A: Statistical Mechanics and its Applications*, 193(3):469 – 482, 1993.

[137] Oleksandr Chepizhko and Fernando Peruani. Diffusion, subdiffusion, and trapping of active particles in heterogeneous media. *Phys. Rev. Lett.*, 111:160604, Oct 2013.

[138] R. Friedrich, F. Jenko, A. Baule, and S. Eule. Anomalous diffusion of inertial, weakly damped particles. *Phys. Rev. Lett.*, 96:230601, Jun 2006.

[139] Joseph Snider, Francis Lin, Neda Zahedi, Vladimir Rodionov, Clare C. Yu, and Steven P. Gross. Intracellular actin-based transport: How far you go depends on how often you switch. *Proceedings of the National Academy of Sciences*, 101(36):13204–13209, 2004.

[140] Rajan P. Kulkarni, David D. Wu, Mark E. Davis, and Scott E. Fraser. Quantitating intracellular transport of polyplexes by spatio-temporal image correlation

spectroscopy. *Proceedings of the National Academy of Sciences*, 102(21):7523–7528, 2005.

[141] George T. Shubeita, Susan L. Tran, Jing Xu, Michael Vershinin, Silvia Cermelli, Sean L. Cotton, Michael A. Welte, and Steven P. Gross. Consequences of motor copy number on the intracellular transport of kinesin-1-driven lipid droplets. *Cell*, 135(6):1098 – 1107, 2008.

[142] D.A. Smith and R.M. Simmons. Models of motor-assisted transport of intracellular particles. *Biophysical Journal*, 80(1):45 – 68, 2001.

[143] Bo Wang, James Kuo, Sung Chul Bae, and Steve Granick. When brownian diffusion is not gaussian. *Nature Materials*, 11:481–485, 2012.

[144] Bo Wang, Stephen M. Anthony, Sung Chul Bae, and Steve Granick. Anomalous yet brownian. *Proceedings of the National Academy of Sciences*, 106(36):15160–15164, 2009.

[145] Ralf Metzler. Gaussianity fair: The riddle of anomalous yet non-gaussian diffusion. *Biophysical Journal*, 112(3):413–415, 2017.

[146] Mykyta V. Chubynsky and Gary W. Slater. Diffusing diffusivity: A model for anomalous, yet brownian, diffusion. *Phys. Rev. Lett.*, 113:098302, 2014.

[147] Rafael Morgado, Fernando A. Oliveira, G. George Batrouni, and Alex Hansen. Relation between anomalous and normal diffusion in systems with memory. *Phys. Rev. Lett.*, 89:100601, Aug 2002.

[148] Janet Rossant and Patrick P.L. Tam. New insights into early human development: Lessons for stem cell derivation and differentiation. *Cell Stem Cell*, 20(1):18 – 28, 2017.

[149] Aryeh Warmflash, Benoit Sorre, Fred Etoc, Eric D Siggia, and Ali H Brivanlou. A method to recapitulate early embryonic spatial patterning in human embryonic stem cells. *Nature Methods*, 11:847–854, 2014.

[150] Mariaceleste Aragona, Tito Panciera, Andrea Manfrin, Stefano Giulitti, Federica Michielin, Nicola Elvassore, Sirio Dupont, and Stefano Piccolo. A mechanical checkpoint controls multicellular growth through yap/taz regulation by actin-processing factors. *Cell*, 154(5):1047 – 1059, 2013.

[151] Wouter Saelens, Robrecht Cannoodt, Helena Todorov, and Yvan Saeys. A comparison of single-cell trajectory inference methods. *Nature biotechnology*, 37:547 – 554, 2019.

[152] Keren Bahar Halpern, Rom Shenhav, Orit Matcovitch-Natan, Beta Tth, Doron Lemze, Matan Golan, Efi E. Massasa, Shaked Baydatch, Shanie Landen, Andreas E. Moor, Alexander Brandis, Amir Giladi, Avigail Stokar-Avihail, Eyal David, Ido Amit, and Shalev Itzkovitz. Single-cell spatial reconstruction reveals global division of labour in the mammalian liver. *Nature*, 542:352–356, 2017.

[153] Samuel G. Rodriques, Robert R. Stickels, Aleksandrina Goeva, Carly A. Martin, Evan Murray, Charles R. Vanderburg, Joshua Welch, Linlin M. Chen, Fei Chen, and Evan Z. Macosko. Slide-seq: A scalable technology for measuring genome-wide expression at high spatial resolution. *Science*, 363(6434):1463–1467, 2019.

[154] R. R. Coifman, S. Lafon, A. B. Lee, M. Maggioni, B. Nadler, F. Warner, and S. W. Zucker. Geometric diffusions as a tool for harmonic analysis and structure definition of data: Diffusion maps. *Proceedings of the National Academy of Sciences*, 102(21):7426–7431, 2005.

[155] Manu Setty, Michelle D Tadmor, Shlomit Reich-Zeliger, Omer Angel, Tomer Meir Salame, Pooja Kathail, Kristy Choi, Sean Bendall, Nir Friedman,

and Dana Pe'er. Wishbone identifies bifurcating developmental trajectories from single-cell data. *Nature biotechnology*, 34:637–645, 2016.

[156] Bernard W. Silverman. Smoothed functional principal components analysis by choice of norm. *The Annals of Statistics*, 24(1):1–24, 1996.

[157] https://pydiffmap.readthedocs.io/en/master/reference/diffusion_map.html.